

# Modelling and Simulation for Concrete Durability: Mechanism and Prediction

Lead Guest Editor: Qing-feng Liu

Guest Editors: Branko Šavija, Jin Xia, Xiaoshan Lin, and Dongshuai Hou





---

# **Modelling and Simulation for Concrete Durability: Mechanism and Prediction**



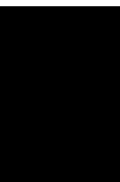
Modelling and Simulation in Engineering

---

**Modelling and Simulation for Concrete  
Durability: Mechanism and Prediction**

Lead Guest Editor: Qing-feng Liu

Guest Editors: Branko Šavija, Jin Xia, Xiaoshan Lin,  
and Dongshuai Hou



---

Copyright © 2021 Hindawi Limited. All rights reserved.

This is a special issue published in “Modelling and Simulation in Engineering.” All articles are open access articles distributed under the Creative Commons Attribution License, which permits unrestricted use, distribution, and reproduction in any medium, provided the original work is properly cited.

## **Editorial Board**

Fahad Al Basir, India  
Jean-Michel Bergheau, France  
Agostino Bruzzone, Italy  
Michele Cali, Italy  
Elio Chiodo, Italy  
Ming-Cong Deng, Japan  
Tadashi Dohi, Japan  
Dimitris Drikakis, United Kingdom  
Dariusz J. Gawin, Poland  
Parviz Ghadimi, Iran  
Jing-song Hong, China  
Ameur Houari, Algeria  
Paolo Iodice, Italy  
MuDer Jeng, Taiwan  
Stavros Kotsopoulos, Greece  
Rajesh Kumar, India  
Nikos D. Lagaros, Greece  
Fazle Mabood, Canada  
Dimitrios E. Manolakos, Greece  
Angelos Markopoulos, Greece  
Carlos A. Mota Soares, Portugal  
Javier Murillo, Spain  
Ricardo Perera, Spain  
ADRIAN PLESCA, Romania  
Zhiping Qiu, China  
Luis Carlos Rabelo, USA  
Franco Ramírez, Spain  
Mohammed Seaid, United Kingdom  
Gaetano Sequenzia, Italy  
Aiguo Song, China  
Chen Lin Soo, Malaysia  
Mohamed B. Trabia, USA  
Nicolò Vaiana, Italy  
Joseph Virgone, France  
Feng Xiao, China  
Farouk Yalaoui, France



# Contents

---

## **Modelling and Simulation for Concrete Durability: Mechanism and Prediction**

Qing-feng Liu , Branko Šavija , Jin Xia , Xiaoshan Lin , and Dongshuai Hou   
Editorial (2 pages), Article ID 9782710, Volume 2021 (2021)


## **Improved Crack Detection and Recognition Based on Convolutional Neural Network**

Keqin Chen , Amit Yadav, Asif Khan , Yixin Meng, and Kun Zhu  
Research Article (8 pages), Article ID 8796743, Volume 2019 (2019)

## **Hydration of Early Age Cement Paste with Nano-CaCO<sub>3</sub> and SAP by LF-NMR Spectroscopy: Mechanism and Prediction**

Haitao Zhao , Gaoyang Sun, Lu Yu, Kaidi Jiang, Xiaodong Chen, Ruiming Jia, Yi Wan, and Shihai Li  
Research Article (10 pages), Article ID 8384051, Volume 2019 (2019)

## **Modeling of the Axial Load Capacity of RC Columns Strengthened with Steel Jacketing under Preloading Based on FE Simulation**

Ahmed M. Sayed  and Hesham M. Diab  
Research Article (8 pages), Article ID 8653247, Volume 2019 (2019)

## **Numerical Study on Diffusion of Chloride and Induced Rebar Corrosion by Two-Dimensional Multiscale Approach**

Xi Tu , Jin Di, Cunjun Pang, and Xiaoqing Xu   
Research Article (20 pages), Article ID 1932813, Volume 2018 (2018)

## Editorial

# Modelling and Simulation for Concrete Durability: Mechanism and Prediction

**Qing-feng Liu** <sup>1</sup>, **Branko Šavija** <sup>2</sup>, **Jin Xia** <sup>3</sup>, **Xiaoshan Lin** <sup>4</sup>, and **Dongshuai Hou** <sup>5</sup>

<sup>1</sup>State Key Laboratory of Ocean Engineering, School of Naval Architecture, Ocean and Civil Engineering, Shanghai Jiao Tong University, Shanghai 200240, China

<sup>2</sup>Microlab, Faculty of Civil Engineering and Geosciences, Delft University of Technology, Delft 2628CN, Netherlands

<sup>3</sup>Institute of Structural Engineering, Zhejiang University, Hangzhou, China

<sup>4</sup>School of Engineering, RMIT University, Australia

<sup>5</sup>Department of Civil Engineering, Qingdao University of Technology, China

Correspondence should be addressed to Qing-feng Liu; liuqf@sjtu.edu.cn

Received 28 July 2021; Accepted 28 July 2021; Published 16 August 2021

Copyright © 2021 Qing-feng Liu et al. This is an open access article distributed under the Creative Commons Attribution License, which permits unrestricted use, distribution, and reproduction in any medium, provided the original work is properly cited.

Concrete is the most widely used man-made material in the modern construction industry. However, the service life of concrete has been seriously shortened due to durability problems, particularly when serving in nonideal environments and suffering internal/external attacks. In this regard, the development of a better understanding of the deterioration mechanisms as well as reliable prediction methods for durability properties and/or long-term performance of concrete is necessary. Modern computational modelling theories and methods are favorable for bringing innovative solutions to the above issues. The objective of this special issue is to present novel modelling studies on concrete durability by using analytical/numerical approaches alone or in conjunction with experimental techniques.

During the submission period, we received more than 20 submissions from more than 10 different countries. All these submissions were well written and had their own innovations, but only 4 of them were selected as they were closer to the subjects of this special issue. The articles published in this special issue covered various scales from the C-S-H to reinforced concrete components and finally concrete-based buildings, and the following topics were involved: (a) simulation of deterioration processes; (b) permeability and diffusivity modelling; (c) cracking and fracture detection; (d) simulation of rebar corrosion process; (e) simulation of hydration processes; and (f) prediction

model of long-term performance. The contributions offered by each paper are detailed in the following.

The paper entitled “Numerical Study on Diffusion of Chloride and Induced Rebar Corrosion by Two-Dimensional Multiscale Approach” by X. Tu et al. described a two-dimensional multiscale model including core parts and compensation apart and three-phase mesoscales including binder, aggregate, and ITZ to simulate chloride diffusion within concrete. The diffusivity and width of ITZ, volume fraction, and grade of aggregate were studied. Besides, the authors also discussed rebar corrosion in terms of intrusion by external chloride. The distribution of chloride content was considered with the change of ITZ and compensation. This presented work showed the benefits of a multiscale model and provided the basis for future large-scale structure numerical studies.

The paper entitled “Modeling of the Axial Load Capacity of RC Columns Strengthened with Steel Jacketing under Preloading Based on FE Simulation” by A. M. Sayed and H. M. Diab devised a macroscale three-dimensional finite element (FE) model to analyze the conduct and capacity of RC (reinforced concrete) square columns reinforced with steel jacketing under static preload. In comparison with previously experimental results, the proposed FE model of the component showed good accuracy. Thus, the model revealed the potential for calculating RC columns’ load capacity and for predicting accurate failure modes.

The paper entitled “Hydration of Early Age Cement Paste with Nano-CaCO<sub>3</sub> and SAP by LF-NMR Spectroscopy: Mechanism and Prediction” by H. Zhao et al. brought a deep-seated mechanism such as the interaction among various mineral hydrations into consideration and tested the evolution of the physically bound water using the low-field nuclear magnetic resonance (LF-NMR) technology. The microscope hydration process was divided into 4 periods and analyzed, respectively. The effects of water to cement ratio ( $w/c$ ), NC (nano-CaCO<sub>3</sub>), and SAP (superabsorbent polymer) on each hydration process period of cement-based materials were discussed in detail. Meanwhile, a modified hydration model considering the content of NC and SAP is also proposed.

The paper entitled “Improved Crack Detection and Recognition Based on Convolutional Neural Network” by K. Chen et al. improved crack detection based on convolutional neural networks, which can automatically detect whether an image contains cracks and mark the location of the cracks. In this paper, the authors firstly tested and improved the convolution neural networks with an accuracy of 99.71%. Secondly, they introduced this automatic system for historic buildings. From their experiments, the system had a certain value for periodic inspection and maintenance of long-term buildings.

With this special issue, we hope researchers (and interested readers as well) who have been engaged in this or related areas receive advanced information, gain ideas, and then further promote the development of modelling of concrete durability. We, the guest editors, hope it will stimulate relevant research interests on both performance prediction at the structural level and mechanism investigations at the material level in the coming future.

### **Conflicts of Interest**

We declare that we have no financial or personal relationships with other people or organizations that can inappropriately influence the work included in this special issue.

*Qing-feng Liu*  
*Branko Šavija*  
*Jin Xia*  
*Xiaoshan Lin*  
*Dongshuai Hou*



## Research Article

# Improved Crack Detection and Recognition Based on Convolutional Neural Network

Keqin Chen <sup>1,2</sup>, Amit Yadav,<sup>2</sup> Asif Khan <sup>3,4</sup>, Yixin Meng,<sup>2</sup> and Kun Zhu<sup>2</sup>

<sup>1</sup>School of Business Administration, Southwestern University of Finance and Economics, Chengdu 611130, China

<sup>2</sup>Department of Information and Software Engineering, Chengdu Neusoft University, Dujianyan, Chengdu, Sichuan 611844, China

<sup>3</sup>Crescent Institute of Science and Technology, Vandalur, Chennai 600048, India

<sup>4</sup>University of Electronic Science and Technology of China, Chengdu, China

Correspondence should be addressed to Keqin Chen; 3118268411@qq.com

Received 29 June 2019; Accepted 22 August 2019; Published 14 October 2019

Guest Editor: Qing-Feng Liu

Copyright © 2019 Keqin Chen et al. This is an open access article distributed under the Creative Commons Attribution License, which permits unrestricted use, distribution, and reproduction in any medium, provided the original work is properly cited.

Concrete cracks are very serious and potentially dangerous. There are three obvious limitations existing in the present machine learning methods: low recognition rate, low accuracy, and long time. Improved crack detection based on convolutional neural networks can automatically detect whether an image contains cracks and mark the location of the cracks, which can greatly improve the monitoring efficiency. Experimental results show that the Adam optimization algorithm and batch normalization (BN) algorithm can make the model converge faster and achieve the maximum accuracy of 99.71%.

## 1. Introduction

Traditional concrete which is used for various construction purposes such as buildings, bridges, and dams often age due to years of use which causes problems that affect the construction facilities. In order to avoid the problems caused by the aging of the facilities, it is necessary to continuously monitor and maintain the facilities. The traditional manual inspection method obviously cannot meet the huge road pavement inspection requirements. At present, many computer vision technologies realize the detection of cracks. Yiyang proposed a crack detection algorithm based on digital image processing technology [1]. Through pre-processing, image segmentation, and feature extraction, Yiyang obtained information about the crack image. The threshold segmentation method is used after smoothing the accepted input image. To determine their image, Yiyang calculated the area and circumference of the circle. Then, by comparison, Yiyang evaluated the presence of cracks in the image. Oliveira and Correia designed an automatic crack detection system [2]. Crack detection here is based on a sample. In the sample paradigm, a subset of the available

image databases is automatically selected and used for unsupervised training of system images. They have characterized operations based on the classification of non-overlapping image blocks. The width of the crack is then estimated based on the detection of the crack block. An improved dynamic programming-based algorithm is proposed to detect cracks [3]. The algorithm performs fast but has low accuracy. The Gabor filter is used to detect cracks [4], which has a good effect on the detection of simple pavement cracks and is severely broken for the detection of complex cracks. Zhang et al. [5] adopted four-layer convolutional neural network (CNN) to realize crack detection, with an accuracy of 87%, which needs to be improved. Zhang et al. [6] proposed a new region growth algorithm to detect road cracks, which is not suitable for detecting small and scattered cracks in the road. The extended finite element formula (XFEM) combined with the genetic algorithm (GA) has been proven to be effective in detecting structural defects [7–9], but this method also has many limitations. In this article, a novel method [10] is used to improve the convolutional neural network [11, 12], so that the convolutional neural network can automatically detect the crack in the image and

mark the corresponding position. The contribution of this article is twofold. The first system based on convolutional neural network is a good technique for detecting cracks in concrete structures, with an average accuracy of 99.71%. Secondly, the automatic detection system for historical buildings is introduced. In order to ensure the integrity of historical building structure, especially the degradation of masonry structure caused by aging and human activities, it has certain reference value for periodic inspection and maintenance of cultural relics. In practical, drones can easily detect ancient buildings, bridges, dams, and temples that are not easily monitored by humans. A convolutional neural network is used to collect images, detect the presence of cracks, and mark the corresponding cracks.

## 2. Improvement Based on Convolutional Neural Network

*2.1. Classical Convolutional Neural Network.* Relative to traditional neural network back propagation (BP neural network) [12, 13], the use of weight sharing in convolutional neural networks can greatly reduce network parameters and accelerate the training speed of the network. The performance is stronger than that of BP neural networks. Convolutional neural networks have powerful feature extraction capabilities. Using the advantages of convolutional neural networks, convolutional neural networks are widely used in various fields, including image classification, object detection, autopilot, and image style migration.

A classic convolutional neural network usually includes an input layer, a convolutional layer, a pooled layer (under the layer), a fully connected layer, and an output layer, as shown in Figure 1.

### 2.1.1. Convolution Layer

$$H_i = f(H_{i-1} \otimes W_i + b_i), \quad (1)$$

where  $i$  indicates the number of layers in the network,  $H_{i-1}$  represents the upper layer,  $i-1$  indicates the layer output value, and  $w_i$  indicates the weight of the network at the  $i$  level. The weight is generally carried out by random initialization. The “ $\otimes$ ” symbol indicates a convolution operation, where  $f$  indicates that the result of the convolution is input to an activation function that is nonlinearized.

*2.1.2. Pooling Layer.* The pooling layer includes max pooling, mean pooling, and random pooling. Here, the maximum pooling used in this paper is mainly discussed. Maximum pooling, selects the maximum value in the area within a certain area.

*2.2. Improvement Based on Convolutional Nerve.* Because the crack to be identified is quite different from the background color of the picture, the task of identification is relatively simple. Therefore, the convolution kernel and pooling size used in the network are generally large, and the network structure is simple. The network is batch normalized (BN)

[14] after each layer of pooling. The mathematical expression of batch normalization is normalized, as shown in the formula (2)–(5). The input is normalized to a data distribution with an average of 0 and a variance of 1. Then, the normalization operation destroys the possible data distribution of the data itself and performs matrix shrinking and translation on the normalized result to recover the data distribution characteristics that the data itself may have. Batch normalization can avoid the model overfitting to some extent. At the same time, it can accelerate the convergence of the model and improve the stability of training.

$$\mu_{\mathcal{B}} \leftarrow \frac{1}{m} \sum_{i=1}^m x_i, \quad (2)$$

$$\sigma_{\mathcal{B}}^2 \leftarrow \frac{1}{m} \sum_{i=1}^m (x_i - \mu_{\mathcal{B}})^2, \quad (3)$$

$$\hat{x}_i \leftarrow \frac{x_i - \mu_{\mathcal{B}}}{\sqrt{\sigma_{\mathcal{B}}^2 + \epsilon}}, \quad (4)$$

$$y_i \leftarrow \gamma \hat{x}_i + \beta \equiv \text{BN}_{\gamma, \beta}(x_i). \quad (5)$$

*2.2.1. Adam Algorithm.* In terms of the choice of optimizer for model training, instead of the traditional SGD [15] optimization using the faster convergence Adam [16] algorithm, Adam was submitted by OpenAI’s Diederik Kingma and the University of Toronto’s Jimmy Ba to the 2015 ICLR paper (Adam), “A Method for Stochastic Optimization.” Adam can set a learning rate for each weight parameter, giving a smaller learning rate for those weights that are updated more frequently and giving a larger learning rate for those with fewer updates, while updating the parameters. The momentum technique is introduced to consider the past gradient in the parameter update, so that the updated value of the current time is composed of the gradient and the last updated gradient, which can effectively reduce the oscillation of the loss function, stabilize the training process, and speed up the training. The updated formula is as follows:

$$\theta_{t+1} = \theta_t - \frac{\eta}{\sqrt{\hat{v}_t} + \epsilon} \hat{m}_t, \quad (6)$$

where  $\theta$  represents the parameters in the network, the number of iterations of the  $t$ ,  $\eta$  represents the network learning rate, and  $\epsilon$  is a small floating-point number, which is used to avoid meaningless operations when the denominator  $\llbracket \sqrt{\hat{v}} \rrbracket_t$  is zero. Also,  $\hat{m}_t$  represents the gradient after increasing the momentum factor, and the function of  $\sqrt{\hat{v}_t}$  is to set a separate learning rate for each parameter.

*2.3. Network Structure.* The network structure used in this paper is shown in Figure 2. The input is a 227-pixel  $\times$  227-pixel RGB 3-channel picture. After 24 convolution kernels with a size of  $20 \times 20$  and a stride of 2,  $114 \times 114$  is obtained. The tensor output of  $\times 24$ , after  $7 \times 7$ , the pooling layer with a

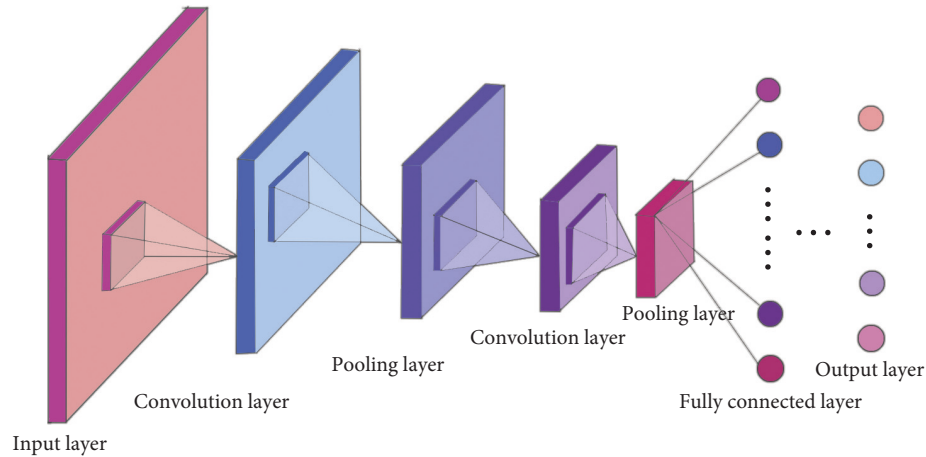


FIGURE 1: Typical convolutional neural network.

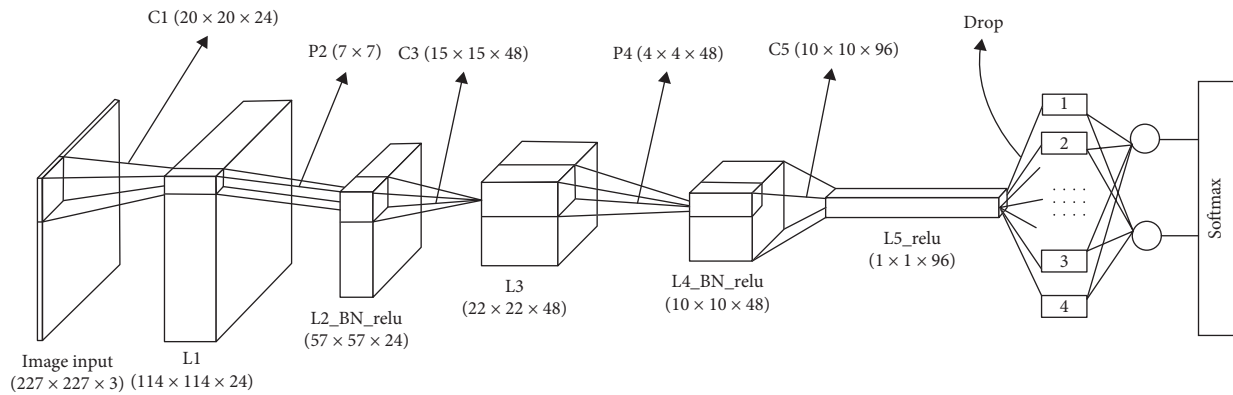


FIGURE 2: Network structure.

step size of 2 outputs  $57 \times 57 \times 24$  tensor, then it is subjected to nonlinearization by batch normalization (BN) and relu activation function processing. Then, after 48 convolutions of  $15 \times 15$  steps of 2, a tensor of  $22 \times 22 \times 48$  is obtained, and after  $4 \times 4$  steps of 2, a tensor of  $10 \times 10 \times 48$  is obtained, also after the tensor is obtained, it is processed by batch normalized processing (BN) and relu activation function for nonlinear processing, the activated  $10 \times 10 \times 48$  tensor is obtained, and then 96 convolutions of  $10 \times 10$  steps are obtained to obtain  $1 \times 1 \times 96$  tensor. Then, after passing through the fully connected layer of size 2, it is then passed through softmax to convert the output value into a probability output to obtain the result. Note that there are many parameters in the fully connected layer. In order to avoid overfitting, dropout [17] is used to ignore some nodes randomly and proportionally, so that the node does not work in this calculation, and to avoid the overfitting to some extent. The specific network parameter configuration is shown in Table 1.

### 3. Empirical Research

#### 3.1. Lab Environment

Translator: Python3.6

Operating environment: Spyder

Processor: Intel(R) Core(TM) i5-6200U CPU @ 2.60 GHz 2.59 GHz

Running memory: 4G

Operating system: Windows 10 Enterprise

Machine learning framework: TensorFlow 1.8

3.2. *Data Set.* A training data set of concrete gap images provided by Mendeley [18], including specific images with cracks. The test data comes from Middle East Technical University campus building. The data set is divided into two categories, cracked and crack-free images. Each type of image has 20,000 images, and each image has RGB pixels of 227-pixels  $\times$  227-pixels, for a total of 40,000 images. The crack data set image is shown in Figure 3 below. These 40,000 images are cut from 458 high-resolution ( $4032 \times 3024$ ) images, which are mentioned in Figure 3. High-resolution images differ in terms of the lighting and the like.

3.3. *Experimental Result.* Before the experiment begins, the data are divided into a part of the verification data set. The size of the model output data batch is 32. Before image input, sample normalization of the image was conducted and label data were encoded by one-hot encoding. Use the network structure of Figure 2 for training. The loss value is printed



TABLE 1: Network parameter.

Layer	Size	Operator	Filters	Kernel_size	Strides	Padding
Input	$227 \times 227 \times 3$	C1	24	$20 \times 20$	2	Same
L1	$114 \times 114 \times 24$	P2	—	$7 \times 7$	2	Same
L2	$57 \times 57 \times 24$	BN	—	—	—	—
		relu	—	—	—	—
		C3	48	$15 \times 15$	2	Valid
L3	$22 \times 22 \times 48$	P4	—	$4 \times 4$	2	Valid
L4	$10 \times 10 \times 48$	BN	—	—	—	—
		relu	—	—	—	—
		C4	96	$10 \times 10$	2	Valid
L5	$1 \times 1 \times 96$	relu	—	—	—	—
		Drop	—	—	—	—
L6	$1 \times 1 \times 2$	C5	2	$1 \times 1$	1	Valid

The learning rate is set to 0.0001, and the learning rate drops to 0.99 for each iteration of 100; the dropout is set to 0.5.

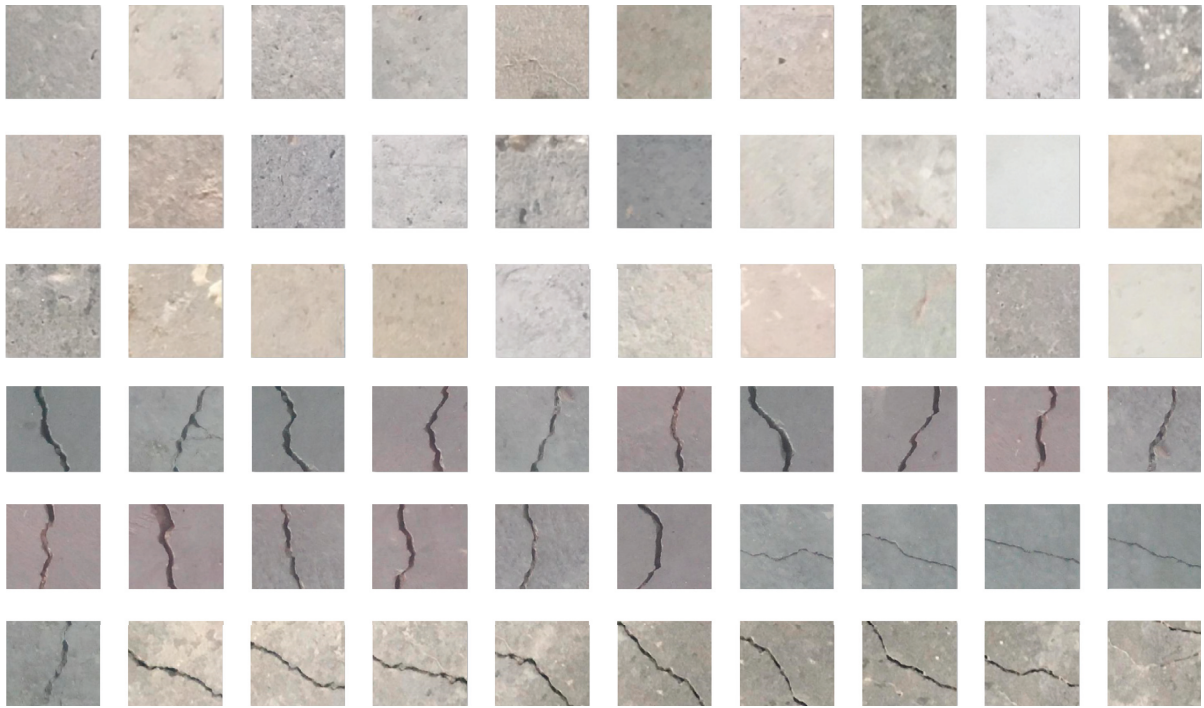


FIGURE 3: Crack image sample.

once in every 100 iterations, and the model is evaluated once every 1000 iterations using the verification data set, as shown in Figure 4. If the correct rate of this evaluation is greater than the last time, the model is retained, and if 100 consecutive times are less than the correct rate of the previous evaluation, then training is stopped, which experimentally proves that the use of Adam optimization algorithm and batch normalization (BN) can make the model converge faster.

After 110k iteration, the program automatically stops training, and the correct rate of the model is about 99.71%. As can be seen from Figure 5, after 11k iterations, the maximum correct rate is achieved. It takes about 50 minutes. As can be seen from the figure, due to the continuous reduction of the learning rate, the correct rate is gradually stabilized in the later stages of training.

Table 2 shows Zhang's ConvNet built through the Caffe framework and trained through the use of 5-fold cross-validation [5]. The results obtained from different methods i.e., SVM and Boost are compared. Using ConvNes and Adam, it can be seen that the accuracy result of each method is 0.8112, 0.736, 0.8696, and 0.9971, respectively. The most accurate result is that of the Adam method.

*3.4. Recognition Effect Display and Analysis.* The large size images used for verification come from Google Images, all containing cracks. Since the image resolution is much larger than the  $227 \times 227$  input size of the model, the image is first cut into small images of  $227 \times 227$  and placed into the model. After detection, the results are returned and the crack location is marked in the figure according to the returned results. The specific effect diagram is shown in Figure 6.

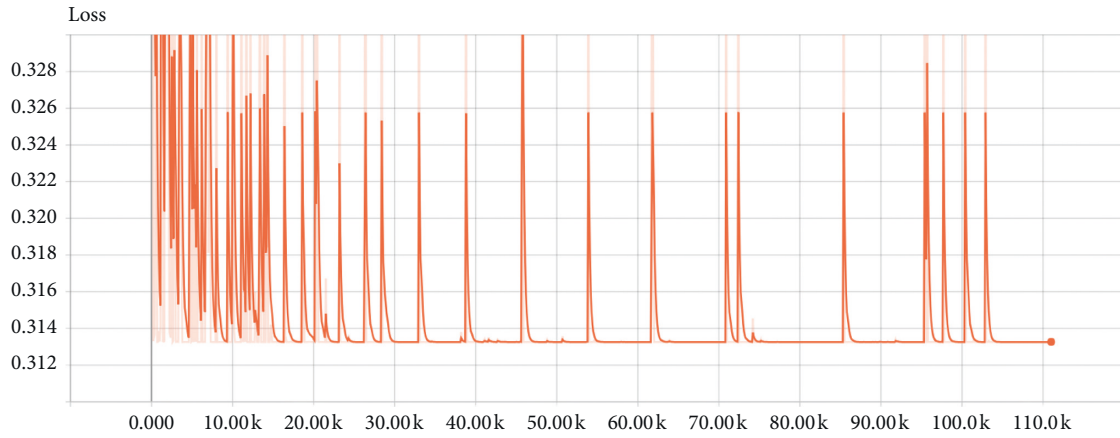


FIGURE 4: Printed loss value. Each iteration prints a loss of 100 times and evaluates the model once per 1000 iterations using the validation data set.

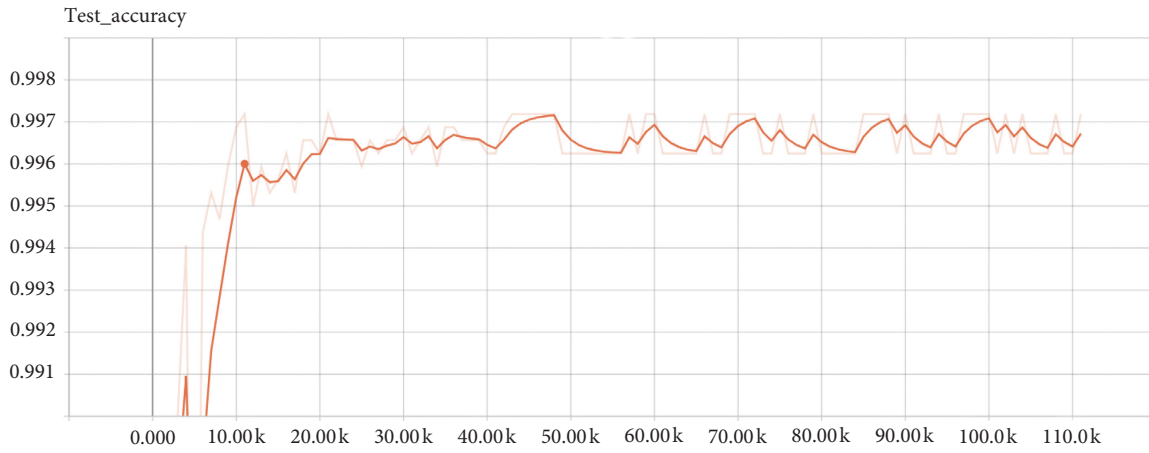
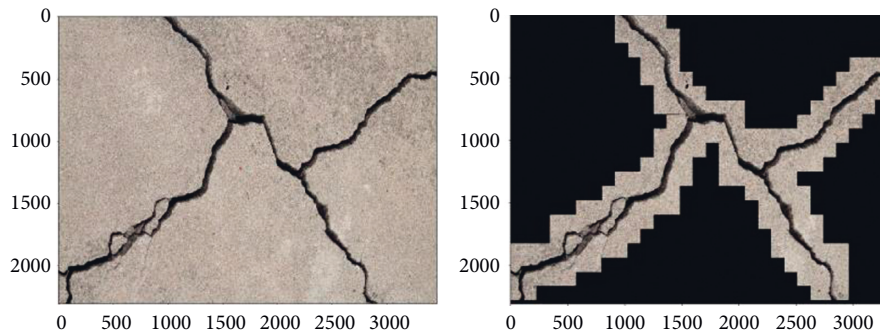


FIGURE 5: Correct rate change chart. The light line is the set of real data points, and the solid line is the set of points after the smoothing process.

TABLE 2: Performance comparison of different methods.

Method	SVM	Boosting	ConvNets	Adam
Precision	0.8112	0.736	0.8696	0.9971



(a)

FIGURE 6: Continued.

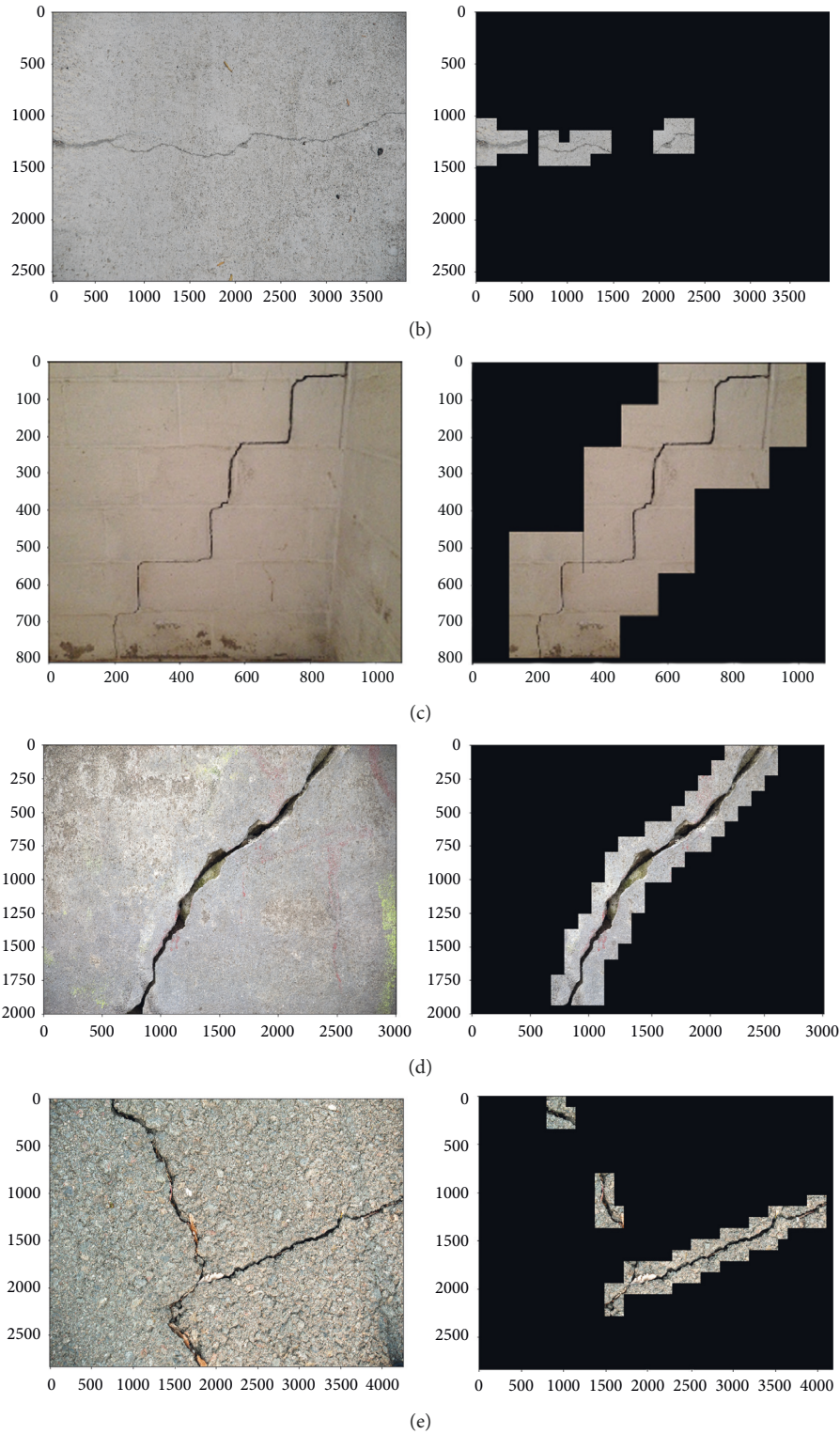


FIGURE 6: Continued.

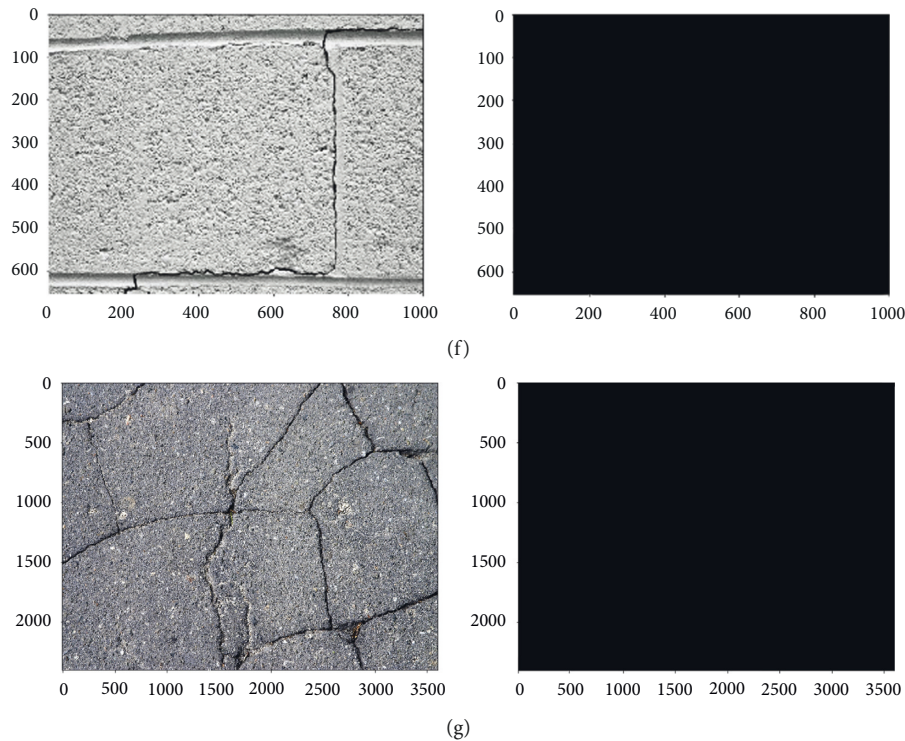


FIGURE 6: Crack recognition effect display.

By comparing the results of the picture, it can be seen that the model can better distinguish the picture with the contrast of the background color of the crack and the picture, as shown in Figures 6(a), 6(c), and 6(d). However, in Figures 6(b), 6(e), and 6(f), the identification effects are not properly visible for cracks which is unapparent. The reason behind this issue is that cracks are narrow and the colour of the cracks is similar to the background colour of the wall. The result is poor in Figure 6(g) as it does not identify a crack, which may be due to the model itself is based on the black interpretation of the image to determine whether there is a crack. The solution to this problem is to add black to the background in the training dataset or include relatively dark lines of cracks on similar pictures while doing analysis using the neural network.

#### 4. Conclusion

In this paper, the use of relatively simple and improved convolutional neural networks has successfully achieved the identification of cracks and has a very high accuracy rate. For the analysis of relatively simple crack identification, it is suggested that the use of large convolution and pooling methodology with fewer network layers can be helpful to get better results.

#### Data Availability

The authors confirm that the data supporting the findings of this study are available within the article.

#### Conflicts of Interest

The authors declare that there are no conflicts of interest regarding the publication of this paper.

#### References

- [1] Z. Yiyang, "The design of glass crack detection system based on image preprocessing technology," in *Proceedings of the 2014 IEEE 7th Joint International Information Technology and Artificial Intelligence Conference (ITAIC)*, pp. 39–42, IEEE, Chongqing, China, December 2014.
- [2] H. Oliveira and P. L. Correia, "Automatic road crack detection and characterization," *IEEE Transactions on Intelligent Transportation Systems*, vol. 14, no. 1, pp. 155–168, 2013.
- [3] Y. Huang and Y. Tsai, "Dynamic programming and connected component analysis for an enhanced pavement distress segmentation algorithm," *Transportation Research Record: Journal of the Transportation Research Board*, vol. 2225, no. 1, pp. 89–98, 2011.
- [4] M. Salman, S. Mathavan, K. Kamal, and M. Rahman, "Pavement crack detection using the Gabor filter," in *Proceedings of the 16th International IEEE Conference on Intelligent Transportation Systems (ITSC 2013)*, pp. 2039–2044, IEEE, Hague, The Netherlands, October 2013.
- [5] L. Zhang, F. Yang, Y. D. Zhang, and Y. J. Zhu, "Road crack detection using deep convolutional neural network," in *Proceedings of the 2016 IEEE International Conference on Image Processing (ICIP)*, pp. 3708–3712, IEEE, Phoenix, Arizona, September 2016.
- [6] D. Zhang, Q. Li, Y. Chen, M. Cao, L. He, and B. Zhang, "An efficient and reliable coarse-to-fine approach for asphalt pavement crack detection," *Image and Vision Computing*, vol. 57, pp. 130–146, 2017.
- [7] S. Teidj, A. Khamlichi, and A. Driouach, "Identification of beam cracks by solution of an inverse problem," *Procedia Technology*, vol. 22, pp. 86–93, 2016.
- [8] E. N. Chatzi, B. Hiriyyur, H. Waisman, and A. W. Smyth, "Experimental application and enhancement of the XFEM–



- GA algorithm for the detection of flaws in structures,” *Computers & Structures*, vol. 89, no. 7-8, pp. 556–570, 2011.
- [9] D. Rabinovich, D. Givoli, and S. Vigdergauz, “XFEM-based crack detection scheme using a genetic algorithm,” *International Journal for Numerical Methods in Engineering*, vol. 71, no. 9, pp. 1051–1080, 2007.
- [10] Y.-J. Cha, W. Choi, and O. Büyüköztürk, “Deep learning-based crack damage detection using convolutional neural networks,” *Computer-Aided Civil and Infrastructure Engineering*, vol. 32, no. 5, pp. 361–378, 2017.
- [11] Y. LeCun, “LeNet-5, convolutional neural networks (2015),” 2016.
- [12] D. E. Rumelhart, G. E. Hinton, and R. J. Williams, “Learning representations by back-propagating errors,” *Nature*, vol. 323, no. 6088, pp. 533–536, 1986.
- [13] Y. LeCun, B. Boser, J. S. Denker et al., “Backpropagation applied to handwritten zip code recognition,” *Neural Computation*, vol. 1, no. 4, pp. 541–551, 1989.
- [14] S. Ioffe and C. Szegedy, “Batch normalization: accelerating deep network training by reducing internal covariate shift,” 2015, <http://arxiv.org/abs/1502.03167>.
- [15] M. A. Vorontsov and V. P. Sivokon, “Stochastic parallel-gradient-descent technique for high-resolution wave-front phase-distortion correction,” *Journal of the Optical Society of America A*, vol. 15, no. 10, pp. 2745–2758, 1998.
- [16] D. P. Kingma and J. Ba, “Adam: a method for stochastic optimization,” 2014, <http://arxiv.org/abs/1412.6980>.
- [17] N. Srivastava, G. Hinton, A. Krizhevsky, I. Sutskever, and R. Salakhutdinov, “Dropout: a simple way to prevent neural networks from overfitting,” *The Journal of Machine Learning Research*, vol. 15, no. 1, pp. 1929–1958, 2014.
- [18] Dataset, <http://dx.doi.org/10.17632/5y9wdsg2zt.1#file-c0d86f9f-852e-4d00-bf45-9a0e24e3b932>.

## Research Article

# Hydration of Early Age Cement Paste with Nano-CaCO<sub>3</sub> and SAP by LF-NMR Spectroscopy: Mechanism and Prediction

Haitao Zhao <sup>1</sup>, Gaoyang Sun,<sup>2</sup> Lu Yu,<sup>3</sup> Kaidi Jiang,<sup>4</sup> Xiaodong Chen,<sup>5</sup> Ruiming Jia,<sup>6</sup> Yi Wan,<sup>7</sup> and Shihai Li<sup>8</sup>

<sup>1</sup>College of Materials Science and Engineering, Southeast University, Nanjing 211189, China

<sup>2</sup>Jiangsu Testing Center for Quality of Construction Engineering Co. Ltd., Nanjing 210028, China

<sup>3</sup>Nanjing Architectural Design & Research Institute Co. Ltd., Nanjing 210005, China

<sup>4</sup>College of Civil and Transportation Engineering, Hohai University, Nanjing 210098, China

<sup>5</sup>China Communications Construction Company Urban Investment Holding Co. Ltd., Guangzhou 510623, China

<sup>6</sup>Tong Yuan Design Group Co. Ltd., Jinan 250101, China

<sup>7</sup>Anhui Transport Consulting & Design Institute Co., Ltd., Hefei 230088, China

<sup>8</sup>Dalian Luneng Real Estate Co. Ltd., Dalian 116000, China

Correspondence should be addressed to Haitao Zhao; [hhuzhaoht@163.com](mailto:hhuzhaoht@163.com)

Received 20 June 2019; Accepted 25 July 2019; Published 14 August 2019

Guest Editor: Qing-feng Liu

Copyright © 2019 Haitao Zhao et al. This is an open access article distributed under the Creative Commons Attribution License, which permits unrestricted use, distribution, and reproduction in any medium, provided the original work is properly cited.

In this paper, by testing the evolution of the physically bound water using the low-field nuclear magnetic resonance (LF-NMR) technology, the hydration process of cement paste with nano-CaCO<sub>3</sub> (NC) and superabsorbent polymer (SAP) at early age is investigated. Results indicate that the hydration process can be divided into four periods according to the zero points of the second-order differential hydration curve: initial period, acceleration period, deceleration period, and steady period. Firstly, with the increase in the water to cement ratio, the starting time of the hydration period is delayed, and the duration becomes longer. Secondly, the addition of NC leads to the speedy arrival of each period and shortens the duration of each period in the hydration process, and the optimal NC content is 1.5%. Thirdly, with the increase in SAP content, the starting time of the hydration period is delayed and the duration becomes longer. Finally, based on the experimental results and the existing hydration model, the modified hydration model considering the content of NC and SAP is proposed.

## 1. Introduction

Concrete is the most widely used man-made construction material in the world, and the mechanical property and durability are focused in recent studies [1–5]. Nanomaterials, as products of nanotechnology, are defined as materials with particle sizes less than 100 nm and have many superior properties that differ from traditional materials [6, 7]. Nanomaterials can enhance the physical and mechanical properties of the cement-based materials effectively, reduce the porosity, and help in manufacturing the concrete with better performance [8]. The price of nano-SiO<sub>2</sub> [9], nano-Al<sub>2</sub>O<sub>3</sub> [10], nano-TiO<sub>2</sub> [11], and other materials are very expensive, which makes it difficult to be widely used in

cement-based materials. But NC has many advantages such as low price, small particle size, and large surface area, which can be filled with cement particles to make the microstructure more compact [12]. The research indicates that NC can promote hydration process and induce new hydration products [13]. Therefore, it is significant to study the effect of NC on the hydration process of cement-based materials. Furthermore, traditional external curing methods are not effective because the curing water penetrates only the surface layer of the concrete [14]. Internal curing with SAP is an effective method to reduce the decrease in internal relative humidity by supplying additional water [15] and to prevent the detrimental effects of shrinkage by producing a dense crack-free microstructure [16].

Scholars have done a series of experimental studies on the influence of NC or SAP on cement-based materials. Wang and Zhang [17] studied the effects of NC on the hydration properties of silicate cement by using the microthermograph method and the differential scanning thermal analysis. The results showed that the use of NC could promote the hydration and enhance the heat of hydration. Liu et al. [18] used the ultrasonic method to study the influence of NC on the performance of cement paste. The results showed that when the dosage of NC was 2%, the initial time and final time of concrete were shortened by 61 min and 39 min, respectively. So, the addition of NC can promote the hydration reaction of cement paste. Camiletti et al. [19] studied the effect of NC on the performance of super-high-performance concrete by using thermal analysis. The results indicated that NC accelerates the hydration process of cement by inducing nucleation effect. Esteves [20] studied the hydration degree of cement paste and mortar by using the differential thermogravimetric analysis. The results showed that SAP promoted cement hydration. Justs et al. [21] found that SAP promoted hydration of cement-based materials from 7 to 28 days. However, there is no research on the combined impact of NS and SAP on hydration of cement-based materials at present. Thus, the effects of NC and SAP on the hydration process of cement-based materials were investigated in this paper.

At present, there are many research methods of the early age hydration process such as ultrasonic method [22], resistivity method [23], hydrated thermal analysis method [24], and ultrasonic testing method [25]. These methods have made great progress in the study of hydration process. However, there are still many deep-seated mechanisms that have not been systematically solved, especially the interaction among various mineral hydration. Low-field nuclear magnetic resonance (LF-NMR) technology is utilized to study the hydration of cement-based materials by testing the evolution of the physically bound water [26, 27]. It is quick, continuous, and lossless. Apih et al. [28] found that the longitudinal relaxation time ( $T_1$ ) of the cement paste decreased with the progress of hydration, which could reveal the different periods of cement hydration. She et al. [29] measured the  $T_2$  signal intensity of the physically bound water in the cement paste and found that the evolution of  $T_2$  could well describe the hydration kinetics. The initial period, acceleration period, and steady period were characterized according to the different rates of change. Moreover, the reaction and the mechanism of each period were discussed based on the theory of cement chemistry.

In this paper, the effects of the water to cement ratio ( $w/c$ ), NC, and SAP on the hydration process of cement paste are tested and discussed based on LF-NMR. Furthermore, the modified hydration model considering the effects of NC and SAP is proposed.

## 2. Materials and Methods

**2.1. Materials.** In this experiment, P.II52.5 Portland cement with the specific surface area of  $350 \text{ m}^2/\text{kg}$  and density of  $3180 \text{ kg}/\text{m}^3$  was used. The chemical composition of cement is shown in Table 1. NC (Figure 1) with the purity of the NC of

above 95 wt.% and grain size ranging from 40 nm to 80 nm was used in this test. The polycarboxylic high-performance water-reducing agent produced by Sobute New Materials Company Ltd. (Nanjing, China) was used. However, the SAP (Figure 2) used in this study is an organic-inorganic polymer material and the water absorption capacity is 20 g water per gram of SAPs.

The influencing factors of the hydration are selected as  $w/c$ , NC content, and SAP content. The NC content is 1.0%, 1.5%, 2.0%, and 3.0% replacing the cement by weight. The dosage of SAP is 0.15% and 0.30% by mass of cement, and the  $w/c$  ratios are 0.30, 0.35, and 0.40. Furthermore, nine different cement compositions are designed (Table 2), and the time of each test is 96 hours.

In Table 2, SJ indicates that the cementitious material in the sample consists of cement only, and NC indicates that the cementitious material in the sample consists of cement and NC. For example, 0.30SJ\_NC015S15 represents a sample with a  $w/b$  value of 0.30, an NC content of 1.5%, and an SAP content of 0.15%.

**2.2. Specimen Preparation.** Cement paste specimens were mixed using a paddle mixer following a procedure which was similar to ASTM C-305 [30] as follows.

Cement and water and the admixture if necessary were weighed; sometimes one kind of particular admixture was added to water in a bowl. The mixture was initially mixed at 140 revolutions per minute (rpm) for 30 seconds. Taking a pause for 1 minute, meanwhile cement paste adhering to the sides of the mixing bowl was scraped. The entire mixture was mixed for another 2.5 minutes at 285 rpm. Then, the cement paste was cast into a glass tube with a height of 200 mm and a diameter of 27 mm until the height of samples were approximately 20–30 mm and then sealed with plastic film immediately after pouring.

**2.3. Testing Methods.** All of the experiments were carried out on a PQ001 LF-NMR with a magnetic field of 0.42 T and proton frequency field of 18 MHz. The room temperature was held constant at  $20 \pm 1^\circ\text{C}$ .

Before the test, the free induction decay (FID) sequence was calibrated on the oil sample to obtain the offset of RF signal frequency (O1) and the width of  $\pi/2$  pulse (P1). Then Carr-Purcell-Meiboom-Gill (CPMG) sequence ( $\pi/2-(\tau-\pi-\tau)$  n-TR) was applied to measure the transverse relaxation time  $T_2$  of pastes.  $\pi/2$  and  $\pi$  were pulses which could rotate the magnetization vector about the axis where pulses were applied. TR was the waiting time between two measurements, and  $n$  was the number of sampling data. The parameter settings for LF-NMR are given in Table 3.

By monitoring the  $T_2$  signal of physically bound water in cement paste using LF-NMR, the wave crest amplitude of the  $T_2$  signal,  $A(t)$ , is used to characterize the hydration process, as shown in Figure 3(a). Then the curve about  $A(t)$  in the unit mass of cement paste and different hydration time are obtained (Figure 3(b)). According to the zero point ( $b_1$ ,  $b_2$ , and  $b_3$ ) of the second-order differential curve (Figure 3(c)), the hydration process can be divided into four periods: initial period, acceleration period, deceleration period, and steady period, as shown in Figure 3(b).

TABLE 1: Chemical composition of cement.

Material	SiO <sub>2</sub>	Al <sub>2</sub> O <sub>3</sub>	Fe <sub>2</sub> O <sub>3</sub>	CaO	MgO	Na <sub>2</sub> O	K <sub>2</sub> O	SO <sub>3</sub>	TiO <sub>2</sub>	LOI
Cement	19.53	4.31	2.89	63.84	1.25	0.13	0.64	3.25	0.26	3.0

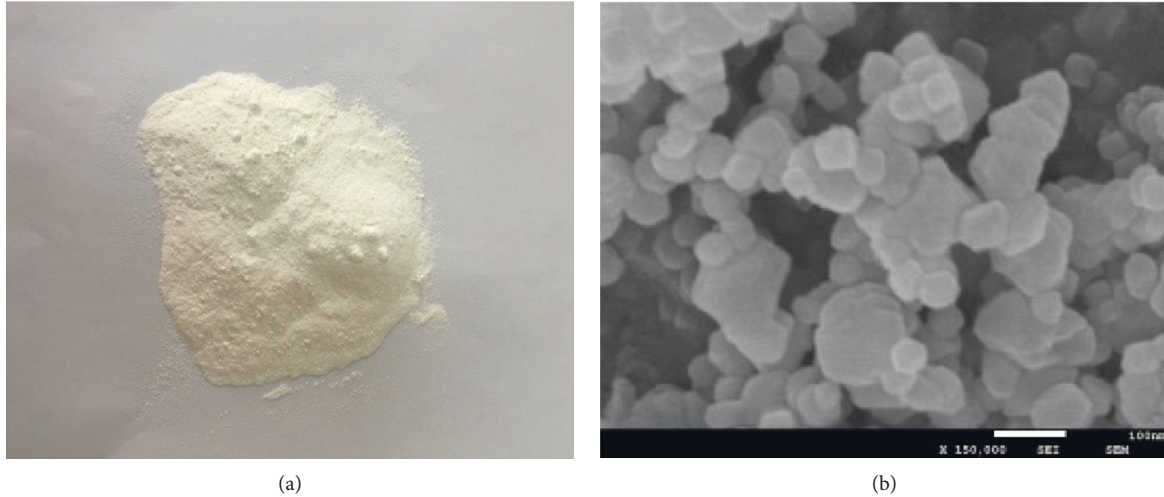


FIGURE 1: NC diagram. (a) NC powder. (b) SEM image of NC.



FIGURE 2: SAP.

### 3. Results and Discussion

**3.1. Effect of  $w/c$  on the Hydration Process.** Figure 4 shows the curves of  $T_2$  signal amplitude in unit mass with different  $w/c$ . The larger the  $w/c$  is, the more physically bound water in the unit mass of cement paste contains. According to the method introduced above, the test data are treated as differential treatment, and then the time cutoff point of the four periods is obtained. The results are shown in Figure 4 and Table 4.

It can be seen from Figure 4 that the unit signal amplitude of three cement pastes decreases with age. In the early stage of the initial phase,  $C_3A$  (tricalcium aluminate), the most active in cement, has begun to react with water. And the hydrated product is encapsulated on the cement surface to form a gel protective film. In the later stage of the initial phase, the gel protective layer like the permeable membrane only allows water molecules to enter the protective layer. But it does not allow  $Ca^{2+}$  and  $OH^-$  ions to go through the protective layer. Further progress of the hydration reaction is prevented. At the

end of the initial phase, the  $T_2$  signal amplitude of the samples 0.30SJ, 0.35SJ, and 0.40SJ decreases to 471.3 a.u./g, 649.3 a.u./g, and 805.6 a.u./g, respectively. At any time of this stage, the  $T_2$  signal amplitude in unit mass increases as the  $w/c$  increases. The reason is that the greater the  $w/c$ , the more the water contained in the per unit mass of cement paste, and the greater the detection of physically bound water signal.

The duration of the initial period of the samples 0.30SJ, 0.35SJ, and 0.40SJ is 1.65 h, 1.872 h, and 2.033 h, respectively. The larger the  $w/c$  is, the longer the initial period is. The reason is perhaps that the larger the  $w/c$ , the lower the  $Ca^{2+}$  concentration in the solution, which increases the degree of cement hydration. Furthermore, larger  $w/c$  delays  $Ca^{2+}$  to reach the time of super saturation, prolonging the initial period. At the end of the initial period, the protective layer of the gel layer produced in the previous stage ruptures due to the change in permeability. The new cement surface comes into contact with water, and the acceleration period begins.

At the acceleration stage,  $Ca^{2+}$  achieves super saturation, which makes  $Ca^{2+}$  crystal to precipitate and promotes the hydration of  $C_3S$  (tricalcium silicate). Water is rapidly consumed, and the signal quantity decreases quickly. At the end of the acceleration period, the  $T_2$  signal amplitude of the samples 0.30SJ, 0.35SJ, and 0.40SJ decreases to 402.3 a.u./g, 564.7 a.u./g, and 705.3 a.u./g, respectively. The decreasing rates are 21.1 a.u./g/h, 24.5 a.u./g/h, and 27.5 a.u./g/h, respectively. It indicates that the larger the  $w/c$  is, the faster the hydration rate is.

At the end of the acceleration period, the hydration product has been produced in large quantity. The hydration products have been accumulated and formed on the outer shell of the protective layer. These shells are connected to each other to form a mesh structure. The  $T_2$  signal amplitude of the samples 0.30SJ, 0.35SJ, and 0.40SJ reduces to 162.3 a.u./g, 277.0 a.u./g, and

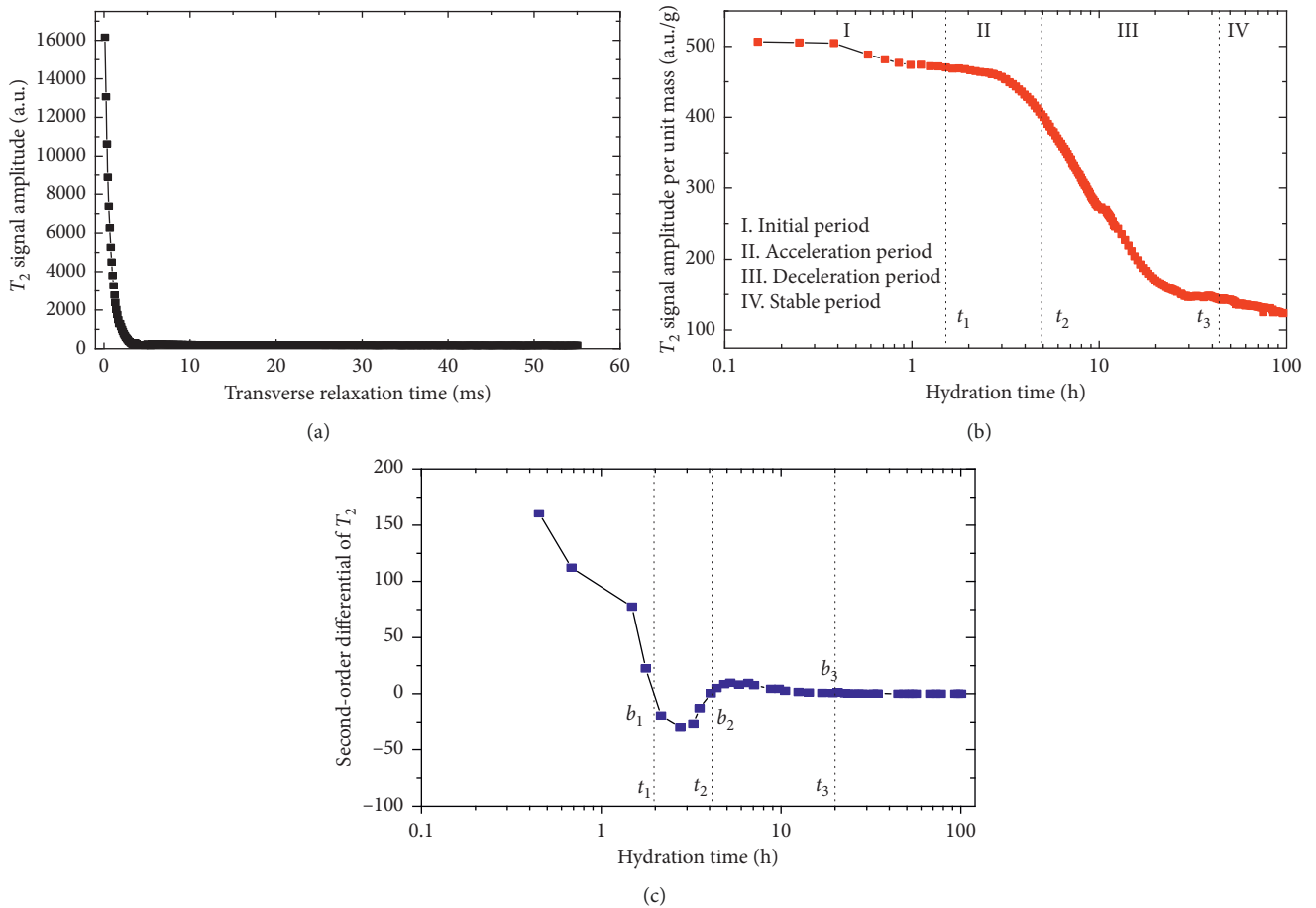


TABLE 2: Mix proportion of cement pastes.

Sample	w/b	Dosage of NC (%)	Dosage of SAP (%)	Influencing factor
0.30SJ	0.30	0	0	w/c
0.35SJ	0.35	0	0	
0.40SJ	0.40	0	0	
0.30SJ_NC010	0.30	1.0	0	NC content
0.30SJ_NC015	0.30	1.5	0	
0.30SJ_NC020	0.30	2.0	0	
0.30SJ_NC030	0.30	3.0	0	
0.30SJ_NC015S15	0.30	1.5	0.15	SAP content
0.30SJ_NC015S30	0.30	1.5	0.30	

TABLE 3: Parameter settings for LF-NMR.

Sequence	TD	SW	RFD	RG1	DRG1	PRG	TW	NS	NECH	TE	DL1
FID	1024	100	0.02	20	3	2	2000	4	—	—	—
CPMG	Automatic settings	250	0.005	10	3	2	200	16	500	0.11	500

FIGURE 3: Schematic diagram of hydration process. (a) First wave crest amplitude of ( $T_2$ ) signal. (b) The first peak amplitude  $A(t)$  in unit mass changes with time. (c) Second-order differential of  $A(t)$ .

371.1 a.u./g, respectively. The reason is that the larger the w/c, the more the water contained in the cement gap and pore diameter in the cement paste, and the more the presence of physically bound water.

At the end of the deceleration period, the  $T_2$  signal amplitude of the samples 0.30SJ, 0.35SJ, and 0.40SJ decreases

to 124.7 a.u./g, 203.2 a.u./g, and 266.3 a.u./g, respectively. The  $T_2$  signal amplitude in unit mass is very small and tends to be stable, and the rate of hydration process is very slow. The time of the steady period of the samples 0.30SJ, 0.35SJ, and 0.40SJ is 50.583 h, 52.815 h, and 54.117 h, respectively. The larger the w/c, the longer the time requires to reach the steady period.

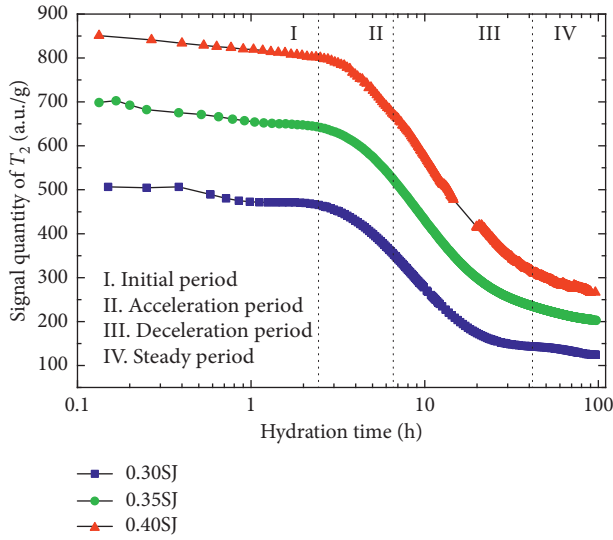


FIGURE 4: Effects of different w/c on the hydration process.

TABLE 4: The hydration period separation time of pure cement pastes with different w/c.

Sample	$t_1$ (h)	$t_2$ (h)	$t_3$ (h)	$(0\sim t_1)$	$(t_2\sim t_3)$	$(t_3\sim)$
0.30NC0	1.65	4.977	50.583	1.65	3.327	45.606
0.35NC0	1.872	5.324	52.815	1.517	3.452	47.491
0.40NC0	2.033	5.677	54.117	0.867	3.644	48.44

3.2. *Effect of NC on the Hydration Process.* The curves of  $T_2$  signal amplitude in unit mass of cement paste with an NC dosage of 0%, 1.0%, 1.5%, 2.0%, and 3.0% with hydration time are shown in Figure 5. According to the same division method of the hydration process abovementioned, the hydration process is divided into four periods, and each period duration is listed in Table 5. For cement paste with same w/c, the addition of NC makes the  $T_2$  signal amplitude in unit mass stronger. As binder materials continuously hydrate,  $T_2$  signal amplitude in all samples is on the decline with different rates. But different dosages of NC have an obviously distinct influence on each period.

It can be observed in Figure 5 that with the increase of NC content, the  $T_2$  signal amplitude gradually increases, and the increase rate is not proportional. At the beginning of the initial period, the  $T_2$  signal amplitude of the samples 0.30SJ, 0.30SJ\_NC010, 0.30SJ\_NC015, 0.30SJ\_NC020, and 0.30SJ\_NC030 is 506.78 a.u./g, 521.95 a.u./g, 542.92 a.u./g, 598.71 a.u./g, and 662.52 a.u./g, respectively. Compared with the baseline group, the  $T_2$  signal amplitude of NC cement paste increases 15.17 a.u./g, 36.14 a.u./g, 91.93 a.u./g, and 155.74 a.u./g, respectively. And the corresponding growth rates are 3.0%, 7.13%, 18.14%, and 30.73%, respectively. There is no corresponding linear relationship. NC particle size ranges from 40 nm to 80 nm, which can be filled in small pores to function as microaggregates, so that the relative content of water in the pores is reduced and the free water of the surface involved in the reaction relatively increases. When the amount of NC is increased, more porous pores are filled and more free surface water content exists.

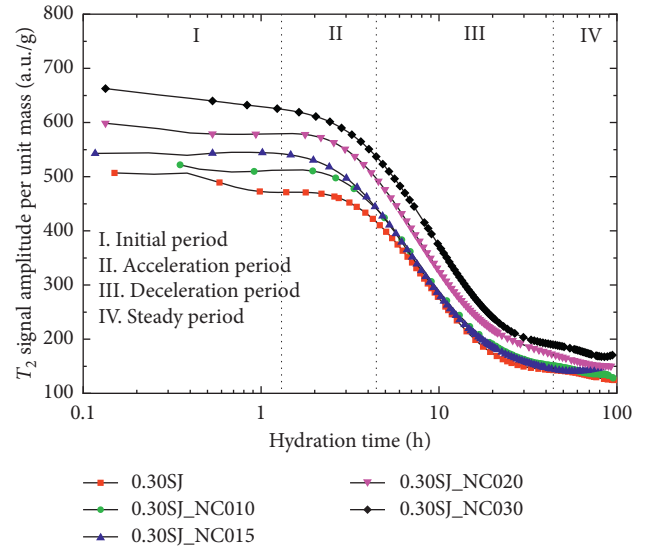


FIGURE 5: Effects of different NC dosages on the hydration process.

TABLE 5: The hydration period separation time of cement pastes with different NC dosages.

Sample	$t_1$ (h)	$t_2$ (h)	$t_3$ (h)	$(0\sim t_1)$	$(t_2\sim t_3)$	$(t_3\sim)$
0.3NC0	1.65	4.977	50.583	1.65	3.327	45.606
0.3NC1.0	1.517	4.817	48.8	1.517	3.3	43.983
0.3NC1.5	1.167	4.317	42.117	1.167	3.15	37.8
0.3NC2.0	1.342	4.587	46.357	1.342	3.245	41.77
0.3NC3.0	1.233	4.465	45.516	1.233	3.232	41.051

It can obviously be seen in Table 5 that during the hydration process, with the addition of NC, the duration of four stages are all shortened. When the NC content is 1.5%, the starting time of each hydration period is the earliest and thus the duration of each period is the shortest. Therefore, the addition of NC can promote the hydration process of cement paste, and the optimal NC content is 1.5%. The conclusion is similar with the previous study of hydration process [31]. The duration of the initial period of the samples 0.30SJ, 0.30SJ\_NC010, 0.30SJ\_NC015, 0.30SJ\_NC020, and 0.30SJ\_NC030 is 1.65 h, 1.517 h, 1.167 h, 1.342 h, and 1.233 h, respectively. At the beginning of the acceleration period, the  $T_2$  signal amplitude of the samples 0.30SJ, 0.30SJ\_NC010, 0.30SJ\_NC015, 0.30SJ\_NC020, and 0.30SJ\_NC030 is 471.31 a.u./g, 512.51 a.u./g, 545 a.u./g, 579.55 a.u./g, and 625.60 a.u./g, respectively. At the end of the acceleration period, the  $T_2$  signal amplitude is 402.31 a.u./g, 431.83 a.u./g, 444.8 a.u./g, 491.57 a.u./g, and 537.18 a.u./g, respectively.

There are several reasons for abovementioned phenomenon [32]. Firstly, the particle size of NC is in nanometer, and its strong surface activity can change the distribution of cement particles. The microaggregate effect can increase the relative content of free water so as to increase the contact area between cement particles and water. Secondly, NC makes the diffused  $\text{Ca}^{2+}$  to accumulate on its particle surface, decreasing the nearby  $\text{Ca}^{2+}$  concentration and accelerating the chemical reaction of  $\text{C}_3\text{S}$ , which promotes the hydration process. Thirdly, NC has a high

chemical activity to increase the distribution of cement particles, increasing the contact area between water and cement particles. Finally, when NC contacts  $C_3A$ , a small amount of calcium aluminate ( $CaCO_3 \cdot C_3A \cdot H_2O$ ) is produced. It can make water molecules and other particles spread so as to accelerate the hydration process. However, when the content of NC is over 1.5%, the phenomenon of “bleeding” may occur and the active influence on the hydration process falls. So, the optimal NC content is 1.5%.

**3.3. Effect of SAP on the Hydration Process.** The curves of the  $T_2$  signal amplitude of cement paste with different SAP content are presented in Figure 6. According to the same division method introduced above, each period’s duration is shown in Table 6.

It can be seen from Figure 6 that, in the four stages of hydration process, with the increase of SAP content, the  $T_2$  signal amplitude gradually increases. At the end of the initial period, the  $T_2$  signal amplitude of the samples 0.30SJ\_NC015, 0.30SJ\_NC015S15, and 0.30SJ\_NC015S30 is 534.022 a.u./g, 698.244 a.u./g, and 756.576 a.u./g, respectively. The pre-absorbent of water in SAP introduces extra water, which releases moisture due to the concentration difference and self-drying. Thus, the amount of physical bound water is greater.

It can be observed in Table 6 that, with the increase in SAP content, the starting time of each hydration period is also delayed and thus the duration of each period is prolonged. The starting time of the deceleration period of the samples 0.30SJ\_NC015, 0.30SJ\_NC015S15 and 0.30SJ\_NC015S30 is 4.317 h, 4.433 h, and 4.583 h, respectively. Thus, the duration is 42.117 h, 43.067 h, and 43.3 h, respectively. SAP continuously releases moisture to promote the hydration process [33]. It makes the total w/c larger. With the proceeding of hydration, the relative concentration of  $Ca^{2+}$  per unit volume decreases, and the time to reach the saturation state prolongs.

In addition, it can obviously be seen from Figure 6 that the  $T_2$  signal amplitude of NC cement paste mixed with SAP continued to decline at the steady period. However, the  $T_2$  signal amplitude without SAP is almost constant. Taking hydration time from 82 h to 96 h, for example, the  $T_2$  signal amplitude of the samples 0.30SJ\_NC015, 0.30SJ\_NC015S15, and 0.30SJ\_NC015S30 is 0.347 a.u./g, 7.782 a.u./g, and 6.353 a.u./g. The descending rates are 0.025 a.u./g/h, 0.556 a.u./g/h, and 0.454 a.u./g/h. With the proceeding of hydration, the free water in the cement paste is continuously consumed. SAP gradually releases moisture due to poor concentration of capillary solution, humidity difference, and capillary tensile stress [28]. The results are consistent with previous studies [34].

### 3.4. Hydration Model

**3.4.1. Hydration Model for Pure Cement Paste.** The hydration model can be used to describe and predict the development of hydration. The Avrami–Erofeev equation [35] is the classic overall kinetic equation and has many significant advantages, such as a more simplified expression and less parameters. The Avrami–Erofeev equation is as follows:

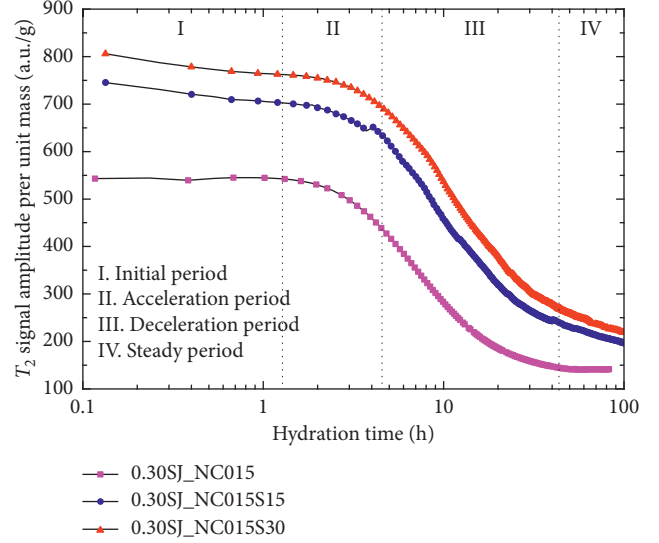


FIGURE 6: Effects of different SAP dosages on the hydration process.

TABLE 6: The hydration period separation time of cement pastes with different SAP dosages.

Sample	$t_1$ (h)	$t_2$ (h)	$t_3$ (h)	(0~ $t_1$ )	( $t_2$ ~ $t_3$ )	( $t_3$ ~)
0.3NC1.5	1.167	4.317	42.117	1.167	3.15	37.8
0.3NC1.5S0.15	1.233	4.433	43.067	1.233	3.2	38.634
0.3NC1.5S0.3	1.367	4.583	43.3	1.367	3.216	38.717

$$\alpha(t) = 1 - \exp(-(kt)^n), \quad (1)$$

where  $\alpha(t)$  is the degree of hydration,  $k$  and  $n$  are the empirical parameters, and  $t$  is the time of cement paste hydration.

On the basis of this model, the variation law of  $T_2$  with time is described. And the hydration process is characterized by transverse relaxation time. The expression of the  $T_2$  signal amplitude over time is as follows:

$$T(t) = a - b \exp(-ct), \quad (2)$$

where  $T(t)$  is the  $T_2$  signal amplitude of unit mass of cement paste hydration at  $t$  moment and  $a$ ,  $b$ , and  $c$  are the model parameters, which depend on mineral compositions, w/c, etc.

The experiment data and fitting curves of pure cement pastes with different w/c are given in Figure 7. The fitted results including fitting parameters and correlation are listed in Table 7.

$$a = 561.71 - 2716.32 \ln(w/c) - \frac{1110.51}{w/c},$$

$$b = -3140.24 + 11138.79 (w/c)^3 + \frac{727.71}{(w/c)}, \quad (3)$$

$$c = 0.22 - 0.38 \ln(w/c) - \frac{0.32}{(w/c)^{0.5}},$$

where the w/c ranges from 0.3 to 0.4 and the hydration time  $t$  ranges from 0 h to 110 h.

As presented in Table 7, the correlation of experiment data and fitting curves is all over 0.99, and equation (2) could

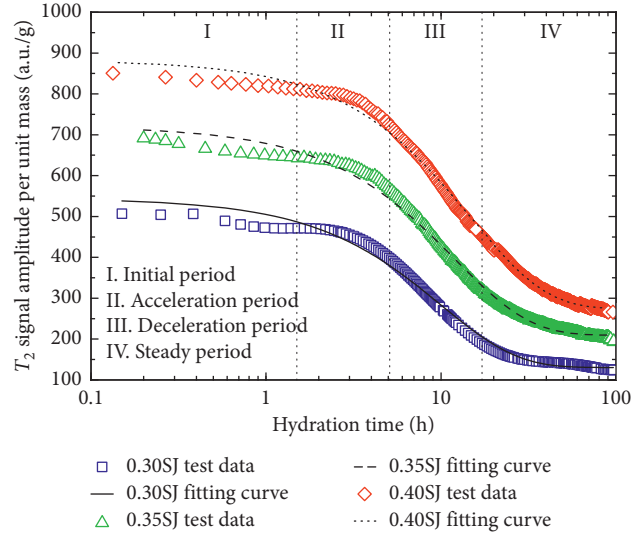


FIGURE 7: Experiment data and fitting curves of pure cement pastes with different w/c.

TABLE 7: Fitting parameters and correlation of pure cement pastes with different w/c.

Sample	$a$	$b$	$c$	Correlation
0.3NC0	130.385	-413.786	0.0996	0.9975
0.35NC0	240.477	-583.487	0.0840	0.9972
0.4NC0	274.374	-608.077	0.0679	0.9983

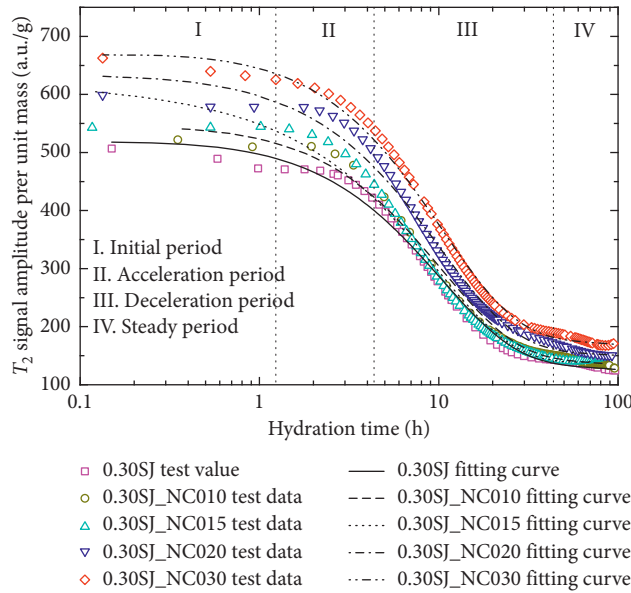


FIGURE 8: Experiment data and fitting curves of cement pastes with different NC dosages.

describe the hydration process of pure cement pastes very well. According to Table 7, the relations of  $a$ ,  $b$ , and  $c$  with w/c are proposed by regression analysis.

**3.4.2. Modification of Hydration Model.** The hydration model above only describes the hydration process of the neat cement paste. The effect of NC and SAP on the hydration process of cement paste is not mentioned.

Through the hydration model obtained in Section 3.4.1, it can be found that it has the advantages such as simple expression, few parameters, and simple calculation. Therefore, this section modifies the hydration model based on the Avrami–Erofeev model. The expression is as follows:

$$T(t) = \gamma_{\text{SAP}} \gamma_{\text{NC}} [a - b \exp(-ct)], \quad (4)$$

TABLE 8: Fitting parameters and correlation of cement pastes with different NC dosages.

Sample	$A_{NC}$	$B_{NC}$	$C_{NC}$	Correlation
0.3NC0	0.911	-0.0011	0.075	0.9955
0.3NC1.0	0.945	-0.0014	0.093	0.9929
0.3NC1.5	1.195	0.0017	-0.111	0.9907
0.3NC2.0	1.1479	-0.0007	0.036	0.9895
0.3NC3.0	1.1601	-0.0014	0.118	0.9946

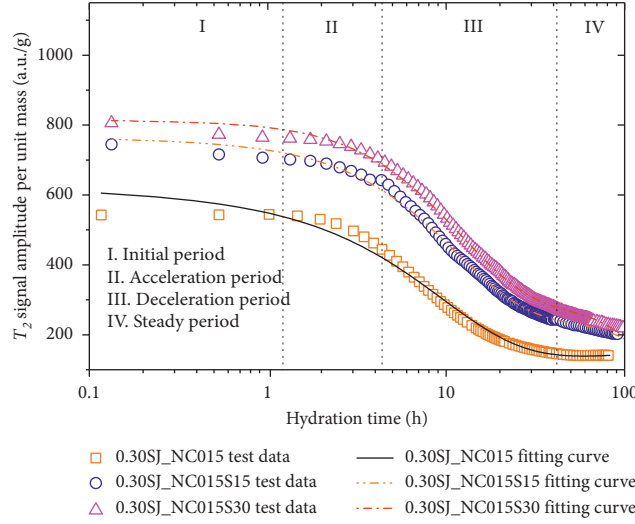


FIGURE 9: Experiment data and fitting curves of cement pastes with different SAP dosages.

where  $\gamma_{NC}$  and  $\gamma_{SAP}$  are the parameters which are related to the dosage of NC and SAP.

The experiment data and fitting curves of cement pastes with different NC dosages are shown in Figure 8. The fitted results including fitting parameters and correlation are listed in Table 8.

As presented in Table 8, the correlation of experiment data and fitting curves is all over 0.99, and equation (4) could well describe the hydration process of cement pastes with different NC dosages. According to Table 8, the relations of  $A_{NC}$ ,  $B_{NC}$ , and  $C_{NC}$  with NC content ( $m_{NC}$ ) are proposed by regression analysis:

$$\begin{aligned} \gamma_{NC} &= A_{NC} + B_{NC}t + C_{NC}t^{0.19}, \\ A_{NC} &= \frac{m_{NC}}{m_{NC} - 0.935} - \frac{0.857}{m_{NC} - 0.941} + 0.04m_{NC}, \\ B_{NC} &= \frac{8.722m_{NC} - 0.001}{m_{NC} - 1.45}, \\ C_{NC} &= \frac{0.07 - 0.02m_{NC}^2}{1 - 0.58m_{NC}^2 + 0.036m_{NC}^4}, \end{aligned} \quad (5)$$

where the NC content  $m_{NC}$  ranges from 0.01 to 0.03% and the hydration time  $t$  ranges from 0 h to 110 h.

The experimental data and fitting curves of cement pastes with different SAP dosages are shown in Figure 9. The fitted results including fitting parameters and correlation are listed in Table 9.

TABLE 9: Fitting parameters and correlation of cement pastes with different SAP dosages.

Sample	$A_{SAP}$	$B_{SAP}$	$C_{SAP}$	$\gamma_{SAP}$	Correlation
0.3NC1.5	1.017	-0.032	0.115	1.0572	0.994
0.3NC1.5S0.15	1.236	-0.042	0.135	1.0572	0.998
0.3NC1.5NC0.3	1.312	-0.062	0.196	1.0572	0.998

As presented in Table 8, the correlation of experiment data and fitting curves is all over 0.99 and the equation (4) could well describe the hydration process of cement pastes with different SAP dosages. According to Table 9, the relations of  $A_{SAP}$ ,  $B_{SAP}$ , and  $C_{SAP}$  with SAP content ( $m_{SAP}$ ) are proposed by regression analysis:

$$\begin{aligned} \gamma_{SAP} &= A_{SAP} + B_{SAP}t + C_{SAP}t^{0.75}, \\ A_{SAP} &= 3.84 - 1.68m - 2.73 \exp(-m_{SAP}), \\ B_{SAP} &= 0.02 - 0.43m^3 - 0.053 \exp(m_{SAP}), \\ C_{SAP} &= -0.07 + 0.78m^{1.5} + 0.18 \exp(-m_{SAP}), \end{aligned} \quad (6)$$

where the SAP content  $m_{SAP}$  ranges from 0 to 0.3% and the hydration time  $t$  ranges from 0 h to 110 h.

## 4. Conclusions

From the materials and measurement methods used in this study, the following conclusions can be drawn:



- (1) With the development of hydration reaction,  $T_2$  signal amplitude in unit mass of different cement pastes always decreases with age, and the hydration process of the cement paste can be divided into four periods according to the second-order differential zero point of the curve: initial period, acceleration period, deceleration period, and steady period. The larger the w/c is, the greater the  $T_2$  signal amplitude in unit mass is. And the increase of the w/c delays the arrival of the acceleration period, deceleration period, and steady period, and hence, the periods of initial, acceleration, and deceleration last longer.
- (2) With the addition of NC in the cement paste, the  $T_2$  signal amplitude increases, the arrival of each period is faster, and hence, the duration of each period becomes shorter. When the content of NC exceeds 1.5%, the effect of promoting the hydration process is weakened. So, the optimal content of NC is 1.5%.
- (3) The addition of SAP increases the  $T_2$  signal amplitude of the cement paste, and the  $T_2$  signal amplitude increases as the SAP content increases, but the arrival of the acceleration period, deceleration period, and steady period delays, thus prolonging the duration of the initial period, acceleration period, and deceleration period.
- (4) Based on the Avrami-Erofeev model, combined with the change in the  $T_2$  signal amplitude with the hydration time, the hydration model considering the NC content and the SAP content is proposed. The results of the model are in good agreement with the experimental data.

## Data Availability

The data used to support the findings of this study are available from the corresponding author upon request.

## Conflicts of Interest

The authors declare that they have no conflicts of interest.

## Acknowledgments

The authors gratefully acknowledge the financial supports from the Jiangsu Planned Projects for Postdoctoral Research Funds under Grant no. 1501013C.


## References

- [1] W. Qiang, W. Dengquan, and C. Honghui, "The role of fly ash microspheres in the microstructure and macroscopic properties of high-strength concrete," *Cement and Concrete Composites*, vol. 83, pp. 125–137, 2017.
- [2] Q.-F. Liu, G.-L. Feng, J. Xia, J. Yang, and L.-Y. Li, "Ionic transport features in concrete composites containing various shaped aggregates: a numerical study," *Composite Structures*, vol. 183, pp. 371–380, 2018.
- [3] X. H. Shen, Q. F. Liu, Z. Hu, W. Q. Jiang, X. Lin, and D. Hou, "Combine ingress of chloride and carbonation in marine-exposed concrete under unsaturated environment: a numerical study," *Ocean Engineering*, 2019.
- [4] L. X. Mao, Z. Hu, J. Xia et al., "Multi-phase modelling of electrochemical rehabilitation for ASR and chloride affected concrete composites," *Composite Structures*, vol. 207, pp. 176–189, 2019.
- [5] X. H. Shen, W. Q. Jiang, D. Hou, Z. Hu, J. Yang, and Q. F. Liu, "Numerical study of carbonation and its effect on chloride binding in concrete," *Cement & Concrete Composites*, 2020.
- [6] D. Hou, J. Yu, and P. Wang, "Molecular dynamics modeling of the structure, dynamics, energetics and mechanical properties of cement-polymer nanocomposite," *Composites Part B: Engineering*, vol. 162, pp. 433–444, 2019.
- [7] W. Li, Z. Huang, F. Cao, Z. Sun, and S. P. Shah, "Effects of nano-silica and nano-limestone on flowability and mechanical properties of ultra-high-performance concrete matrix," *Construction and Building Materials*, vol. 95, pp. 366–374, 2015.
- [8] M. S. M. Norhasri, M. S. Hamidah, and A. M. Fadzil, "Morphology and strength of cement paste from clay as nanomaterial," *Applied Mechanics and Materials*, vol. 490–491, pp. 19–24, 2014.
- [9] B. W. Jo, C. H. Kim, and J. H. Lim, "Investigations on the development of powder concrete with nano-SiO<sub>2</sub> particles," *KSCE Journal of Civil Engineering*, vol. 11, no. 1, pp. 37–42, 2007.
- [10] S. Barbhuiya, S. Mukherjee, and H. Nikraz, "Effects of nano-Al<sub>2</sub>O<sub>3</sub> on early-age microstructural properties of cement paste," *Construction and Building Materials*, vol. 52, pp. 189–193, 2014.
- [11] L. C. Feng, C. W. Gong, Y. P. Wu, D. C. Feng, and N. Xie, "The study on mechanical properties and microstructure of cement paste with nano-TiO<sub>2</sub>," *Advanced Materials Research*, vol. 629, pp. 477–481, 2012.
- [12] T. Sato and J. J. Beaudoin, "Effect of nano-CaCO<sub>3</sub> on hydration of cement containing supplementary cementitious materials," *Advances in Cement Research*, vol. 23, no. 1, pp. 33–43, 2011.
- [13] B. W. Langan, K. Weng, and M. A. Ward, "Effect of silica fume and fly ash on heat of hydration of Portland cement," *Cement and Concrete Research*, vol. 32, no. 7, pp. 1045–1051, 2002.
- [14] S. Zhuovsky, K. Kovler, and A. Bentur, "Revisiting the protected paste volume concept for internal curing of high-strength concretes," *Cement and Concrete Research*, vol. 41, no. 9, pp. 981–986, 2011.
- [15] D. Shen, X. Wang, D. Cheng, J. Zhang, and G. Jiang, "Effect of internal curing with super absorbent polymers on autogenous shrinkage of concrete at early age," *Construction and Building Materials*, vol. 106, pp. 512–522, 2016.
- [16] P. Lura, M. Wyrzykowski, C. Tang, and E. Lehman, "Internal curing with lightweight aggregate produced from biomass-derived waste," *Cement and Concrete Research*, vol. 59, pp. 24–33, 2014.
- [17] C. Wang and C. Zhang, "The effect of nano-CaCO<sub>3</sub> on the hydration properties of Portland cement," *Silicate Bulletin*, vol. 35, no. 3, pp. 824–830, 2016, in Chinese.
- [18] X. Liu, L. Chen, A. Liu, and X. Wang, "Effect of nano-CaCO<sub>3</sub> on properties of cement paste," *Energy Procedia*, vol. 16, pp. 991–996, 2012.
- [19] J. Camilletti, A. M. Soliman, and M. L. Nehdi, "Effects of nano- and micro-limestone addition on early-age properties of ultra-high-performance concrete," *Materials and Structures*, vol. 46, no. 6, pp. 881–898, 2013.

- [20] L. P. Esteves, *Internal curing in cement-based materials*, Ph.D. thesis, Aveiro University, Aveiro, Portugal, 2009.
- [21] J. Justs, M. Wyrzykowski, D. Bajare, and P. Lura, "Internal curing by superabsorbent polymers in ultra-high performance concrete," *Cement and Concrete Research*, vol. 76, pp. 82–90, 2015.
- [22] G. Trtnik, G. Turk, F. Kavčič, and V. B. Bosiljkov, "Possibilities of using the ultrasonic wave transmission method to estimate initial setting time of cement paste," *Cement and Concrete Research*, vol. 38, no. 11, pp. 1336–1342, 2008.
- [23] Z. Bosiljkov and W. Li, "Contactless, transformer-based measurement of the resistivity of materials," pp. 10–28, 2003, US Patent: 6639401.
- [24] V. Balek, "The hydration of cement investigated by emanation thermal analysis," *Thermochimica Acta*, vol. 72, no. 1-2, pp. 147–158, 1984.
- [25] Ö. K. Keskin, İ. O. Yaman, and M. Tokyay, "Effects of experimental parameters in monitoring the hydration of cement mortars by ultrasonic testing," in *Nondestructive Testing of Materials and Structures*, pp. 437–443, Springer, Dordrecht, Netherlands, 2013.
- [26] C. Zhou, F. Ren, Q. Zeng, L. Xiao, and W. Wang, "Pore-size resolved water vapor adsorption kinetics of white cement mortars as viewed from proton NMR relaxation," *Cement and Concrete Research*, vol. 105, pp. 31–43, 2018.
- [27] C. Zhou, F. Ren, Z. Wang, W. Chen, and W. Wang, "Why permeability to water is anomalously lower than that to many other fluids for cement-based material?," *Cement and Concrete Research*, vol. 100, pp. 373–384, 2017.
- [28] T. Apih, G. Lahajnar, A. Sepe et al., "Proton spin-lattice relaxation study of the hydration of self-stressed expansive cement," *Cement and Concrete Research*, vol. 31, no. 2, pp. 263–269, 2001.
- [29] A. She, W. Yao, and Y. Wei, "In-situ monitoring of hydration kinetics of cement pastes by low-field NMR," *Journal of Wuhan University of Technology*, vol. 25, no. 4, pp. 692–695, 2010.
- [30] ASTM, *Standard Practice for Mechanical Mixing of Hydraulic Cement Pastes and Mortars of Plastic Consistency*, ASTM, West Conshohocken, PA, USA, 1999.
- [31] H. S. Yang, Y. J. Che, and M. Zhang, "Effect of nano-CaCO<sub>3</sub>/limestone powder composite on the early age cement hydration products," *Key Engineering Materials*, vol. 703, pp. 354–359, 2016.
- [32] S. W. M. Supit and F. U. A. Shaikh, "Effect of nano-CaCO<sub>3</sub> on compressive strength development of high volume fly ash mortars and concretes," *Journal of Advanced Concrete Technology*, vol. 12, no. 6, pp. 178–186, 2014.
- [33] B. Craeye, *Reduction of Autogenous Shrinkage of Concrete by Means of Internal Curing*, Ghent University, Ghent, Belgium, 2006.
- [34] L. Dudziak and V. Mechtcherine, "Reducing the cracking potential of ultra-high performance concrete by using super absorbent polymers (SAP)," in *Advances in Cement-Based Materials*, pp. 11–19, CRC Press, Boca Raton, FL, USA, 2010.
- [35] K. Van Breugel, *Simulation of Hydration and Formation of Structure in Hardening Cement-Based Materials*, Delft University of Technology, Delft, Netherlands, 1991.

## Research Article

# Modeling of the Axial Load Capacity of RC Columns Strengthened with Steel Jacketing under Preloading Based on FE Simulation

Ahmed M. Sayed <sup>1,2</sup> and Hesham M. Diab<sup>1</sup>

<sup>1</sup>Department of Civil Engineering, Engineering Faculty, Assiut University, Assiut, Egypt

<sup>2</sup>Department of Civil and Environmental Engineering, College of Engineering, Majmaah University, Al Majmaah 11952, Saudi Arabia

Correspondence should be addressed to Ahmed M. Sayed; [emc\\_elngaoy@yahoo.com](mailto:emc_elngaoy@yahoo.com)

Received 4 January 2019; Accepted 15 February 2019; Published 4 March 2019

Guest Editor: Qing-feng Liu

Copyright © 2019 Ahmed M. Sayed and Hesham M. Diab. This is an open access article distributed under the Creative Commons Attribution License, which permits unrestricted use, distribution, and reproduction in any medium, provided the original work is properly cited.

Reinforced concrete (RC) columns often require consolidation or rehabilitation to enhance their capacity to endure the loads applied. This paper aims at studying the conduct and capacity of RC square columns, those reinforced with steel jacketing under static preloads. For this purpose, a three-dimensional model of finite element (FE) is devised mainly to investigate and analyze the effect of this case. The model was tested and adjusted to ensure its accuracy using the previous experimental results obtained by the author. Results of testing, experimentally, the new developed FE model revealed the ability to use the model for calculating RC columns' axial load capacity and for predicting accurate failure modes. The new model that tends to predict the axial load capacity was suggested considering the parametric analysis results.

## 1. Introduction

Reinforced concrete (RC) columns often require strengthening to enhance their axial load capacity to endure loads. This reinforcement may be needed because of the alteration in the use which ended in addition to loads that are live; errors of design, problems in the construction while making erection, elevating for confirming to existing code necessities or aging of RC columns itself were studied.

There are three commonly used methods for reinforcing RC columns including concrete and/or steel jacketing and fiber-strengthened polymer (FRP) jacketing. All these methods have led to an effective rise in the load capacity of RC columns. This study refers to RC columns loaded by axial compressive load strengthened under load by steel jacketing. Strengthened existing steel columns under preloading through welding steel plates is frequently rendered [1, 2], but there is hardly any study of RC columns under preloading exists. Some researchers [3–10] reproduced the findings of

an experimental test chain on some RC columns fortified with the angles of steel jacketing under axial load without preloading. There was a witness confirming that the jacketing of steel enhances the failure load of the fortified RC columns.

Because the existing experimental research [3–10] ignores the effect of the preloading that found when the strengthening is done on the axial load capacity, reliance on the research that already exists is problematic for an accurate prediction of the axial load capacity relating to RC columns reinforced with steel jacketing under preloading. Moreover, the existing codes ACI Committee 318 [11] and Eurocode 4 [12] only predict the axial load capacity, based on the composite concrete-steel structure without preloading effect.

Other studies [13–16], using FE modeling, revealed that the conduct of RC members can be simulated precisely, especially the RC members that was strengthened by steel jacketing. At the same time, conducting experimental researches taking into account all the parameters which affect



the ultimate capacity of the load is not sensible, especially if the strengthening is under preloading. Accordingly, there is a need to develop a special FE model that could be used for simulating RC columns reinforced by steel jacketing and investigate the behaviors of each parameter under preloading.

While predicting RC columns' axial load capacity, fortified with steel jacketing, it is necessary to take into consideration the factors mentioned above and under preloading. In this research, the FE simulation model was built in 3D aiming at predicting the axial load capacity of steel jacketing-reinforced RC columns with and without preloading. On the basis of the findings derived from the parametric study, it is proposed to resort to prediction model to consider the effect of the preloading on the load capacity pertaining to steel jacketing-fortified RC columns. Moreover, experimental outcomes of tests conducted on RC columns as reflected in the literature review [3, 4] were gathered to use the same for verification of the precision of the analytical results obtained through the FE program (ANSYS-15) [17].

## 2. Existing Models

Many authors introduced design models for a similar problem. However, Campione [5], ACI Committee 318 [11], and Eurocode 4 [12] reported that the designed axial load capacity  $P_u$  of the steel jacketing-reinforced RC column is basically calculated from

$$P_u = P_c + P_s + P_{sj}, \quad (1)$$

where  $P_c$ ,  $P_s$ , and  $P_{sj}$  represent the contribution of concrete, steel reinforcement, and steel jacketing, respectively.

The models offered by ACI Committee 318 [11] and the majority of the models that already exist implement the equation given below for calculating the design axial load capacity of the RC column without strengthening:

$$\phi P_{n,max} = 0.80\phi [0.85f'_c(A_g - A_{st}) + (f_y A_{st})]. \quad (2)$$

For designing, the ACI code allows using the factors, such as  $\phi$ ,  $0.85f'_c$  and  $0.80$  to equivalent rectangular compressive stress distribution to replace the more exact concrete stress distribution and to make safety design. So if there is a need to predict failure axial load capacity, then the equation is formulated to

$$P_{u,f} = f'_c(A_c - A_{st}) + (f_y A_{st}). \quad (3)$$

As stated by Eurocode 4 [12], the ultimate load capacity of RC columns fortified with steel jacketing as a combined cross section is expressed by the following equation:

$$N_{pl,Rd} = 0.85A_c f'_{cd} + A_{st} f_{yd} + A_a f_{sd}, \quad (4)$$

where  $N_{pl,Rd}$  is the plastic resistance to compression;  $A_a$ ,  $A_c$ , and  $A_{st}$  are the cross-sectional domains of steel jacketing, concrete, and steel reinforcement, correspondingly; and  $f_{sd}$  and  $f_{cd}$  together with  $f_{yd}$  are their design values characteristic strengths. For concrete-filled sections, the coefficient  $0.85$  may be replaced by  $1.0$ , so equation (4) will be reduced to

$$P_{u,f} = N_{u,f} = A_c f'_{cd} + A_{st} f_{yd} + A_a f_{sd}. \quad (5)$$

However, several authors proposed models to acquire a precise equation for the axial load capacity of RC column reinforced by steel angles jacketing and horizontal steel plate strips.

Campione [5] stated an analytical expression for predicting the axial load capacity of reinforced RC columns with steel angles and strips jacketing. The final axial load capacity is given by

$$P_{u,Campione} = A_c f'_{cc} + A_s f_{sk} + n_a \cdot A_a \cdot f_y, \quad (6)$$

where  $f'_{cc}$  shows the compressive strength of confined concrete and  $n_a$  represents a dimensionless ratio of the axial force existing in the vertical steel angles jacketing.

## 3. ANSYS Finite Element Model Study

**3.1. Concrete Modeling and Properties.** While making an analysis, the commercial program of FE (ANSYS) was employed. For modeling the concrete, 65 solid elements were used ANSYS-15 [17]. Such an element consists of 8 nodes together with freedom of 3 degrees between every translations and node in the nodal  $x$ ,  $y$ , and  $z$  directions. Also, such an element can result in deforming of the plastic, breaking in 3 orthogonal directions with a simultaneous crushing. For modeling the concrete, to have a simulation of real concrete behavior, ANSYS needs linear and multilinear isotropic substance characteristics for centering, together with a few supplementary properties of the concrete substance.

The shear transfers coefficient  $\beta$ , relating to the state of the cracked face [17]. The range of the coefficient value is from  $0.0$  to  $1.0$ , with  $0.0$ , and  $0.0$  represents a smooth crack, and  $1.0$  suggests a rough crack [13, 14]. An open crack coefficient,  $\beta_t = 0.2$ , and the closed crack coefficient,  $\beta_c = 0.8$ , were taken in the study in hand [15]. The calculation about the modulus of elasticity of the concrete is possible to be carried out using the following equation:

$$E_c = 4700 \sqrt{f'_c}. \quad (7)$$

The calculation of uniaxial tensile stress can be made from the following equation:

$$f_r = 0.623 \sqrt{f'_c}. \quad (8)$$

Poisson's ratio of concrete of  $0.2$  was applied. The calculation of the compressive uniaxial stress-strain values for the concrete can be made using equation (9) [16]:

$$E_c = \frac{f_{el}}{\epsilon_{el}},$$

$$\epsilon_0 = \frac{2f'_c}{E_c}, \quad (9)$$

$$f = \frac{E_c \epsilon}{1 + (\epsilon/\epsilon_0)^2},$$

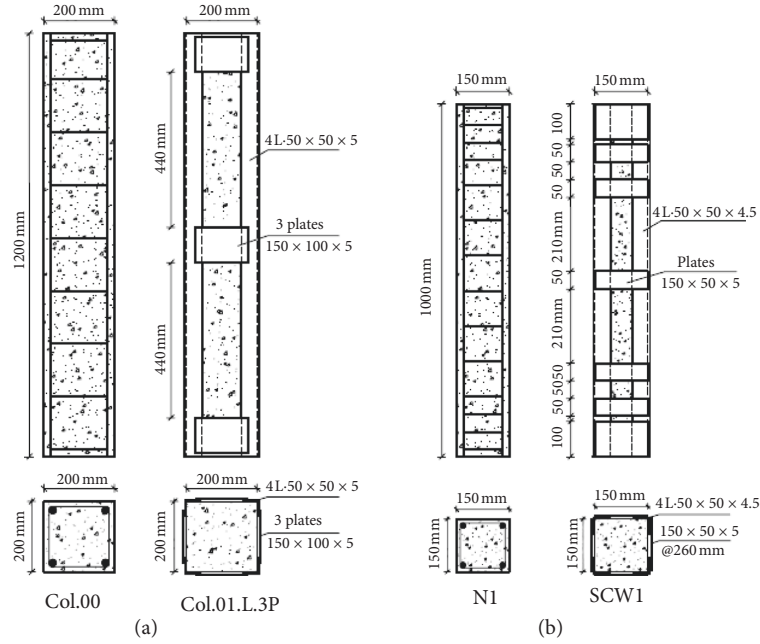


FIGURE 1: RC column geometrical details according to previously published work. (a) Belal et al. [3]. (b) Tarabia and Albakry [4].

where the modulus of elasticity is  $E_c$ , compressive strength is  $f'_c$ , and tensile stress is  $f_t$ , which are in MPa;  $f_{el}$  is the stress at the elastic strain ( $\epsilon_{el}$ ) in the elastic range  $f_{el} = 0.30f'_c$ ;  $\epsilon_0$  is the strain at the ultimate cylinder compressive strength,  $f'_c$ ; and  $f$  is the stress at any strain  $\epsilon$ .

**3.2. Strengthening of Steel, Steel Angles, and Steel Plates Modeling and Characteristics.** SOLID186 elements ANSYS-15 [17] were employed for modeling the steel strengthening, steel angles, and steel plates. SOLID186 is a 3D 20-node solid element of higher order, which displays how quadratic displacement behaves. The definition of this element is made as 20 nodes having 3 degrees of independence at each node. This element also assists plasticity, creep, hyperelasticity, large deflection, stiffening of stress, and larger capabilities of strain. Also, it carries a blend of the capability of the formulation to simulate the deformations of elastic-plastic materials almost incompressible and the hyperelastic materials that are completely compressible. SOLID186 is an identical structural solid that is very suitable for modeling asymmetrical meshes. The steel reinforcement, steel angles, and the plates of steel integrated into the FE models were expected to be materials of linear elasticity together with a modulus of elasticity concerning 210 GPa and Poisson's ratio of 0.3. The yielded stress is another thing that depends upon the use of the element.

The maximum size of the meshing elements was taken as 20 mm in length, 10 mm in height, and 10 mm in width. The contact between steel and concrete was modeled using a set of TARGE170 and CONTA174 contact elements [17], which function on the basis of Coulomb's friction model.

**3.3. Model Studies Pertaining to the Structure.** Seventeen RC columns (with variable cross sections and heights) exposed

to axial loading were considered in the present study. The columns were divided into two groups:

First group: consists of four columns according to previously published work [3, 4], as shown in Figure 1, which were examined to testify the accurateness of the FE model.

Second group: consists of thirteen columns under preloading with different percentages of preloading on the strengthened column, which were analyzed to propose a new model for predicting RC column's axial load capacity, reinforced with steel jacketing. Tables 1 and 2 demonstrate the key material and geometric characteristics of the test data.

## 4. Comparison of FE Modeling with the Experimental Results

To scrutinize the FE model for its validity and reliability, a comprehensive verification was done utilizing a chain of experimental data that exist in the background literature. The database taken into account comprises the outcomes of four experimental tests, together with the outcomes of tests on 2 columns without reinforced and 2 columns strengthened with steel angles jacketing. The key material, as well as geometrical characteristics about the experimental data, has been summarized in Tables 1 and 2.

Table 3 illustrates loads of failure including the findings of both experiments and analysis also showing the ratios between them. Figure 2 graphically compares the values derived through experiment and analysis. The table and the figure show the mean values of  $P_{Exp}/P_{FE}$  as 1.003, the conforming coefficient of variation as 3.16%, and the coefficient of correlation as 0.987. The given values illustrate that the FE model turns out to be an excellent match from a

TABLE 1: A brief account of RC columns assessed in the current study using FE modeling.

Group	Studies FE model based on	Column specimen	Concrete, $f_{cu}$ (MPa)	Column dimensions (mm)	Steel reinforcement		Stirrups	
					Long bars	$f_y$ (MPa)	Size	$f_y$ (MPa)
First	Belal et al. [3]	Col.00	34.0	200 × 200 × 1200	4Φ12 mm	360	φ8@150 mm	240
		Col.01.L.3P	34.0	200 × 200 × 1200	4Φ12 mm	360	φ8@150 mm	240
	Tarabia and Albakry [4]	N1	57.8	150 × 150 × 1000	4Φ10 mm	420	φ6@100 mm	240
		SCW1	57.8	150 × 150 × 1000	4Φ10 mm	420	φ6@100 mm	240
Second	New FE model	Control-300	34.0	300 × 300 × 4000	8Φ16 mm	360	φ8@150 mm	240
		Control-400	43.75	400 × 400 × 4000	12Φ16 mm	420	φ8@150 mm	240

TABLE 2: Summary of RC columns reinforced with steel jacketing in the present study.

Group	Studies FE model based on	Column specimen	Column dimensions (mm)	Strengthening configuration			Confinement stirrups		% preloading	
				Type	Size (mm)	$f_y$ (MPa)	Plates (mm)	Spacing (mm)		
First	Belal et al. [3]	Col.00	200 × 200 × 1200	Control	—	—	—	—	Without	
		Col.01.L.3P	200 × 200 × 1200	Angles	4L50 × 50 × 5	360	150 × 100 × 5	540	Without	
	Tarabia and Albakry [4]	N1	150 × 150 × 1000	Control	—	—	—	—	Without	
		SCW1	150 × 150 × 1000	Angles	4L50 × 50 × 4.5	415	150 × 50 × 5	260	Without	
Second	New FE model	Control-300	300 × 300 × 4000	Control	—	—	—	—	Without	
		Str.300.L50.P00	300 × 300 × 4000	Angles	4L50 × 50 × 10	360	280 × 100 × 5	500	Without	
		Str.300.L50.P22	300 × 300 × 4000	Angles	4L50 × 50 × 10	360	280 × 100 × 5	500	22	
		Str.300.L50.P43	300 × 300 × 4000	Angles	4L50 × 50 × 10	360	280 × 100 × 5	500	43	
		Str.300.L50.P85	300 × 300 × 4000	Angles	4L50 × 50 × 10	360	280 × 100 × 5	500	85	
		Str.300.L50.P94	300 × 300 × 4000	Angles	4L50 × 50 × 10	360	280 × 100 × 5	500	94	
		Str.300.L100.P00	300 × 300 × 4000	Angles	4L100 × 100 × 10	360	240 × 100 × 10	500	Without	
		Str.300.L100.P22	300 × 300 × 4000	Angles	4L100 × 100 × 10	360	240 × 100 × 10	500	22	
		Str.300.L100.P43	300 × 300 × 4000	Angles	4L100 × 100 × 10	360	240 × 100 × 10	500	43	
		Str.300.L100.P85	300 × 300 × 4000	Angles	4L100 × 100 × 10	360	240 × 100 × 10	500	85	
		Str.300.L100.P94	300 × 300 × 4000	Angles	4L100 × 100 × 10	360	240 × 100 × 10	500	94	
		Control-400	400 × 400 × 4000	Control	—	—	—	—	—	Without
		Str.400.L100.P37	400 × 400 × 4000	Angles	4L100 × 100 × 10	420	340 × 100 × 10	500	37	

statistical perspective, and it can be observed for all RC columns with or without strengthening the configurations dealt with while making an analysis.

Figures 3 and 4 bear the curves showing how the load is displaced for specimens used on the experiments and the resultant FE modeling. One comparing the curves of load displacement attained from findings of experiments with the ones attained from the FE models for RC columns with or without strengthening can note an excellent match between them.

The way how FE models deal with all the specimens together with deformed shapes, failure loads, and failure modes was recorded. Figures 5 and 6 illustrate the deformations, failure modes, and locations for experimental specimens and the corresponding FE modeling. When comparing the deformations, failure modes, and locations acquired from the experimental outcomes with the ones

acquired from the FE models for RC columns with or without strengthening, it can also be observed as an excellent match.

## 5. Predicting the Axial Load Capacity under Preloading of RC Columns Founded on Simulation of FE

For assessment of the influence of the parameters on a load of axial capacity, a parametric study was carried out. These parameters incorporated the column dimensions, the concrete strength, the cross section of the zone and yield stress of the steel fortification, the cross section of the zone and the stress yielded by the steel jacketing, and the percentage of preloading. Meanwhile, the typical model from Eurocode 4 [12] was utilized for comparison.

TABLE 3: Comparison of failure load and ratios of  $P_{Exp}/P_{FE}$  for experimental and FE results.

Studies FE model based on	Column specimen	Experimental failure load (kN)	FE failure load (kN)	$P_{Exp}/P_{FE}$
Belal et al. [3]	Col.00	1255	1230	1.020
	Col.01.L3P	1821	1900	0.958
Tarabia and Albakry [4]	N1	1475	1487.5	0.992
	SCW1	2310	2213	1.043

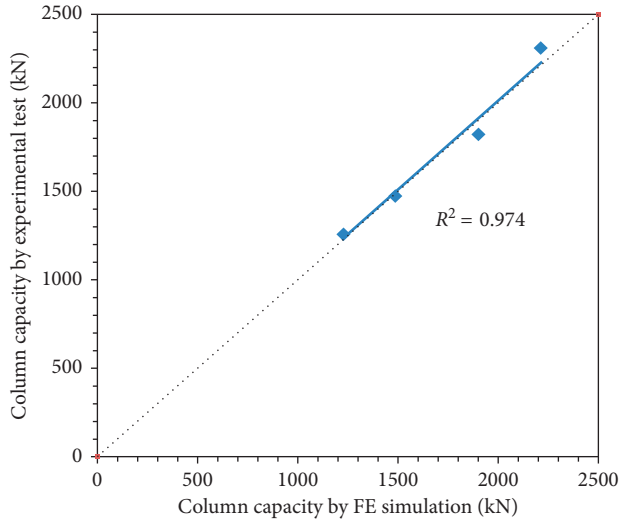


FIGURE 2: A comparison of the experimental and FE analysis values for axial load capacity.

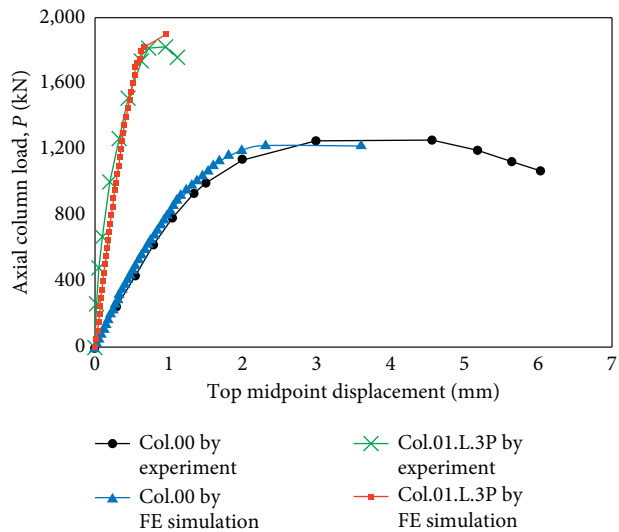


FIGURE 3: Curves showing displacement of load gained from both experimental outcomes Belal et al. [3] and FE results.

5.1. Behavior of Axial Load Displacement. Figures 7 and 8 illustrate how the axial load and column axial displacement are related to each other. Generally, the final load increases when steel jacketing strengthening was used. When the RC column is strengthened under preloading, the ultimate load decreases when the preloading increases.

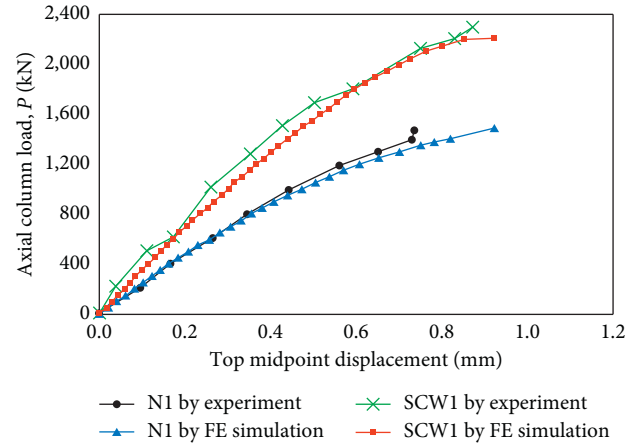


FIGURE 4: Curves showing displacement of load gained from both experimental Tarabia and Albakry [4] and FE outcomes.

5.2. Predicting the RC Columns' Axial Load Capacity Based on FE Simulation. By means of the parameters considered in the present research, it is possible to calculate the axial load capacity of RC columns through the addition of the normal force from concrete and the normal force from steel reinforcement, independently for RC column without strengthening. Furthermore, by making an addition of steel jacketing contributions right to the normal force of the RC column, the procedures ACI Committee 318 [11] and Eurocode 4 [12] come to an excellent match. As a result, the axial load capacity of a reinforced RC column is articulated as the total of the 3 normal constituents in consonance with the internationally accepted procedures as incorporated in equation (2). Table 4 demonstrates the RC column parameters appraised in the current study and the eventual axial loads, derived from simulating and analyzing the FE. The prediction regarding the axial load capacity by the Eurocode 4 [12] design model proposed can be seen in Table 4.

For the evaluation of the FE results' reliability, the findings attained from the design model suggested by Eurocode 4 [12] is compared with the results obtained from the FE simulation, as illustrated in Figure 9. An identical prediction between the Eurocode models and the FE simulations for RC columns can be seen without preloading. In this figure, the mean value of  $P_{u,Eurocode}/P_{u,FE}$  is 0.998, the corresponding coefficient of variation is 2.01%, and the coefficient of correlation is 0.99. The aforementioned values reveal that the FE model is an excellent match, and it can be observed for all RC columns without preloading with the prediction values from the Eurocode 4 [12] model. Otherwise, for RC columns with preloading, the mean value of  $P_{u,Eurocode}/P_{u,FE}$  is 1.199, the



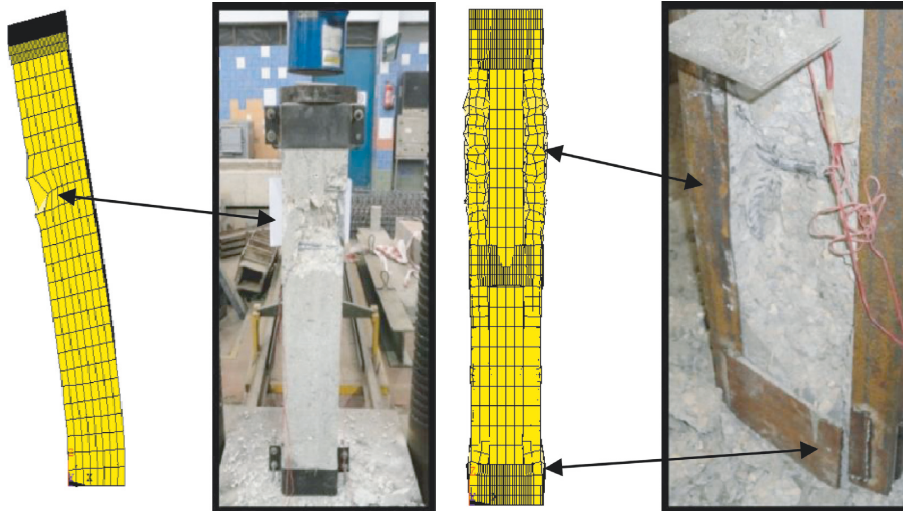


FIGURE 5: Deformations, failure modes, and locations obtained from both experimental Belal et al. [3] and FE results.

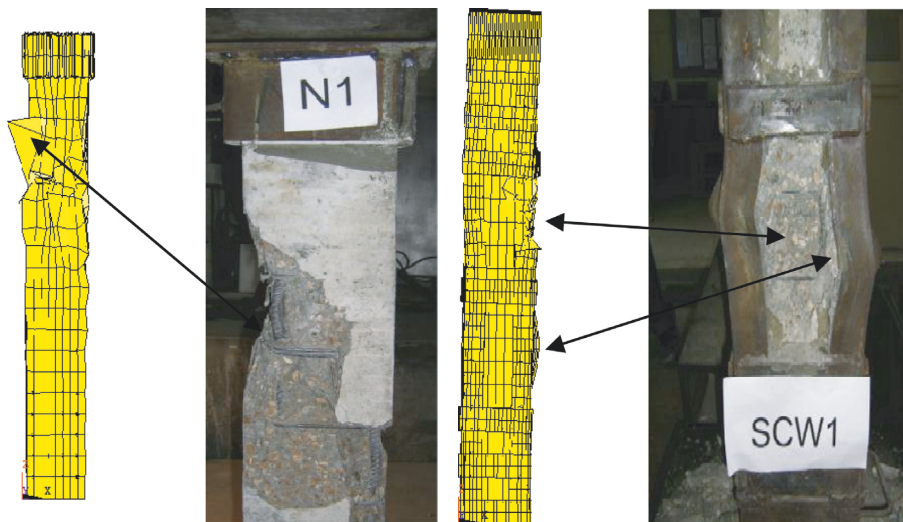


FIGURE 6: Deformations, failure modes, and locations obtained from both experimental Tarabia and Albakry [4] and FE results.

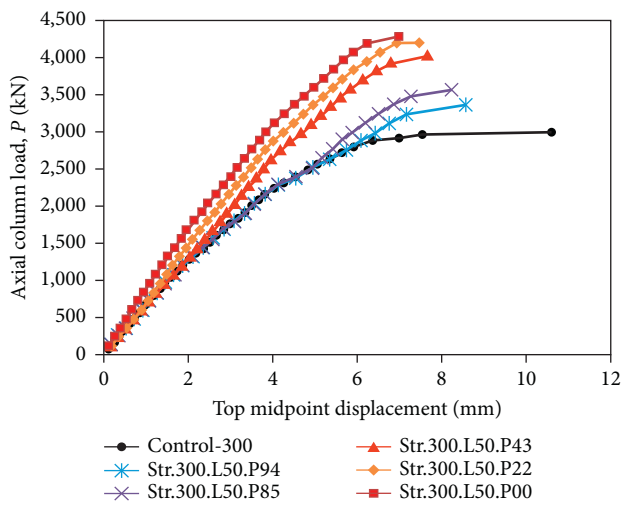


FIGURE 7: The curves relating to load displacement obtained from FE simulation for columns strengthened by 4L-50 × 50 × 10 with different percentages of preloading.

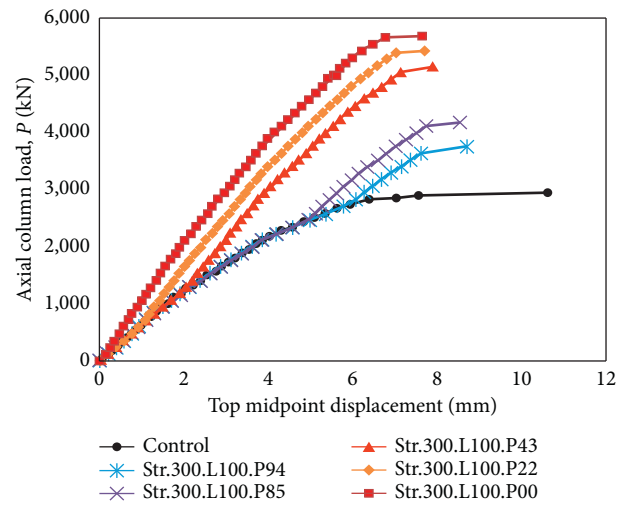


FIGURE 8: The curves relating to load displacement obtained from FE simulation for columns strengthened by 4L-100 × 100 × 10 with different percentages of preloading.

TABLE 4: Summary of RC columns strengthened with steel jacketing in the present study.

Column specimen	% preloading $P_{pre}/P_{u,control}$	$P_{u,f}$ Eurocode (kN)	FE failure load (kN)	Increase in failure load (kN)	Area of steel jacketing, $A_{sj}$ (mm <sup>2</sup> )	Steel jacketing stress, $f_s = (P_{increase}/A_{sj})$ (MPa)	$f_y$ (MPa)	$f_s/f_y$
Col.00	0.0	1250.7	1230	0.0	0.0	0.0	0.0	0.0
Col.01.L.3P	0.0	1934.7	1900	670	1900	353	360	0.981
N1	0.0	1432.4	1487.5	0.0	0.0	0.0	0.0	0.0
SCW1	0.0	2145.8	2213	725.5	1719	422	415	1.016
Control-300	0.0	3026.9	3000	0.0	0.0	0.0	360	0.0
Str.300.L50.P00	0.0	4322.9	4290	1290	3600	359	360	0.997
Str.300.L50.P22	22	4322.9	4200	1200	3600	334	360	0.928
Str.300.L50.P43	43	4322.9	4050	1050	3600	292	360	0.811
Str.300.L50.P85	85	4322.9	3570	570	3600	159	360	0.442
Str.300.L50.P94	94	4322.9	3360	360	3600	100	360	0.278
Str.300.L100.P00	0.0	5762.9	5820	2820	7600	371	360	1.030
Str.300.L100.P22	22	5762.9	5550	2550	7600	336	360	0.933
Str.300.L100.P43	43	5762.9	5250	2250	7600	296	360	0.822
Str.300.L100.P85	85	5762.9	4260	1260	7600	166	360	0.461
Str.300.L100.P94	94	5762.9	3810	810	7600	107	360	0.297
Control-400	0.0	6613.0	6545	0	0.0	0.0	0.0	0.0
Str.400.L100.P37	37	9805.0	9185	2640	7600	347	420	0.826

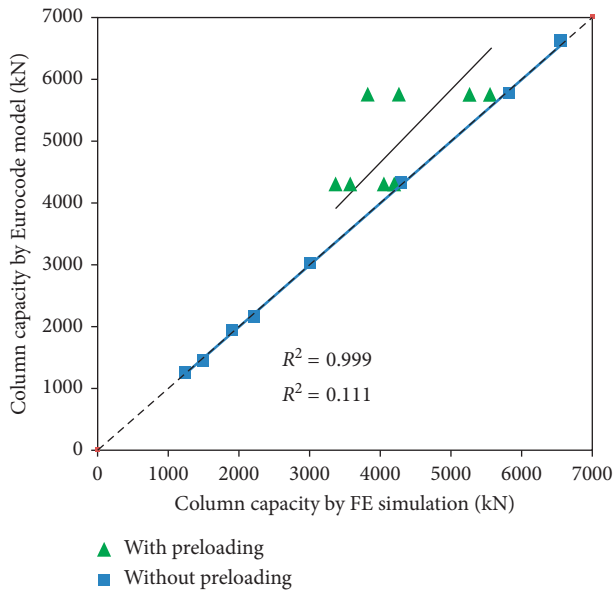


FIGURE 9: Comparison between the Eurocode model [12] and FE simulation for axial load capacity.

conforming coefficient representing variation is 13.58%, and the coefficient of correlation is 0.33; these values show that the prediction values from the Eurocode 4 [12] model are too far from the values obtained from FE simulation. So the Eurocode model needs to be modified to take the preloading when strengthening into consideration.

On the basis of FE simulating 17 RC columns, a clarification was made earlier regarding the rise in the axial load capacity that registered variation with the fluctuation of percentage in preloading; hence, the relationship between the rise in the axial load capacity and percentage of preloading is framed in equation (10), where the equation is a polynomial of the relationship between the ratios of the percentage of preloading with ultimate failure load of the

control RC column ( $P_{p,L}/P_{u,f}$ ) and percentage of steel jacketing stress obtained from the FE simulation with yield stress ( $f_{sj}/f_{yj}$ ), as shown in Figure 10:

$$\frac{P_{p,L}}{P_{u,f}} = -1.167 \left( \frac{f_{sj}}{f_{yj}} \right)^2 + 0.184 \left( \frac{f_{sj}}{f_{yj}} \right) + 0.992. \quad (10)$$

Equation (5), which is employed in the majority of the prevailing models for predicting the axial load capacity for RC column without strengthening, and the proposed new model in equation (10) predict the steel jacketing stress under preloading. The new model that has been recently proposed for predicting the axial load capacity and can be applied to RC columns extrinsically reinforced with steel jacketing strengthening is formulated in the following equation:

$$P_{u,f} = f'_c A_c + f_{sy} A_{st} + f_{sj} A_{sj}. \quad (11)$$

## 6. Conclusions

The introduction of the FE simulation model has been made for predicting the contribution of steel jacketing to the RC columns' axial load capacity. There are parametric studies conducted for assessing the influences of several parameters on the capacity of axial load and failure modes relating to RC columns. The investigative findings derived from the FE model were subjected to a comparison with outcomes attained from previously published work cited in the literature, involving a different structure, concerning test geometries. There is a proposal for a new model which takes into account the investigated parameters. On the basis of this research, the conclusions drawn are given below:

- (1) In comparison with the findings of the experiments, the FE model is considered to be more accurate in making a prediction about the mode of failure and determining the axial load capacity. The mean value

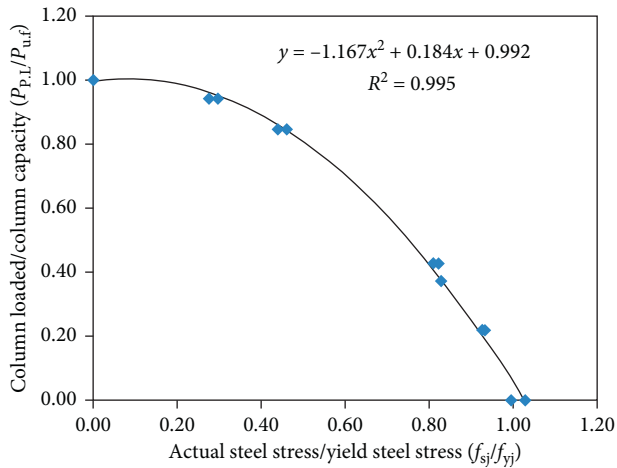


FIGURE 10: The relation between percentage of preloading columns and the corresponding percentage of steel jacketing stress obtained from the FE simulation.

of  $P_{Exp}/P_{FE}$  is 1.003 for columns that strengthened by steel jacketing or without strengthening. The corresponding coefficient of variation is 3.16%, and the coefficient of correlation is 0.987.

- (2) Evaluation with the results obtained from the design model in Eurocode 4 [12] is compared with the results obtained from the FE simulation; there is an excellent match prediction between the Eurocode models and the FE simulations for RC columns without preloading.
- (3) The new model equation (10) can predict steel jacketing stress and the RC columns' axial load capacity strengthened by means of steel jacketing under preloading.

## Data Availability

The data used to support the findings of this study are available from the corresponding author upon request.

## Conflicts of Interest

The authors declare that they have no conflicts of interest.

## Acknowledgments

The author would like to thank the Deanship of Scientific Research at Majmaah University for supporting this work under Project no. 1440-48.

## References

- [1] M. Vild and M. Bajer, "Strengthening under load: the effect of preload magnitudes," *Procedia Engineering*, vol. 161, pp. 343–348, 2016.
- [2] M. Vild and M. Bajer, "Strengthening under load: numerical study of flexural buckling of columns," *Procedia Engineering*, vol. 190, pp. 118–125, 2017.
- [3] M. F. Belal, H. M. Mohamed, and S. A. Morad, "Behavior of reinforced concrete columns strengthened by steel jacket,"

*Housing and Building National Research Center (HBRC) Journal*, vol. 11, no. 2, pp. 201–212, 2015.

- [4] A. M. Tarabia and H. F. Albakry, "Strengthening of RC columns by steel angles and strips," *Alexandria Engineering Journal*, vol. 53, no. 3, pp. 615–626, 2014.
- [5] G. Campione, "Load carrying capacity of RC compressed columns strengthened with steel angles and strips," *Engineering Structures*, vol. 40, pp. 457–465, 2012.
- [6] J. M. Adam, S. Ivorra, F. J. Pallarés, E. Giménez, and P. A. Calderón, "Axially loaded RC columns strengthened by steel caging. finite element modeling," *Construction and Building Materials*, vol. 23, no. 6, pp. 2265–2276, 2009.
- [7] E. Choi, Y.-S. Chung, J. Park, and B.-S. Cho, "Behavior of reinforced concrete columns confined by new steel-jacketing method," *ACI Structural Journal*, vol. 107, no. 6, pp. 654–662, 2010.
- [8] E. Giménez, J. M. Adam, S. Ivorra, and P. A. Calderón, "Influence of strips configuration on the behaviour of axially loaded RC columns strengthened by steel angles and strips," *Materials and Design*, vol. 30, no. 11, pp. 4103–4111, 2009.
- [9] E. S. Khalifa and S. H. Al-Tersawy, "Experimental and analytical behavior of strengthened reinforced concrete columns with steel angles and strips," *International Journal of Advanced Structural Engineering*, vol. 6, no. 2, pp. 1–14, 2014.
- [10] J. M. Adam, S. Ivorra, E. Gimenez et al., "Behaviour of axially loaded RC columns strengthened by steel angles and strips," *Steel and Composite Structures*, vol. 7, no. 5, pp. 405–419, 2007.
- [11] ACI Committee 318, *Building Code Requirement for Structural Concrete (ACI 318-14) and Commentary*, American Concrete Institute, Farmington Hills, MI, USA, 2014.
- [12] Eurocode 4–ENV 1994-1-1, *Design of Composite Steel and Concrete Structures, Part 1–1*, General Rules and Rules for Buildings, 2004, <https://www.phd.eng.br/wp-content/uploads/2015/12/en.1994.1.1.2004.pdf>.
- [13] L. Terec, T. Bugnariu, and M. Păstrav, "Non-linear analysis of reinforced concrete frames strengthened with in filled walls," *Romanian Journal of Materials*, vol. 40, no. 3, pp. 214–221, 2010.
- [14] A. K. H. Kwan, H. Dai, and Y. K. Cheung, "Non-linear seismic response of reinforced concrete slit shear walls," *Journal of Sound and Vibration*, vol. 226, no. 4, pp. 701–718, 1999.
- [15] A. M. Sayed, X. Wang, and Z. Wu, "Finite element modeling of the shear capacity of RC beams strengthened with FRP sheets by considering different failure modes," *Construction and Building Materials*, vol. 59, pp. 169–179, 2014.
- [16] D. Kachlakev, T. Miller, and S. Yim, "Finite element modeling of reinforced concrete structures strengthened with FRP laminates," in *Research Group Final Report SPR 316*, Oregon Department of Transportation, Washington, DC, USA, 2001.
- [17] ANSYS User's Manual Version (15), *Swanson Analysis Systems*, ANSYS, Canonsburg, PA, USA, 2015.



## Research Article

# Numerical Study on Diffusion of Chloride and Induced Rebar Corrosion by Two-Dimensional Multiscale Approach

Xi Tu <sup>1,2</sup>, Jin Di, <sup>1,2</sup> Cunjun Pang, <sup>1,2</sup> and Xiaoqing Xu <sup>1,2</sup>

<sup>1</sup>Key Laboratory of New Technology for Construction of Cities in Mountain Area (Chongqing University), Ministry of Education, Chongqing, China

<sup>2</sup>College of Civil Engineering, Chongqing University, Chongqing, China

Correspondence should be addressed to Xi Tu; [tuxi@cqu.edu.cn](mailto:tuxi@cqu.edu.cn)

Received 15 November 2018; Accepted 12 December 2018; Published 31 December 2018

Guest Editor: Qing-feng Liu

Copyright © 2018 Xi Tu et al. This is an open access article distributed under the Creative Commons Attribution License, which permits unrestricted use, distribution, and reproduction in any medium, provided the original work is properly cited.

Modeling approach for mesoscopic model of concrete depicting mass transportation and physicochemical reaction is important since there is growing demand for accuracy and computational efficiency of numerical simulation. Mesoscopic numerical simulation considering binder, aggregate, and interfacial transition zone (ITZ) generally produces huge number of DOFs, which is inapplicable for full structure. In this paper, a two-dimensional multiscale approach describing three-phase structure of concrete was discussed numerically. An effective approach generating random aggregate in polygon based on checking centroid distance and intersection of line segment was introduced. Moreover, ITZ elements were built by parallel expanding the edge of aggregates on inner side. By combining mesoscopic model including full-graded aggregate and macroscopic model, cases related to diffusivity and width of ITZ, volume fraction, and grade of aggregate were studied regarding the consideration of multiscale compensation. Result clearly showed that larger analysis model in multiscale model expanded the diffusion space of chloride ion and decreased chloride content in front of rebar. Finally, this paper addressed some noteworthy conclusions about the chloride distribution and rebar corrosion regarding the configuration of rebar diameter, concrete cover, and exposure period.

## 1. Introduction

Corrosion of rebar induced by chloride ion could significantly deteriorate the serviceability of concrete structures [1]. The protective film of rebar was depassivated by chloride ion penetrated from surface of concrete and thus corrosion of rebar initiates once the chloride content on surface of rebar reaches a certain thresholding value, defined as critical chloride content. Afterwards, corrosion of rebar keeps propagating and induces further cracking and spalling due to expansion of rust. Therefore, it is important to accurately assess the diffusion process of chloride ion within concrete, which is meaningful for further evaluation of durability of reinforced concrete structures.

In the view of mesoscopic numerical simulation, concrete was recognized as the heterogeneous composite of three phases, including cement paste, aggregate, and interfacial transition zone (ITZ) [2]. ITZ was identified as a fine cement paste zone enclosing aggregate and rebar, providing higher

water-to-cement ratio, higher porosity, and lower cement content compared with normal bulk cement paste regions. Thus ITZ was generally considered as an individual phase [3–5]. Though the porosity of ITZ decreases with increase of distance from aggregate surface [6], ITZ was simplified as a homogenous thin layer in most studies. Significant influence on the overall behavior of concrete attributes to ITZ due to its fraction of the total paste volume, such as diffusivity and strength [4, 6–8].

In the view of mesoscopic numerical simulation, due to large amount of nodes and elements, an optimized approach was that three-phase composite of concrete was simplified into two-phase composite including cement paste and homogenized equivalent aggregate [4, 7, 9–13]. Diffusivity of ITZ was transferred by means of deriving the analytical solution of general effective chloride diffusivity, which means modeling of ITZ is unnecessary.

Generally, modeling and analysis for cement-based material were categorized in microscopic scale, mesoscopic scale,

and macroscopic scale [14, 15]. Recently a number of theory research and modeling efforts have been devoted to studying multiscale modeling. Multiscale modeling was usually defined as the integrated numerical process of transferring mechanical and chemical response between lower scale and higher scale [16, 17]. A significant advantage of multiscale modeling is optimizing computing loading and enhancing the precision. According to available literature, researchers generally focused on the transferring process of material response between scales.

As the major purpose of multiscale modeling to reduce calculation loading, heterogeneous model was always modeled for transferring damage and mass transportation of critical regions from the macroscale to the mesoscale which provided coupling of subdomains [18]. Balance of accuracy and efficiency is the major consideration of multiscale modeling for numerical simulation. By means of macroscopic model substituting for a part of mesoscopic model, multiscale modeling is able to provide relatively smaller size of mesoscopic model and generate the same filling rate of aggregate and less amount of aggregate, which is no doubt beneficial for raising success rate of meshing [19].

For mesoscopic structure of concrete, both of size and shape of aggregates are generated as given design. Regarding two-dimensional space, general process was divided into two steps, including modeling of geometric model and meshing. Angular aggregate was generated based on inscribed convex polygon within elongated ellipse [20]. Wang et al. proposed a procedure for generating random aggregate structures for angular aggregates by means of Monte Carlo sampling, which was compatible for concave polygon [21]. An inevitable algorithm was intersection check of convex polygons, which was achieved by detecting space independence of two polygons [22, 23]. In terms of meshing, mortar plus smaller aggregates embedding coarse aggregate was discretized into finite elements by free meshing [20, 24] or uniform background grid [25–27].

Another major factor for durability of reinforced concrete structures is corrosion of steel rebar. Researchers devoted efforts on laboratorial research by means of natural experiments [28–32] and accelerated experiments [33–38] about the process of chloride diffusion and corrosion. On the other hand, some types of simplified approximate law for corrosion were introduced. Biondini introduced a reasonable linear damage model for corrosion of rebar under aggressive agent, which evaluates corrosion rate according to the real-time chloride content surrounding rebar [39–42]. Despite the complex principle of corrosion, based on the natural damage mode of corrosion, this linear damage model is able to provide acceptable description of damage process.

This paper discussed two important aspects regarding multiscale modeling for numerical simulation of chloride ion diffusing within concrete. Firstly, a comprehensive modeling approach for concrete considering both multiscale modeling including interfacial transition layer (ITL) and three-phase mesoscale structure including ITZ. Secondly, by means of the multiscale numerical simulation tool, the influence of ITZ on diffusion of chloride ion within concrete in mesoscale was studied in detail, where ITZ was modeled as

an individual phase in FE model for chloride diffusion in concrete. Besides, the corrosion of rebar in straight edge of concrete induced by diffusion of chloride ion was also calculated to study the time evolution of corrosion process.

## 2. Multiscale Modeling and Discussion

*2.1. Multiscale Modeling Theory.* In mesoscopic numerical simulation for chloride diffusion, usually 100~200 mm size of specimen in square or rectangle was considered. Within this typical size of analysis space, enough number of aggregates with various sizes were included for in-depth study. Within limited analysis space, chloride ion would be able to penetrate and saturate the whole space within the assessing period, indicating the whole space was inadequate for further simulation. However, it would be impossible to increase the size of analysis space due to two reasons. First, several times of original size of analysis space will generate much more nodes and elements, especially for three-dimensional problem. Second, to control computing loading, changing the grading curve and ignoring fine aggregate will cause inaccuracy of numerical simulation.

In this paper, a scheme of multiscale modeling was introduced in terms of balancing amount of nodes and elements and calculation accuracy (Figure 1). In the view of multiscale modeling, based on original mesoscopic model including multiphase components which was defined as core part, a macroscopic compensation model, which was defined as compensation part, was modeled. The aim of introducing compensation part was creating addition space to absorb the chloride within core part and adjusting the distribution of chloride content within core part, which means redistribution of chloride in larger space.

Due to different definition of nodal chloride content and diffusion coefficient in mesoscopic model and macroscopic model, the two types of models cannot be directly combined and analyzed simultaneously. In this paper, interfacial transition layer (ITL) was introduced to connect both models at the interface which consists of a group of nodes and elements, shown in Figure 1. ITL was designed as a banded shape transition zone allowing chloride ion diffusing from core part into compensation part. Within each time step, core part and compensation part were analyzed sequentially and the chloride content at interface of the two parts was transferred based on the function of ITL.

It is worth noting that the most important precondition is the mechanism of ITL for transporting the chloride ion, which generates equivalent diffusion and distribution of chloride within the model on the same scale. ITL could be composed by a row of common nodes occupied by both mesoscopic model and macroscopic model, as well as an amount of elements with certain thickness stuck by both models.

The process of transferring chloride ion within ITL in one-dimension was illustrated in Figure 2. For initial state, analysis space of three phases including core part, compensation part, and ITL was modeled, respectively. Boundary condition was set at surface of concrete, which was the top of core part shown in Figure 2.

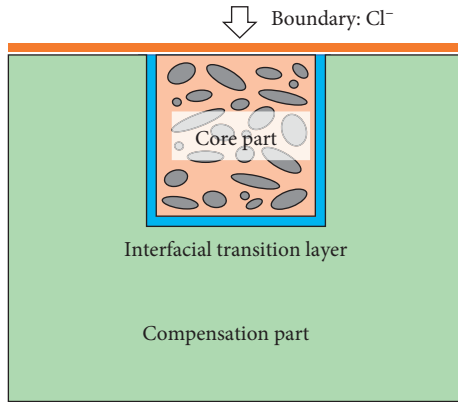


FIGURE 1: Two-dimensional multiscale model with core part and compensation part for simulating chloride diffusion within concrete.

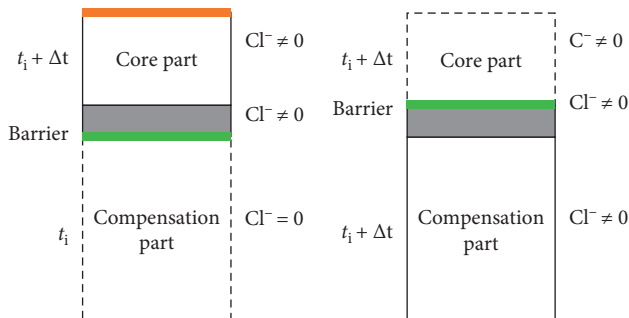


FIGURE 2: The two stages of chloride diffusion at the interfacial transition layer connecting macroscopic and mesoscopic model. (a) First stage. (b) Second stage.

This mixed model behaved in sequential multiscale process. For the mixed case that core part is in mesoscale and compensation part in macroscale, equivalent chloride content in ITL will be calculated and transferred. Definitions of chloride content in both parts were different. Chloride content in macroscopic model was measured in concrete, and the value in mesoscopic model was measured in cement. Therefore, a necessary procedure was included that the value of chloride content in ITL should be calculated for each stage. Simulation of chloride diffusion within mixed model was divided into two stages of diffusion and two steps of conversion.

- (1) The first stage of diffusion: core part and ITL were connected as common interface while ITL and compensation part were disconnected. With one time step, chloride ion penetrated into core part from boundary condition. During current stage, diffusion of chloride ion restrained within core part and ITL. The chloride content of core part and ITL rose up from previous content while compensation part kept unchanged.

Find out all of the elements with the centroid located within the elements from compensation model.

Calculate the weighted mean content of all these elements in core model. This content is the represented content for the element in compensation model.

- (2) Conversion from mesoscale to macroscale within ITL: the simulated result in region in core part covered by ITL was converted from mesoscale to macroscale within this step. For the instance of center bottom of concrete boundary, compensation part was modeled as simply one-dimensional model. Within core part, elements with their centroid included in interfacial transfer layer were identified (the region enclosed by red dashed line in Figure 3). Weighted mean value of chloride content of these involved elements was calculated for the nodal value of ITL in macroscale.
- (3) The second stage of diffusion: a new barrier was inserted at common border of core part and ITL which was equal to cut down the connection of these parts. The existing barrier at common border of compensation part and ITL was removed. During this stage, chloride redistributes within the region including ITL and compensation part.
- (4) Conversion from macroscale to mesoscale within ITL: as the inverse process of the 2nd step, the nodal content of mesoscopic core part was interpolated from macroscopic compensation part in the form of regular rectangle element. As was illustrated in Figure 4, the outer rectangle represents the uniform quadrilateral model in compensation part and the target node denotes the node included within core part. Four nodes of the quadrilateral were numbered in counterclockwise.

*2.2. Analytical Study for Finite Space with Exposed and Time-Dependent Boundary.* In following section, this paper discussed about the feasibility of multiscale model in analytical approach. Due to the sectional design of rebar in concrete member, some research studies on chloride diffusion were transformed within two-dimensional space equivalently. For the case on center of bottom of concrete section, concrete and outer atmosphere were divided into two infinite half-space into which the boundary plane divides the three-dimensional space. Regarding numerical simulation, for the same configuration of boundary condition and diffusivity of concrete, all points in concrete at the same depth from the boundary behave in the same characteristics of diffusion. In simplification, the chloride diffusion in three-dimensional and two-dimensional space was equivalent to one-dimensional one. Therefore, the problem was simplified to one-dimensional macroscopic model, and the analytical solution for finite space with both exposed and sealing boundary was discussed. Usually diffusion of chloride within solution was expressed by linear Fick's second law:

$$\frac{\partial C}{\partial t} = D \cdot \nabla^2 C, \quad (1)$$

where  $D$  is the diffusion coefficient of concrete.  $C$  denotes the chloride content. Considering the boundary condition of  $C(0, t) = C_s$  and  $C(\infty, t) = C_0$ . As was widely known, according to Laplace transform, the analytical solution of above partially derivative equation was

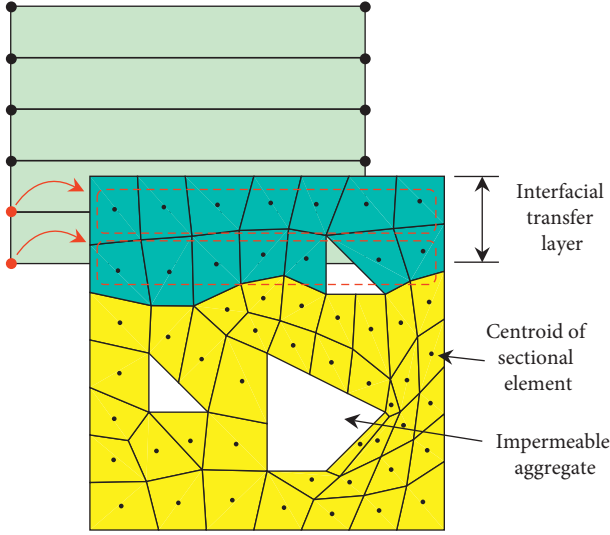


FIGURE 3: First step of conversion: calculation of nodal chloride content of compensation part from involved elements in core part (red dashed: coverage of nodes in compensation part; blue: involved elements in core part; yellow: uninvolved elements).

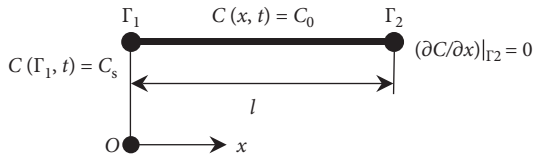


FIGURE 4: Analysis model for analytical deduction.

$$C(x, t) = C_0 + (C_s - C_0) \left[ 1 - \operatorname{erf} \left( \frac{x}{2\sqrt{Dt}} \right) \right], \quad (2)$$

where erf is Gauss error function. The limitation of the above solution is the premise of infinite space for boundary condition, which is suitable for concrete members with large thickness compared with thickness of concrete cover, but inaccurate for typical beams and slabs. For finite space, three-dimensional analytical solution by means of separation of variables was discussed and deduced by Li et al. [43]. For one-dimensional space, assuming the total length of diffusion space is  $l$ .  $x$  axis is the longitudinal direction of the one-dimensional model. Initial condition for diffusion space,  $C(x, 0) = C_0$  and boundary condition, exposed boundary  $C(\Gamma_1, t) = C_s$ , and sealing boundary  $\partial C/\partial x|_{\Gamma_2} = 0$  were all considered. The schematic illustration is shown in Figure 4.

The simplified function of chloride content including the variables of time and depth in one-dimensional space according to Li's solution was expressed as follows:

$$C = C_s + (C_0 - C_s) \sum_{n=1}^{\infty} \frac{4}{(2n-1)\pi} \sin\left(\frac{2n-1}{2l}\pi x\right) e^{-D((2n-1)/2l)\pi^2 t}. \quad (3)$$

If zero chloride content for initial condition,  $C_0 = 0$ , was considered, equation (3) was simplified as given below:

$$C = C_s \left[ 1 - \sum_{n=1}^{\infty} \frac{4}{(2n-1)\pi} \sin\left(\frac{2n-1}{2l}\pi x\right) e^{-D((2n-1)/2l)\pi^2 t} \right]. \quad (4)$$

The aim of following section was to deduce the expression of analytical solution of chloride content with both exposed boundary and time-dependent boundary according to Li's deduction process and prove that the development in core model with predefined time-dependent boundary condition is same as the part in full model. For the consideration of compensation for chloride diffusion, a part of the full model was extracted and called as *Core Model*. The schematic illustration of core model was shown in Figure 5. The length of core model was  $l_1$  while assuming the length of full model was  $l_2$  ( $l_2 > l_1$ ).

Being different with the precondition of Li's solution [43], the boundary condition  $\Gamma_2$  of core model was modified into the function of time-dependent boundary  $\Gamma_2'$  strictly defined by equation (4) set at  $l_1$ , expressed in equation (5). The other parameters and definition were the same as before. For simplification, zero chloride content for initial condition,  $C_0 = 0$ , was considered.

$$\begin{aligned} C(t)|_{\Gamma_2} &= C_s \left[ 1 - \sum_{n=1}^{\infty} \frac{4}{(2n-1)\pi} \sin\left(\frac{2n-1}{2l_2}\pi l_1\right) e^{-D((2n-1)/2l_2)\pi^2 t} \right]. \end{aligned} \quad (5)$$

Considering a temporary variable  $V$ ,

$$V = C - C_s. \quad (6)$$

Apart from initial condition and boundary condition, the time-dependent boundary  $\Gamma_2'$  was expressed as

$$V|_{x=l_1} = -C_s \sum_{n=1}^{\infty} \frac{4}{(2n-1)\pi} \sin\left(\frac{2n-1}{2l_2}\pi l_1\right) e^{-D((2n-1)/2l_2)\pi^2 t}. \quad (7)$$

By means of separation of variables,  $V$  was expressed as

$$V(x, t) = X(x) \cdot T(t). \quad (8)$$

By introducing boundary condition of exposed surface  $\Gamma_1$ , the general solution of  $X$  was simplified as

$$X(x) = B \sin(\alpha x). \quad (9)$$

For time-dependent boundary  $\Gamma_2'$ , by combining equations (7) and (9), we obtained the expression of  $\alpha$ :

$$\alpha_n = \frac{2n-1}{2l_2} \pi, \quad (n = 1, 2, \dots). \quad (10)$$

Thus, particular solution of  $X$  was

$$X_n(x) = k_n \sin\left(\frac{2n-1}{2l_2}\pi x\right). \quad (11)$$

The particular solution of  $T$  was solved as

$$T_n = -d_n e^{-D\alpha_n^2 t}. \quad (12)$$



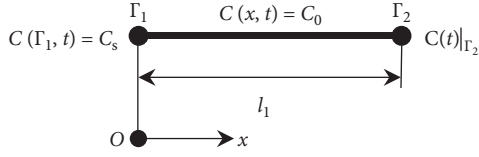


FIGURE 5: Illustration of core model for diffusion with compensation.

Thus, general solution of  $V$  was

$$V_n = e_n \sin\left(\frac{2n-1}{2l_2} \pi x\right) e^{-D\alpha_n^2 t}. \quad (13)$$

where  $e_n$  was the  $n$ th order of unknown expression and  $e_n = k_n \cdot d_n$ . Considering initial condition ( $t = 0$ ), we obtained the following from equation (13):

$$\sum_{n=1}^{\infty} e_n \sin\left(\frac{2n-1}{2l_2} \pi x\right) = -C_s. \quad (14)$$

Due to orthogonality of the following function series,

$$\int_0^l \sin(\alpha_m x) \sin(\alpha_n x) dx = \begin{cases} 0, & m \neq n, \\ l/2, & m = n, \end{cases} \quad (15)$$

Combining equations (14) and (15), we obtained:

$$e_n = -\frac{4C_s}{(2n-1)\pi}. \quad (16)$$

By combining equations (6), (13), and (16), finally we obtained:

$$C = C_s \left[ 1 - \sum_{n=1}^{\infty} \frac{4}{(2n-1)\pi} \sin\left(\frac{2n-1}{2l_2} \pi x\right) e^{-D\left(\frac{(2n-1)\pi}{2l_2}\right)^2 t} \right], \quad (x \in [0, l_1]). \quad (17)$$

Therefore, even considering the time-dependent boundary, the development of diffusion within core model was exactly the same as the original model, which proved the feasibility of compensation for chloride diffusion.

### 3. Mesoscopic Modeling Approach

**3.1. Generation of Two-Dimensional Random Aggregate.** In two-dimensional space, the major consideration of generating mesoscopic model is requirement of both grading of aggregates and its volume fraction in concrete. Generally, the mesoscopic structure of aggregate is randomly generated by dispersing particles in given shape and size in a limited square or rectangle space. This process was fulfilled by two essential steps, including constructing qualified aggregate and dispersing the aggregate. An applicable approach introduced in this paper was depicted as follows.

- (1) Construction of aggregate in given shape and size regarding grading of concrete: the convex polygon of an applicable aggregate is connected along the points on the curve of a randomly generated ellipse, the area of which meets the requirement of

design particle size. Then, the preliminary inscribed polygon is enlarged to match the same area of designed ellipse.

Two additional points to guarantee reasonable shape of aggregate should be noted. In practical concrete engineering, elongated aggregate (with dimension ratio over 2:1) should be avoided considering its poor structural performance. Thus, in aggregate generation program, all vertices of polygon are well distributed on ellipse in terms of the included angle defined by the connecting line of vertices of polygon and its centroid (Figures 6(a) and 6(b)). Another measurement is controlling the area occupancy of polygon within the design ellipse (Figures 6(c) and 6(d)). Detailed values for minimum included angle and minimum area occupancy are designed by domestic specification for aggregates.

- (2) Dispersing aggregate by judgement of overlapping of aggregates: within two-dimensional space, for one newly dispersed aggregate, checking its involvement within given rectangle analysis region and overlapping with all existing aggregates are required. The first condition can be met by checking whether the maximum and minimum coordinates of polygon are covered by the rectangle. The detailed judgement for overlapping of convex polygon was described as follows. Terms quoted are shown in Figure 7.

- (i) For each pair of aggregates, judge whether sum of outer radius ( $R_0 + R'_0$ ) is larger than distance of centroids ( $d_{agg}$ ). Here, outer radius is defined as the maximum radical distance from any vertex to centroid. If no ( $(R_0 + R'_0) \leq d_{agg}$ ), there is no overlapping of aggregate and the newly dispersed aggregate is accepted. If yes ( $(R_0 + R'_0) \geq d_{agg}$ ), possible overlapping cannot be avoided and continue to next step for further check.
- (ii) Judge whether sum of inner radius ( $R_i + R'_i$ ) is smaller than distance of centroids ( $d_{agg}$ ). Here, inner radius is defined as the minimum radical distance from any side to centroid. If no ( $(R_i + R'_i) > d_{agg}$ ), solid overlapping appears and a redispersion of new aggregate is required. If equal ( $(R_i + R'_i) = d_{agg}$ ), a rare case representing parallel sides of aggregates is inappropriate which is also unaccepted. If yes ( $(R_i + R'_i) < d_{agg}$ ), intersected sides cannot be avoided continue to next step for further check.
- (iii) Judge whether the vertices of polygon representing aggregate are inclusion of the existing aggregate (Figure 8). If yes, overlapping is proved and a redispersion of new aggregate is required. If no, a complicated case of overlapping that intersection polygons without any vertex located within each polygon still cannot be assured and continue to next step.
- (iv) The last step is judging whether there are any shared nodes of background meshing grid for both polygons (Figure 9). If yes, overlapping is proved and a redispersion of new aggregate is

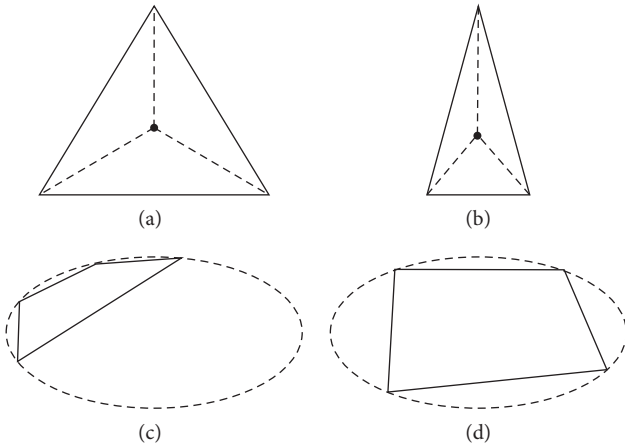


FIGURE 6: Generating polygon of aggregate based on ellipse. (a) Acceptable aggregate. (b) Elongated aggregate. (c) Low area proportion. (d) Fair area proportion.

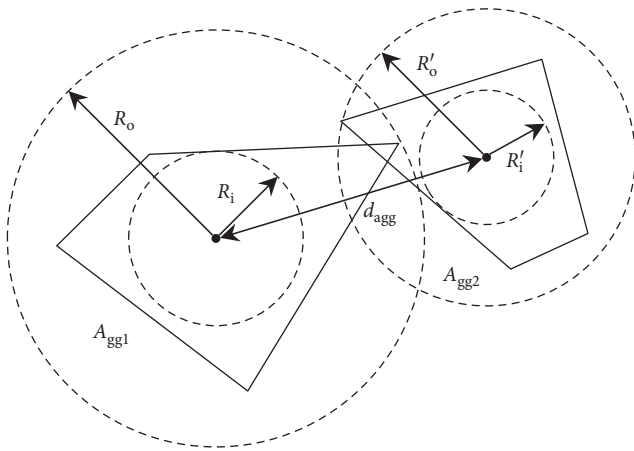


FIGURE 7: Inner radius, outer radius, and distance of centroids of two intersected aggregates.

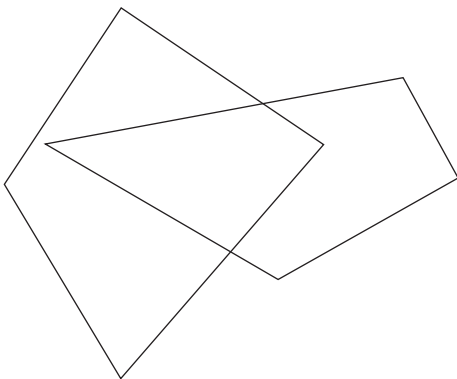


FIGURE 8: Inclusion of vertices owned by dispersed aggregate in existing aggregate.

required. If no, the newly dispersed aggregate is accepted.

The above process was illustrated in Figure 10. Two typical models with elongated aggregate are shown in Figure 11.

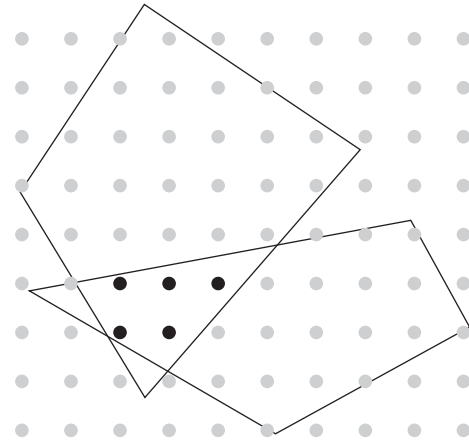


FIGURE 9: Shared nodes of background meshing grid for both polygons.

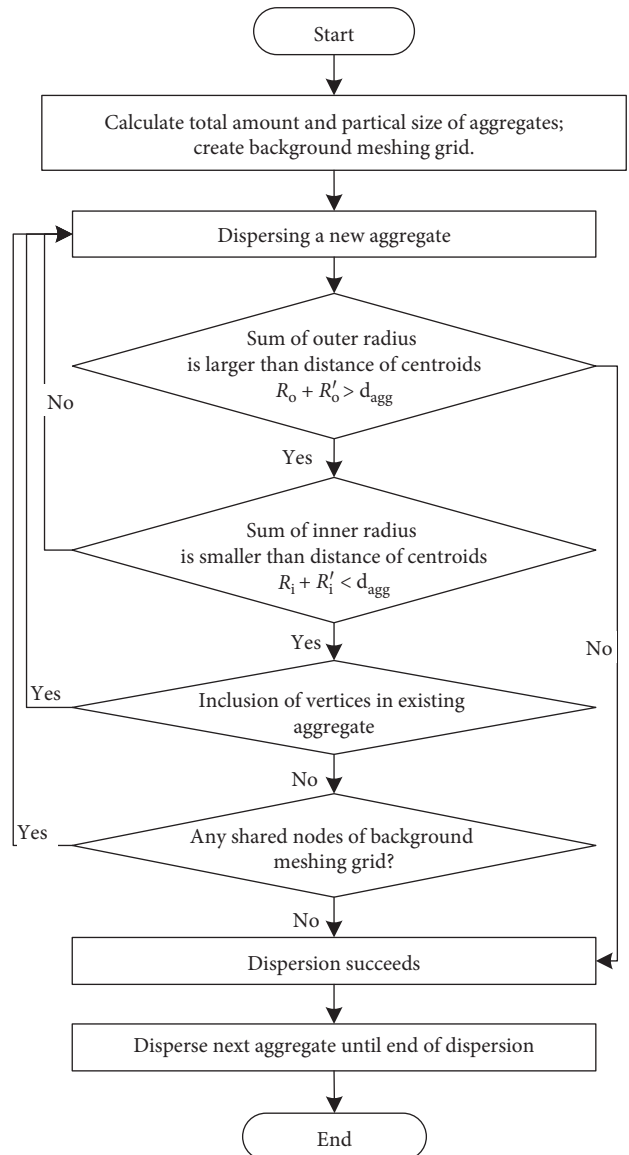


FIGURE 10: Process of generating random polygonal aggregates.

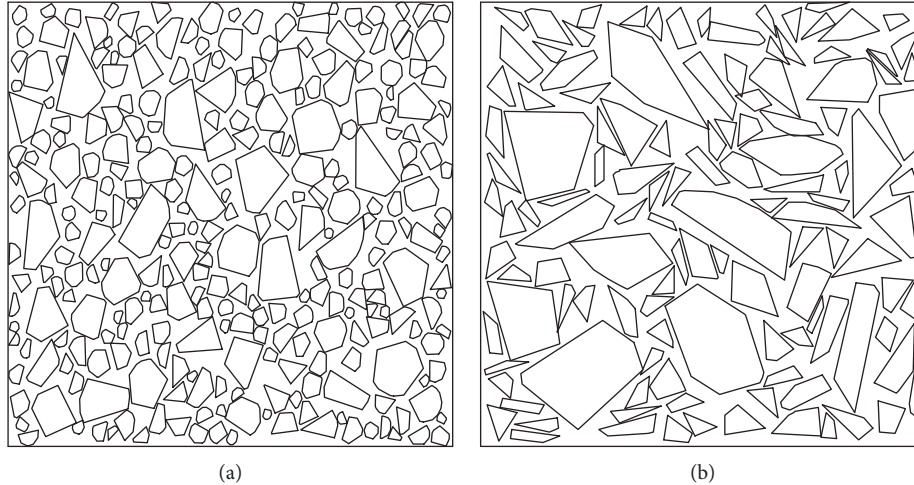


FIGURE 11: Generated aggregates with limitation on dimension ratio. (a) Allowable dimension ratio up to 2 : 1. (b) Allowable dimension ratio up to 5 : 1.

Additional process for modeling is meshing the geometry space including significantly irregular distribution of aggregate. Conventional commercial software was adopted for meshing process. However, low success rate of meshing in refined quadrilateral element cannot be avoided for most commercial software due to the complex model. Thus, an optimized way adopted in this paper was meshing the space in triangle element and subdividing one triangle into four small quadrilaterals, which was proved as high meshing success rate and high efficiency.

**3.2. Modeling of ITZ Based on Meshed Space.** Modeling approach for ITZ was determined by the mechanism of simulating chloride diffusion within ITZ. ITZ was recognized as an indeterminate zone around aggregates and bulk, in linearly decreasing porosity with increase of distance from aggregate surface. Existing approaches describe ITZ as an individual layer or compensation on equivalent diffusivity of aggregate [44–46]. In terms of aggregates in random polygon, the way of building actual elements of ITZ was adopted in this paper. Thus, more DOFs were introduced, which significantly increased time consumption of assembling global diffusion matrix and solving it.

Since ITZ was identified as the individual phase surround aggregate, additional uniform width of elements adhering on the edge of aggregates might induce unnecessary overlapping of ITZ elements in some cases that the pair of aggregate was too close to each other. In order to avoid the above circumstance, ITZ elements were assigned on the inner side of edge of aggregate instead of outer side. According to minor area proportion of ITZ, it was acceptable slightly decreasing the size of aggregate. There are totally three steps for this process.

- (i) For the first step, for any aggregate, the lines on its edge were parallel offset inside by the designed width,  $h$ , shown as the dashed line in Figure 12(a).
- (ii) For the second step, all intersection of the offset lines were found, the total number of which were

equal to vertices of aggregate, shown as the black point in Figure 12(b). Additionally, a special subroutine called “func\_L2L” was developed to identify the relationship of a pair of line segments. Its output result provided whether the two line segments intersect and the coordinate of their intersection.

- (iii) For the third step, combining the previous available nodes of aggregate and newly generated nodes (intersection), a group of quadrilateral elements was built in counterclockwise order, which represented ITZ. Their physical properties were set individually being different from existing cement paste.

The above entire process of modeling FE model of concrete involving ITZ is shown in Figure 13.

## 4. Basis of Assessing Approach

**4.1. Diffusion Model of Chloride.** Transportation of chloride ion in porous medium such as cementitious materials is mainly a diffusive phenomenon due to concentration gradients [47]. The diffusion of chloride ion within concrete components was admitted as a complex process, which was influenced by many factors including water/cement ratio, porosity of cement, additive, aggregate, temperature, humidity, environmental chloride content, binding effect of binder, and hydration of cement. The above process could be simulated by numerical approach based on available environmental attacking condition and material properties. Fick’s second law was widely adopted as the expression of principle differential equation [48]:

$$\omega_e \frac{\partial C_f}{\partial t} = \frac{\partial}{\partial x} D_e \omega_e \frac{\partial C_f}{\partial x} - \frac{\partial C_b}{\partial t}, \quad (18)$$

$$C_t = C_b + C_f \cdot \omega_e,$$

where  $C_f$  is the free chloride content (in  $\text{kg}/\text{m}^3$  of solution);  $C_b$  is the bound chloride content (in  $\text{kg}/\text{m}^3$  of concrete);  $C_t$  is the total chloride content (in  $\text{kg}/\text{m}^3$  of concrete);  $D_e$  is the



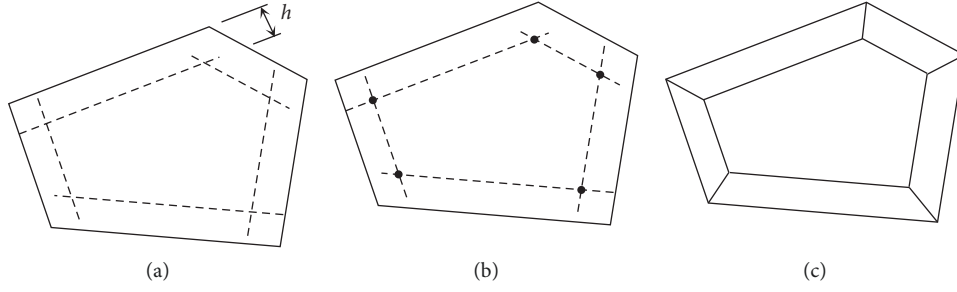


FIGURE 12: Process of generating new elements and nodes for ITZ. (a) Step 1: offset outline with ITZ width,  $h$ . (b) Step 2: find intersection (nodes) of outline. (c) Step 3: form elements of ITZ.

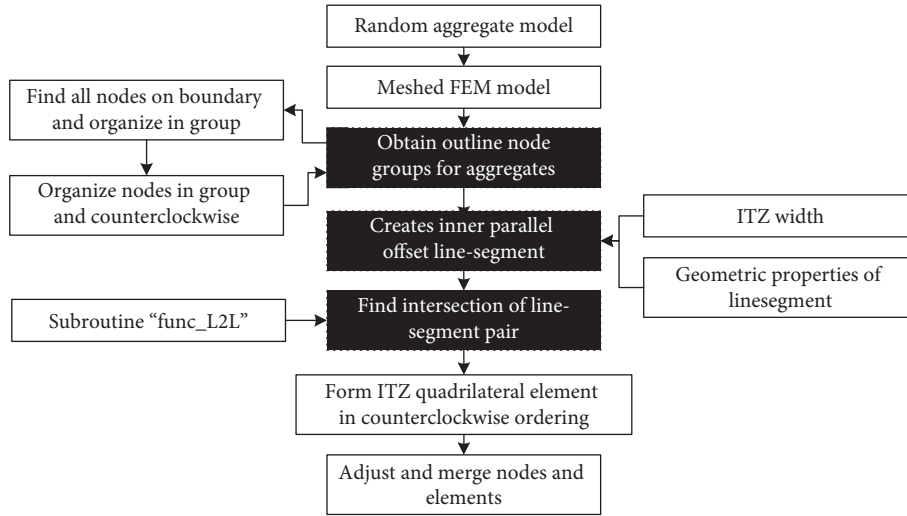


FIGURE 13: Flow chart for modeling of ITZ based on meshed FEM model.

effective diffusivity; and  $\omega_e$  is the evaporable water content (in volume percentage of concrete). Considering complexity of cross sections of bridge pier, appropriate preliminary division and meshing grid are processed by means of some meshing tools or commercial FE software. Experimental data indicated that due to cement hydration and chloride content, the chloride diffusion coefficient is strongly dependent on the exposure period of concrete [49].

**4.2. Corrosion Model of Rebar.** Corrosion of rebar initiates in the form of galvanic reaction between ferrous and oxygen accelerated by the presence of active free chloride ion once the protection of high pH (>12.5) hydration products was de-passivated. Corrosion continues with the cycle of electric current between cathode and anode, which was influenced by high chloride concentration at the level of the rebar, environmental temperature, electrical resistivity of concrete, and hydration of cement. The corrosion model regressed by Liu and Weyers [34] based on experimental data included the influence of chloride content, temperature, concrete cover resistance, and time of cement hydration, which was expressed as

$$\ln(1.08i_{\text{corr}}) = 8.37 + 0.618 \cdot \ln(1.69\text{Cl}) - \frac{3034}{T} - 0.000105R_c + 2.32t^{-0.215}, \quad (19)$$

where  $i_{\text{corr}}$  is corrosion current intensity ( $\mu\text{A}/\text{cm}^2$ ); Cl is chloride content ( $\text{kg}/\text{m}^3$ ), which was obtained from numerical simulation result of chloride diffusion;  $T$  is temperature at the depth of steel surface (in degree Kelvin);  $R_c$  is the resistance of the cover concrete (ohms); and  $t$  is corrosion time duration (years). With the data chloride content obtained by numerical simulation and the other parameters assumed previously, the real-time corrosion current rate at each time step of numerical simulation was calculated by equation (19). Thus, the corrosion depth on surface of rebar was calculated as [50]

$$D_{t+\Delta t} = D_t - 0.023 \cdot i_{\text{corr}} \Delta t, \quad (20)$$

where  $D_t$  is remaining rebar diameter (mm) at  $t$  years, here 20 mm adopted;  $D_{t+\Delta t}$  is reduced rebar diameter (mm) at  $t + \Delta t$  years; and  $\Delta D|_{\Delta t}$  is reduction of rebar diameter (mm) for the period of propagation for the duration time of  $\Delta t$  years.

## 5. Numerical Simulation for Diffusion of Chloride Including Compensation

**5.1. Influence of ITZ Properties regarding Compensation.** Considering that characteristics of ITZ significantly influence diffusion chloride within concrete, critical properties of

ITZ were detailed studied in this section, including diffusivity and width of ITZ, aggregate volume fraction, and grade of aggregate. Furthermore, chloride content on surface of rebar was also researched regarding presence of ITZ.

Another major consideration of this paper was the effect of compensation in multiscale modeling. A  $100 \times 100$  mm two-dimensional square space was modeled for mesoscopic core part, and another  $100 \times 200$  mm rectangle space was modeled for macroscopic compensation part (Figure 14). Width of ITL was set at 10 mm, which means 10% area of core part and 5% area of compensation part were overlapped. On the other hand, for the case without compensation, macroscopic compensation part was deleted and chloride ion can only diffuse within smaller mesoscopic core part.

For the other parameters, transportation mechanism of chloride ion between both parts was described in previous section of this paper. For all simplified cases studied in this section, the analytical apparent surface chloride content of 0.71 ( $\%w_c$ ) and apparent concrete diffusivity of  $1.84 \times 10^{-12} \text{ m}^2/\text{s}$  were adopted for macroscopic model, which were regressed based on Zhao's data [51]. Meanwhile, the aggregate was considered as impermeable and corresponding modeling of FEM was ignored. Boundary condition and diffusivity of cement paste were calculated by these results. Regarding generating random aggregate of mesoscopic model, Fuller's curve was adopted as the grading of aggregate. Both types of cases with compensation and without compensation were studied.

Significant random distribution of aggregate was the major factor for uncertainty of chloride diffusion. Thus, totally, 100 specimens of aggregate model for each case were generated and analyzed considering reasonable accurate and acceptable time consumption. After all specimens were analyzed, mean results of these cases were calculated for further comparison.

**5.1.1. Diffusivity of ITZ.** Firstly, diffusivity of ITZ was studied, which was represented by the ratio of  $D_{ITZ}/D_{CP}$ . Here,  $D_{ITZ}$  and  $D_{CP}$  denoted the diffusivity in ITZ and cement paste, respectively. As was discussed by Zheng et al. [4],  $D_{ITZ}/D_{CP}$  would vary within 1~5 considering different configuration of w/c, aggregate size, hydration time, and aggregate fraction theoretically, which were discussed by means of the approach introduced in this paper.  $50 \mu\text{m}$  of ITZ width was modeled by expanding the edge of aggregate and rebar. Maximum aggregate size in 20 mm was considered.

Figure 15 showed typical distribution of chloride content regarding different diffusivity in ITZ. The major difference of contour line observed was the slightly higher chloride content due to the presence of ITZ in width of the micrometer scale. It means higher diffusivity in ITZ compared with cement paste accelerated the diffusion of chloride within concrete.

For mesoscopic numerical simulation, distribution of aggregate was recognized as the major influence factor for development of chloride [52]. Chloride content on surface of rebar significantly varied with different arrangement and grading of aggregate. Thus, both mean and

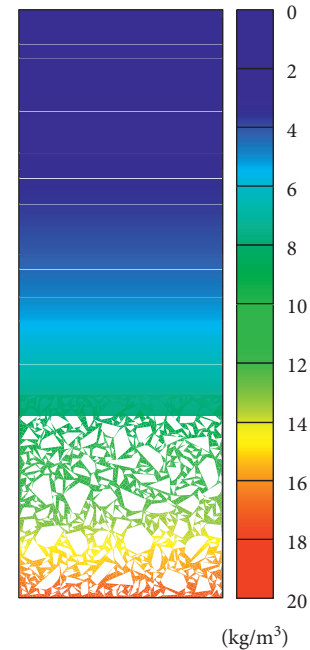


FIGURE 14: Contour of chloride content of multiscale model.

maximum distribution of chloride ion in terms of random aggregate models became the major consideration. Figures 16 and 17 summarized average content and maximum versus depth regarding diffusivity of ITZ at 50 years and 100 years, respectively. It was clearly noted that chloride content increased as the diffusivity of ITZ increased. An interesting phenomenon observed was that the influence of compensation was larger in higher chloride content. It attributed to a larger diffusion space released in mixed model including compensation part. From the result of numerical simulation, another point should be noted that within the boundary layer in width of 10 mm from surface of concrete, both mean and maximum chloride content were closed to boundary condition, which was recognized as the lower aggregate volume fraction and smaller particle size in this region.

**5.1.2. ITZ Width.** The second major factor for chloride diffusion is ITZ width. A thin layer composed of quadrilateral elements in the width of  $5 \mu\text{m}$ ,  $10 \mu\text{m}$ ,  $20 \mu\text{m}$ ,  $35 \mu\text{m}$ , and  $50 \mu\text{m}$  adhering to the edge of aggregates was modeled (Figure 18). For the other parameters, diffusivity of ITZ in  $D_{ITZ}/D_{CP} = 5$  was adopted. Maximum particle size of coarse aggregate was limited within  $D_{\text{max}} = 20 \text{ mm}$ . Figure 18 showed ITZ elements in orange color of FE model in different width of ITZ.

Figures 19 and 20 showed average content and maximum versus depth regarding width of ITZ at 50 years and 100 years, respectively. A clear conclusion was drawn that thicker ITZ width induced higher volume fraction of ITZ and enhanced diffusion of chloride ion.

**5.1.3. Aggregate Volume Fraction.** Aggregate volume fraction determined total amount of aggregates within given space and accordingly total length of perimeter was also determined, which was the key factor for proportion of ITZ

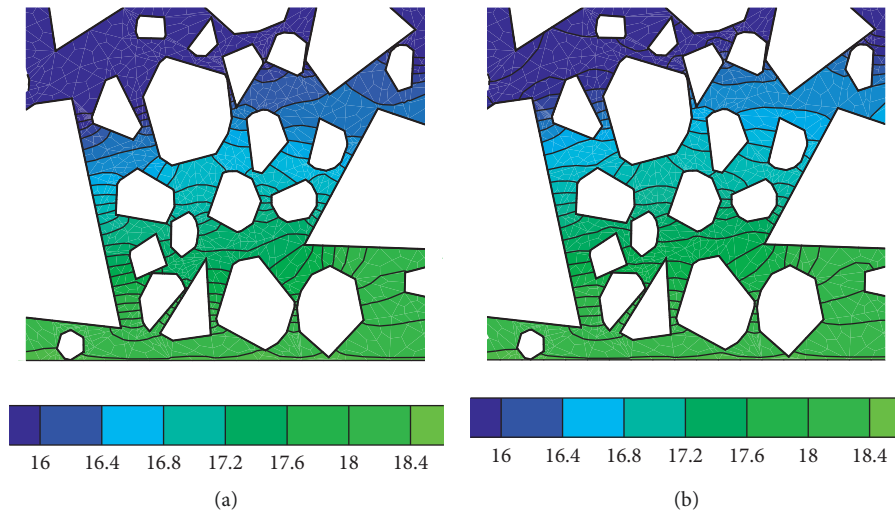


FIGURE 15: Typical distribution of chloride content regarding diffusivity in ITZ (solid line denotes isoline of chloride content). (a)  $D_{ITZ}/D_{CP} = 1$ . (b)  $D_{ITZ}/D_{CP} = 5$ .

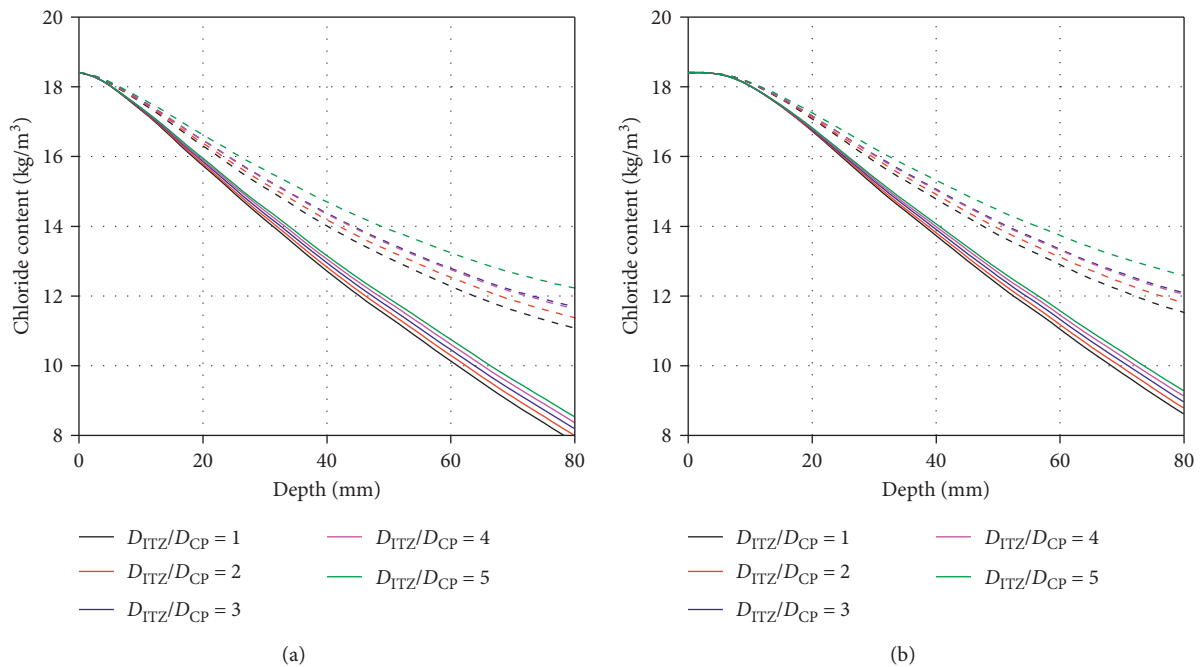


FIGURE 16: Average content and maximum vs. depth regarding compensation and ITZ  $D_{ITZ}/D_{CP}$  at 50 y of exposure (dashed: w/o compensation; solid: with compensation). (a) Mean chloride content. (b) Maximum chloride content.

in concrete. In this section, the cases of aggregate volume fraction in 20%, 30%, 40%, 50%, 60%, and 70% were discussed by means of the approach introduced in this paper. Diffusivity of ITZ in  $D_{ITZ}/D_{CP} = 5$  and  $50 \mu\text{m}$  of ITZ width were adopted. Maximum aggregate size in 20 mm and Fuller grading was adopted. Both types of cases with compensation and without compensation were studied. Figure 21 showed with aggregate volume fraction from 20% to 70%, the typical distribution of chloride content and aggregate with given analysis square space.

Figure 22 described mean content and maximum versus depth regarding aggregate volume fraction at 100 years.

According to the result, presence of ITZ provided greater effect on higher aggregate volume fraction and thus reduced the difference of chloride content profile in cases with different aggregate volume fraction.

**5.1.4. Grade of Aggregate.** The cases for grade of aggregate with maximum aggregate size  $D_{\text{max}} = 5 \text{ mm}$ , 10 mm, 15 mm, 20 mm, 25 mm, and 30 mm were discussed. Both cases with or without ITZ were included. Fuller grading was adopted. For the case with ITZ, diffusivity of ITZ in  $D_{ITZ}/D_{CP} = 5$  was adopted.  $50 \mu\text{m}$  of ITZ width was modeled by expanding the

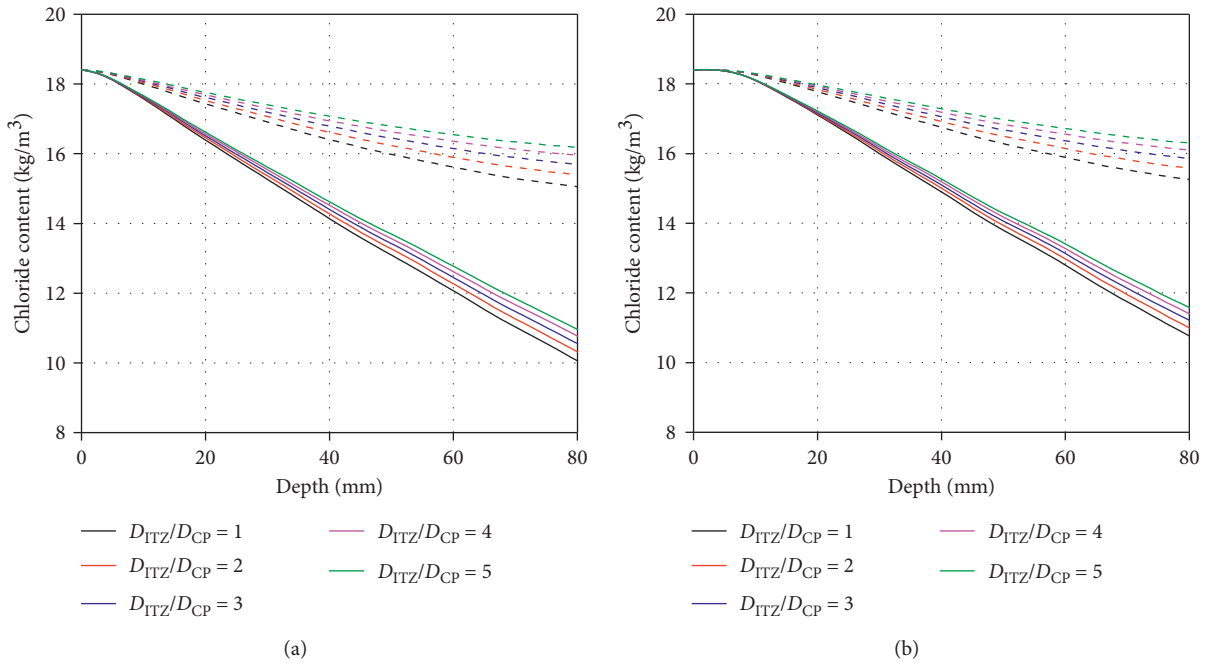


FIGURE 17: Average content and maximum vs. depth regarding compensation and ITZ  $D_{ITZ}/D_{CP}$  at 100 y of exposure (dashed: w/o compensation; solid: with compensation). (a) Mean chloride content. (b) Maximum chloride content.

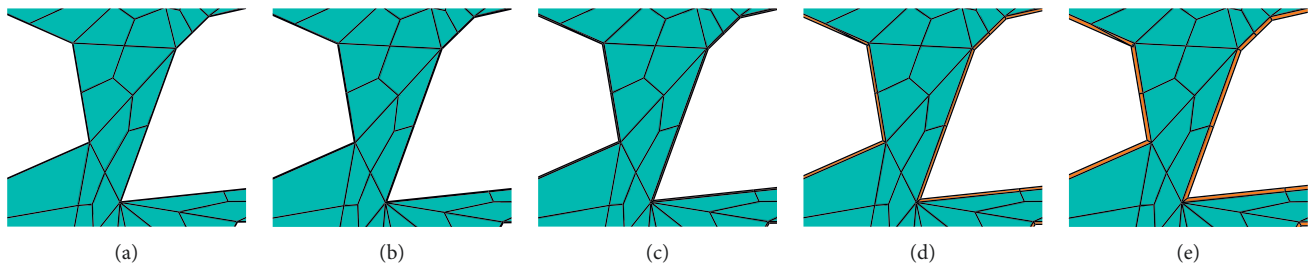


FIGURE 18: FE model for cement paste and ITZ regarding ITZ width,  $h$  (blue: cement paste; orange: ITZ). (a)  $h = 5 \mu\text{m}$ . (b)  $h = 10 \mu\text{m}$ . (c)  $h = 20 \mu\text{m}$ . (d)  $h = 35 \mu\text{m}$ . (e)  $h = 50 \mu\text{m}$ .

edge of aggregate and rebar. Both types of cases with compensation and without compensation were studied. Figure 23 showed with maximum aggregate size from 5 mm to 30 mm, the typical distribution of chloride content and aggregate with given analysis square space. Figure 24 showed mean content and maximum versus depth regarding grade of aggregate at 100 years.

Figure 24 summarized mean and maximum chloride content vs. depth from surface of concrete. An interesting point should be noted that the lower aggregate volume fraction and smaller particle size in the region closed to boundary was not significant in the case with smaller maximum particle size. Moreover, presence of ITZ indeed enhanced diffusion of chloride ion especially in cases with smaller maximum particle size.

**5.2. Chloride Content and Corrosion of Steel Rebar.** In this section, chloride content on the front of rebar in terms of the configuration was studied by the multiscale numerical simulation introduced previously. According to general

engineering design, a group of concrete cover thickness and rebar diameter was devised for detailed comparison of chloride diffusion and rebar corrosion, shown in Table 1. For the purpose of comparison, rebar in diameter of 16 mm was selected for the cases in different cover thickness and 50 mm cover thickness for the comparison of rebar diameters. By means of the random aggregate generation approach and considering reasonable computing loading, 100 two-dimensional samples for each combination of concrete cover thickness and rebar diameter was modeled considering random distribution of aggregate.

Considering three-phase composite of concrete, nodes and elements of ITZ were modeled not only surrounding aggregate, but also on the surface of steel rebar. It also justified to a certain extent that the formation of ITZ on surface of steel rebar in the light of the same mechanism of aggregate. Therefore the same width and diffusivity of ITZ on surface of steel were adopted. Chloride content on front of rebar was extracted from the newly created nodes on the edge of ITZ elements in terms of the neat surface of steel rebar.

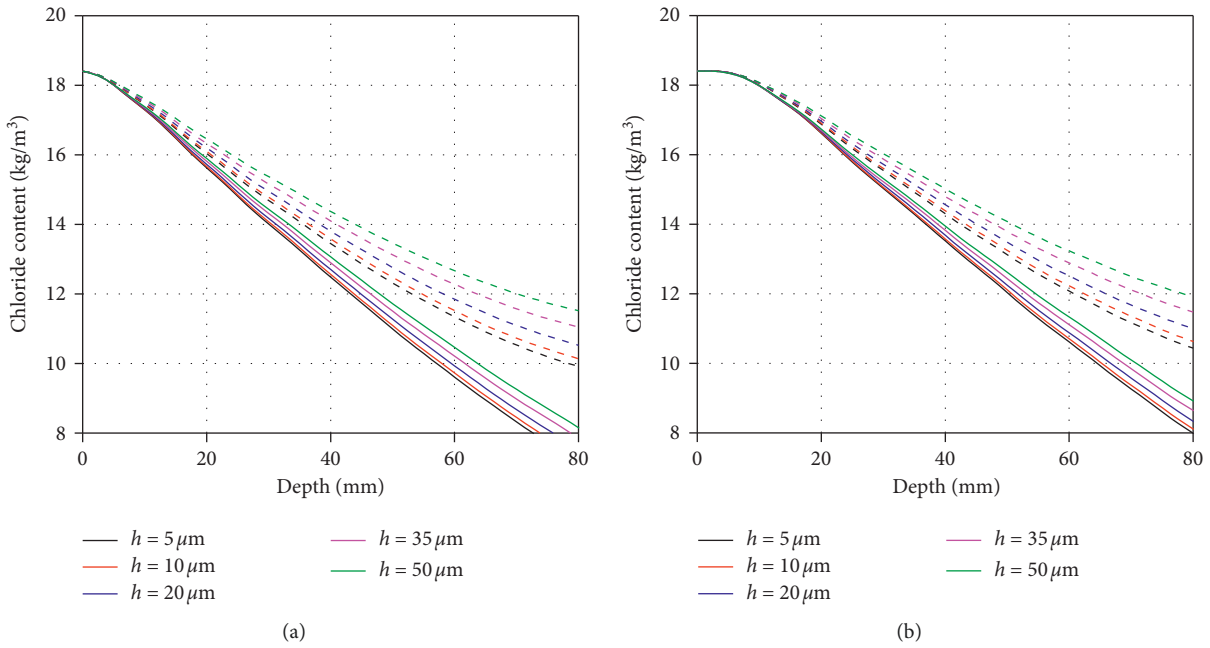


FIGURE 19: Average content and maximum vs. depth regarding compensation and ITZ width at 50 y of exposure (dashed: w/o compensation; solid: with compensation). (a) Mean chloride content. (b) Maximum chloride content.

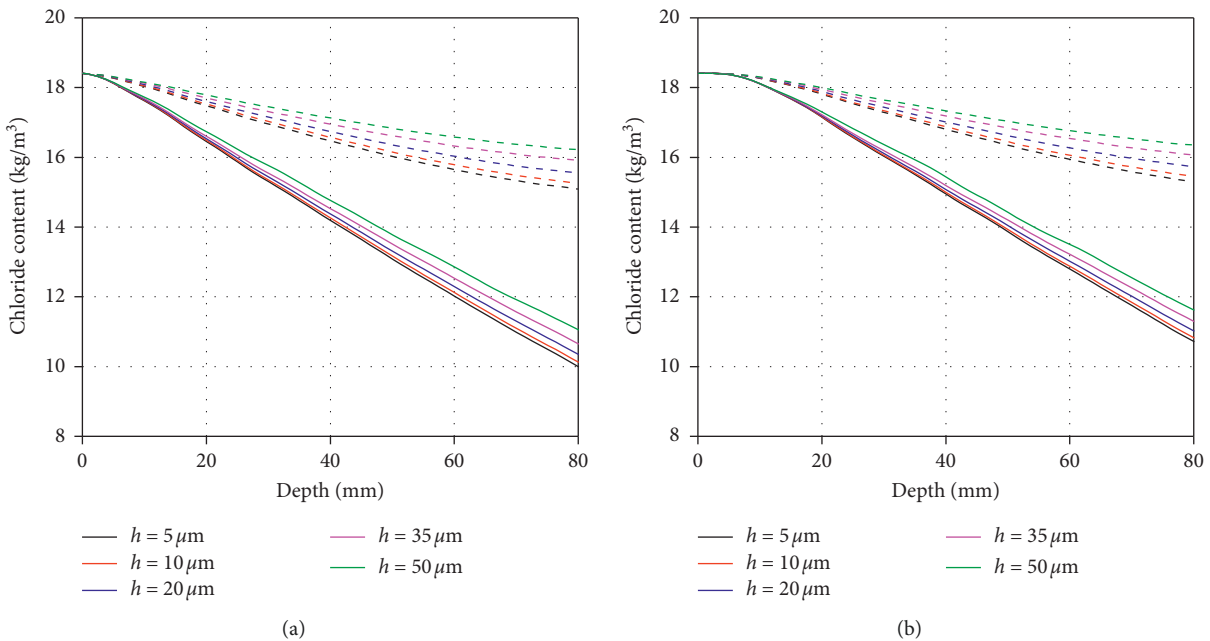


FIGURE 20: Average content and maximum vs. depth regarding compensation and ITZ width at 100 y of exposure (dashed: w/o compensation; solid: with compensation). (a) Mean chloride content. (b) Maximum chloride content.

The placement of steel rebar on the center of straight edge was considered. Rebar placed in the center of bottom side of concrete section (Figure 25(a) listed in Table 1 was tested. Term  $d$  denotes the cover thickness and the diameter;  $D$  of circle refers to diameter of rebar. A two-dimensional mesoscopic core model in the size of  $100 \times 100$  mm was created. In order to guarantee the effect of compensation,  $100 \times 200$  mm total size of compensation

model was designed as two times of core model. 10 mm thickness of ITL was considered for compensation process. Apart from ITZ elements surrounding aggregates, new elements adjacent to steel rebar were also modeled by expanding outline. Therefore, chloride content on surface of rebar was extracted from the newly built nodes of ITZ. Both types of cases with compensation and without compensation were studied. Diffusivity of ITZ in  $D_{ITZ}/$



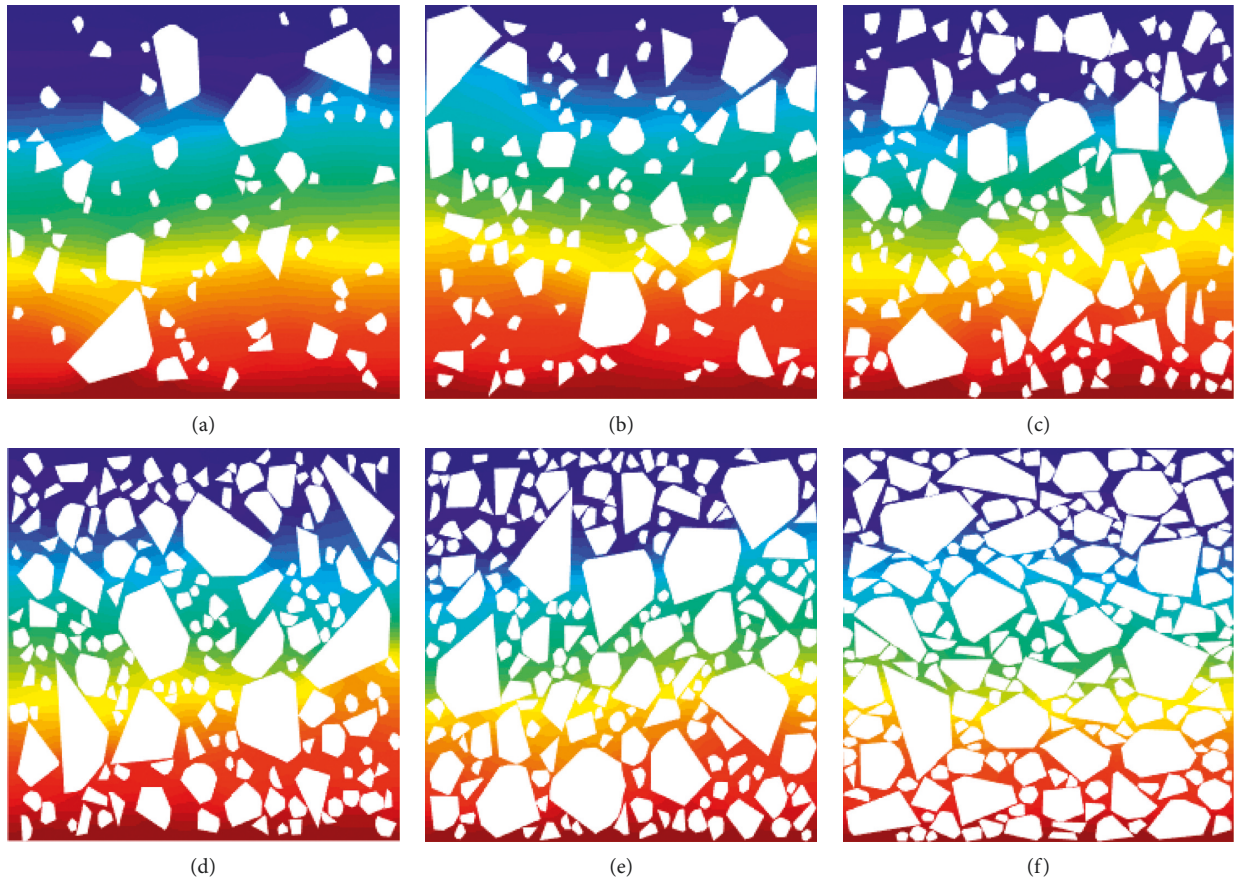


FIGURE 21: FE model and typical distribution of chloride content for different aggregate volume fraction,  $fa$ . (a)  $fa = 20\%$ . (b)  $fa = 30\%$ . (c)  $fa = 40\%$ . (d)  $fa = 50\%$ . (e)  $fa = 60\%$ . (f)  $fa = 70\%$ .

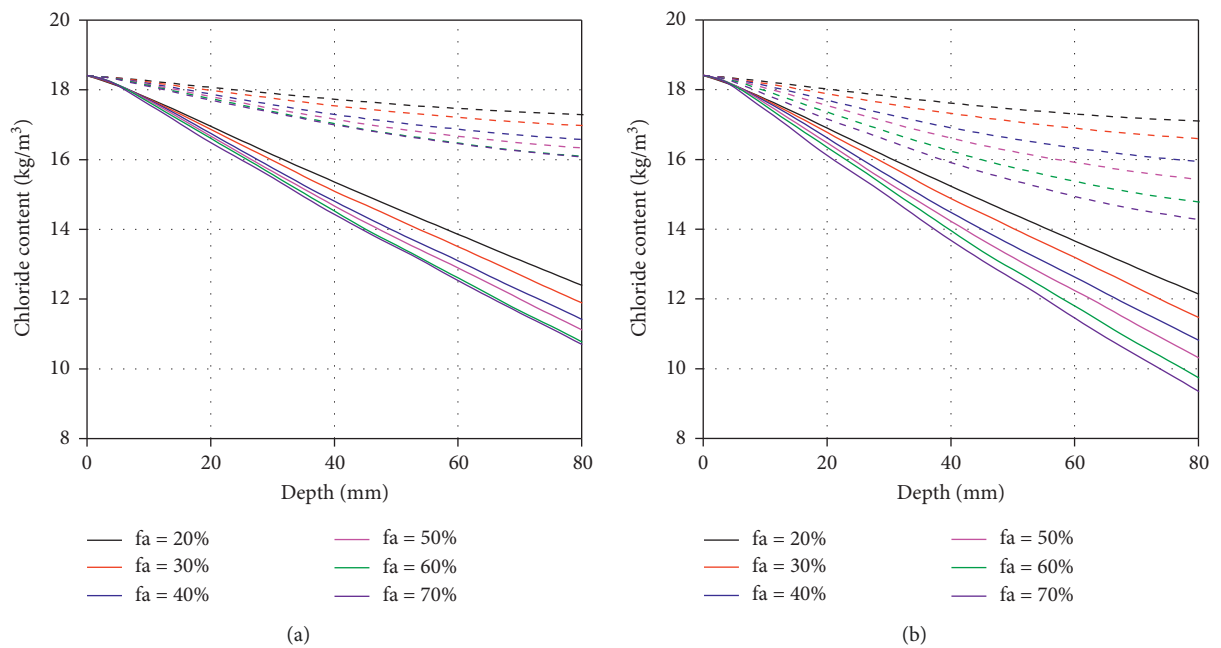


FIGURE 22: Continued.



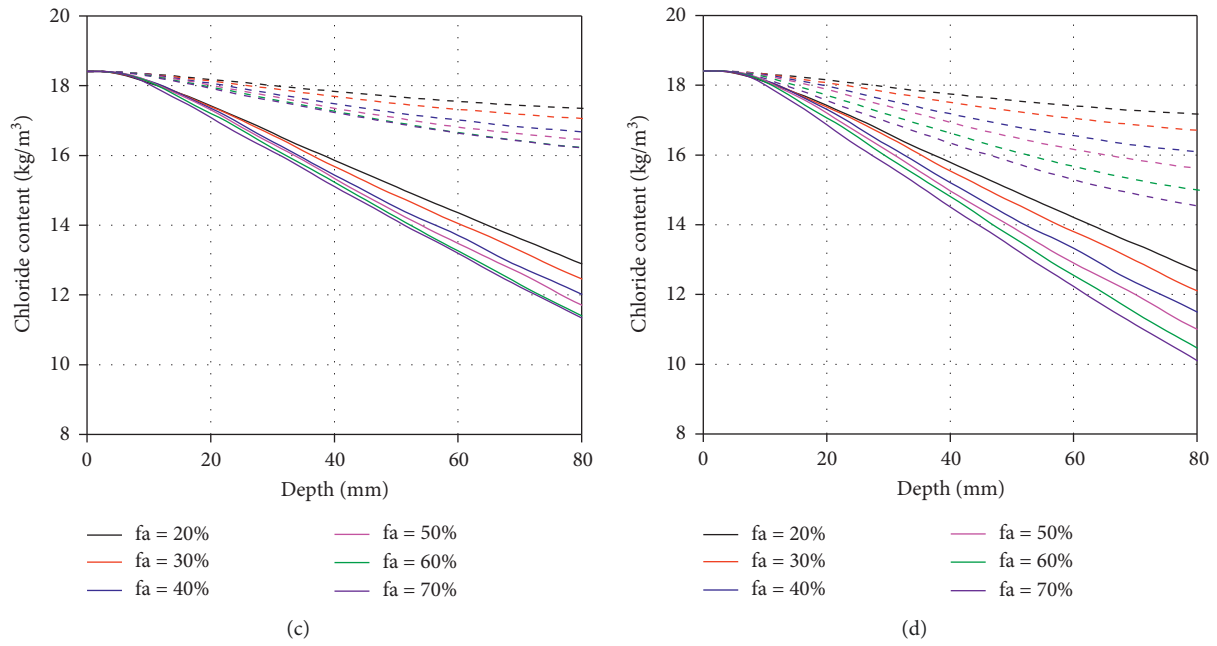


FIGURE 22: Average content and maximum vs. depth regarding aggregate volume fraction ( $f_a$ ) and presence of ITZ at 100 y of exposure (dashed: w/o compensation; solid: with compensation). (a) Mean chloride content with ITZ. (b) Mean chloride content w/o ITZ. (c) Max chloride content with ITZ. (d) Max chloride content w/o ITZ.

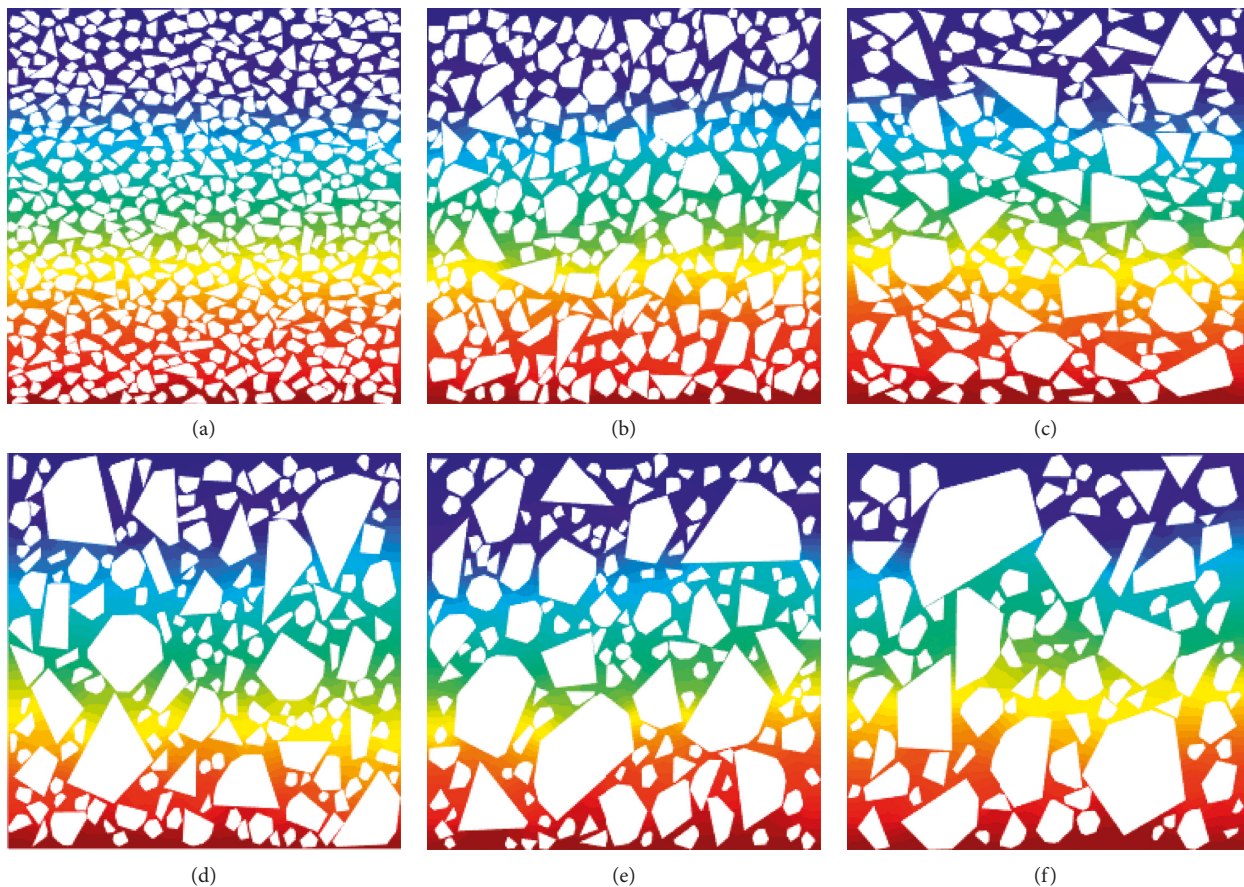


FIGURE 23: FE model and typical distribution of chloride content for different aggregate and gradation. (a)  $D_{max} = 5$  mm. (b)  $D_{max} = 10$  mm. (c)  $D_{max} = 15$  mm. (d)  $D_{max} = 20$  mm. (e)  $D_{max} = 25$  mm. (f)  $D_{max} = 30$  mm.

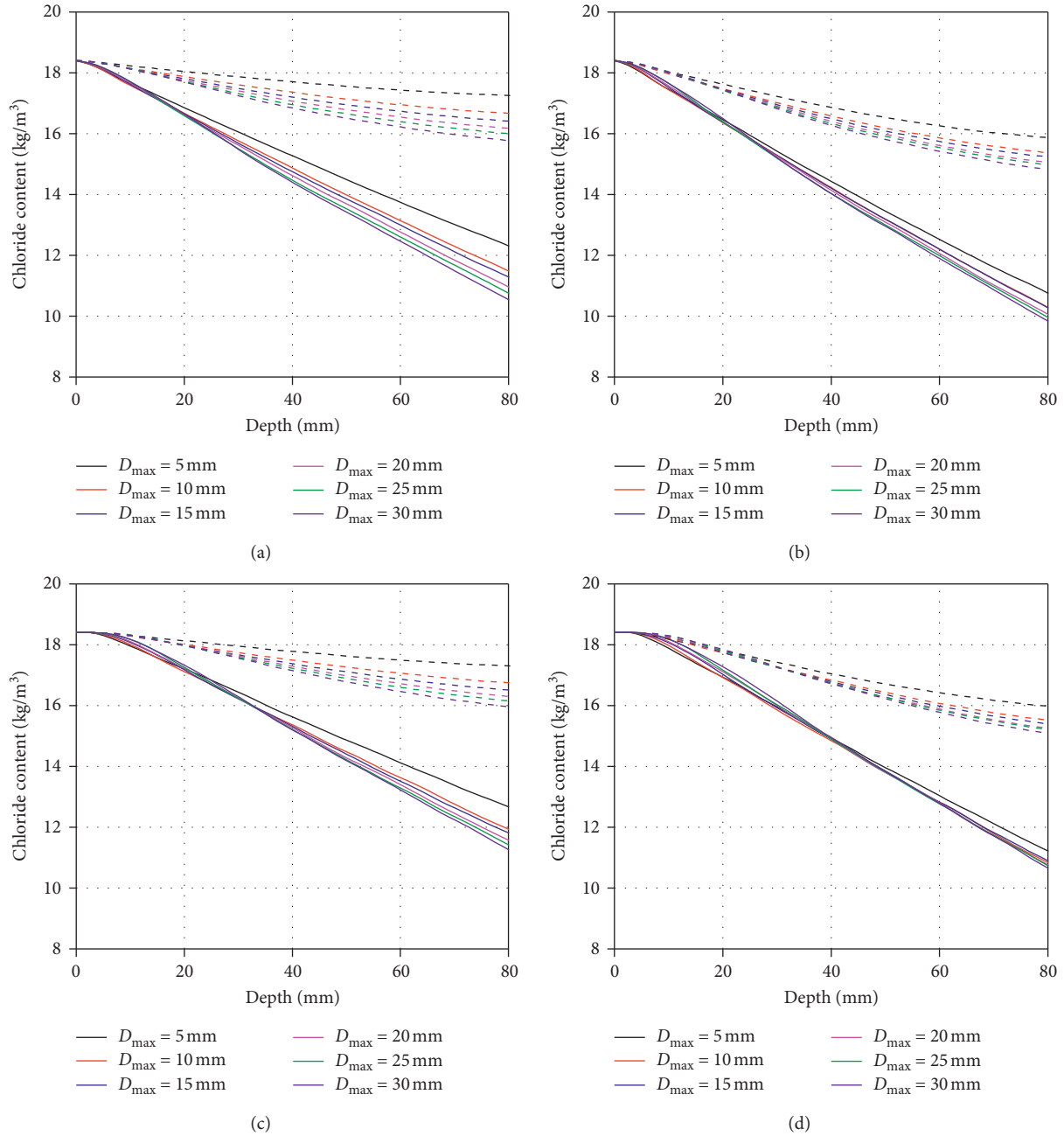


FIGURE 24: Average content and maximum vs. depth, regarding grade of aggregate and presence of ITZ (dashed: w/o compensation; solid: with compensation). (a) Mean with ITZ. (b) Mean w/o ITZ. (c) Max with ITZ. (d) Max w/o ITZ.

TABLE 1: Details of model comparison for concrete cover thickness and rebar diameter regarding chloride diffusion and rebar corrosion.

Cover thickness, $C$ (mm)	Rebar diameter, $D$ (mm)				
	12	16	20	25	28
20		×			
30		×			
40		×			
50	×	×	×	×	×
60		×			

$D_{CP} = 5$  was adopted.  $50 \mu\text{m}$  of ITZ width was modeled by expanding the edge of aggregate and rebar. Maximum aggregate size in 20 mm was considered, and Fuller grading was adopted.

Figure 25(b) showed typical distribution of chloride content within core mesoscopic model and compensated macroscopic model at 100 years of exposure period for the cases of rebar placed in center of bottom. The contour clearly described sound transition of chloride content near ITL on both cases and proved the effect of compensation as well.

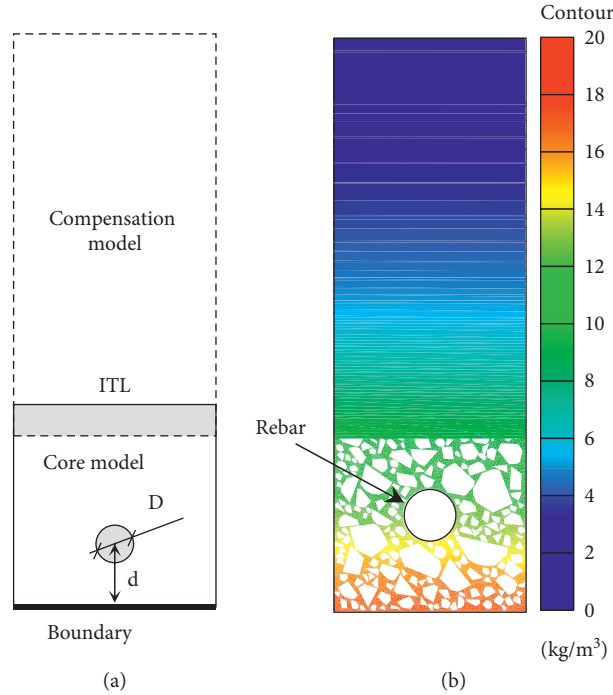


FIGURE 25: Geometrical configuration and chloride content distribution of compensation case. (a) Geometrical configuration of concrete analysis space and rebar. (b) Typical distribution of aggregate and chloride content in concrete, 100 y.

The circle curve of rebar was meshed into a series of node, and nodal chloride content was obtained from result of FE analysis. For all 100 samples of each research case, mean value of chloride content on each node around rebar was calculated and plotted in polar coordinate. Figure 26 showed the polar distribution of mean chloride content on cross section of rebar at 20 years (solid) and 100 years (dashed) of exposure period. Depending on whether compensation model or ITZ was considered, chloride content was plotted in different colors, shown in legend on the bottom. Distribution of chloride content developed towards lower-middle, which matched the configuration of boundary condition. Result indicated higher chloride content was obtained for longer period of exposure. Moreover, lower value was observed in the cases with compensation.

Mean chloride content vs. cover thickness for 16 mm rebar and mean chloride content vs. diameter for 50 mm cover are summarized in Figure 27. An obvious result showed lower chloride content in compensation case since solid lines were all under corresponding dashed lines in the figures, which attributed the larger diffusion space in compensation cases.

Another observation was the insignificant difference between the solid line of "ITZ" and "ITZ + Compensation" (20 years). Since diffusion of chloride did not exceed the border of core part and compensation part, there was no clear difference for both diffusion spaces of "ITZ" and "ITZ + Compensation," which is the major reason.

The corrosion model regressed by Liu and Weyers [34] based on experimental data included the influence of

chloride content, temperature, concrete cover resistance, and time of cement hydration, which was expressed as

$$\ln(1.08i_{\text{corr}}) = 8.37 + 0.618 \cdot \ln(1.69\text{Cl}) - \frac{3034}{T} - 0.000105R_c + 2.32t^{-0.215}, \quad (21)$$

where  $i_{\text{corr}}$  is corrosion current intensity ( $\mu\text{A}/\text{cm}^2$ ); Cl is chloride content ( $\text{kg}/\text{m}^3$ ), which was obtained from numerical simulation result of chloride diffusion;  $T$  is temperature at the depth of steel surface (in degree Kelvin);  $R_c$  is the resistance of the cover concrete (ohms); and  $t$  is corrosion time duration (years). For corrosion calculation in the following discussion, environmental temperature 293 K was adopted. A generally adopted value of concrete resistance 1500  $\Omega$  was adopted. Besides, pitting of rebar was neglected. With the data chloride content obtained by numerical simulation, the real-time corrosion current rate at each time step of numerical simulation was calculated. The corrosion depth on surface of rebar was calculated as [50]

$$D_{t+\Delta t} = D_t - 0.023 \cdot i_{\text{corr}} \Delta t, \quad (22)$$

where  $D_t$  is remaining rebar diameter (mm) at  $t$  years, here 20 mm adopted and  $D_{t+\Delta t}$  is reduced rebar diameter (mm) at  $t + \Delta t$  years.

A single mean chloride content for each time step was calculated as the attacking chloride content for rebar, and mean corrosion depth of rebar was calculated based on equation (19). Figure 28(a) (cover thickness) and Figure 28(b) (rebar diameter) showed corrosion process and

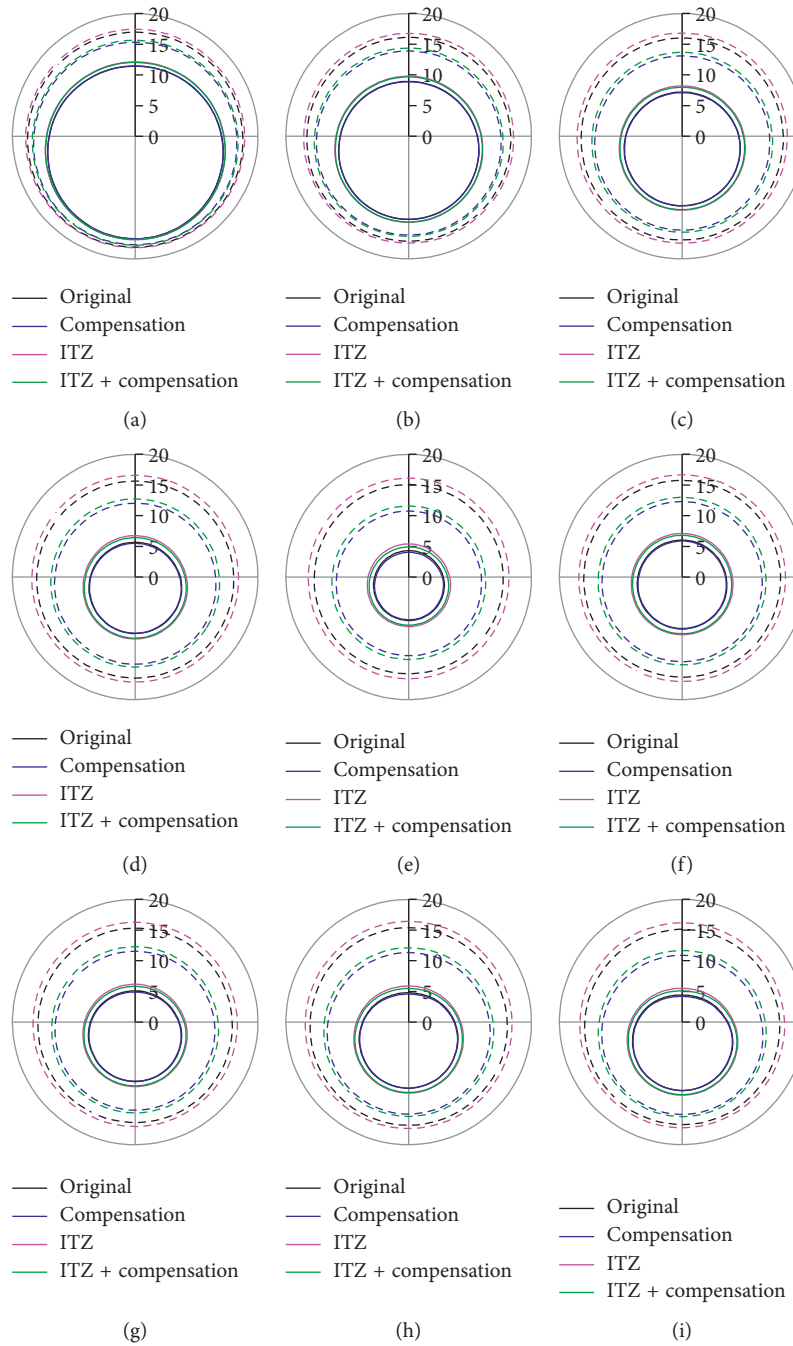


FIGURE 26: Polar distribution of chloride content on cross section of rebar on center of bottom side (solid: 20 y; dashed: 100 y). (a)  $R = 16$  mm,  $C = 20$  mm. (b)  $R = 16$  mm,  $C = 30$  mm. (c)  $R = 16$  mm,  $C = 40$  mm. (d)  $R = 16$  mm,  $C = 50$  mm. (e)  $R = 16$  mm,  $C = 60$  mm. (f)  $R = 12$  mm,  $C = 50$  mm. (g)  $R = 20$  mm,  $C = 50$  mm. (h)  $R = 25$  mm,  $C = 50$  mm. (i)  $R = 28$  mm,  $C = 50$  mm.

characteristics of rebar based on obtained distribution of chloride content around rebar. Ordinate in these figures indicated the ratio of diameter of corroded rebar to initial value.

Obtained diagrams showed less corrosion of steel rebar in the cases with compensation due to larger space for chloride diffusion and lower distributed chloride content. More obvious difference comparing between the result from the compensation model (solid) and the case without compensation (dashed) due to a longer exposure period was observed.

Moreover, it should be noted that increasing concrete cover provided slight effect on protecting steel rebar from corrosion. The higher diffusivity in ITZ adhering on steel rebar provided an equivalent express channel for diffusion of chloride ion around steel rebar. Thus, ITZ actually balanced the difference of depth from surface of concrete for these cases and insignificant difference was observed for cases in different covers. Similar phenomenon was noticed that compensation decreased chloride content on surface of rebar as well as its corrosion degree.

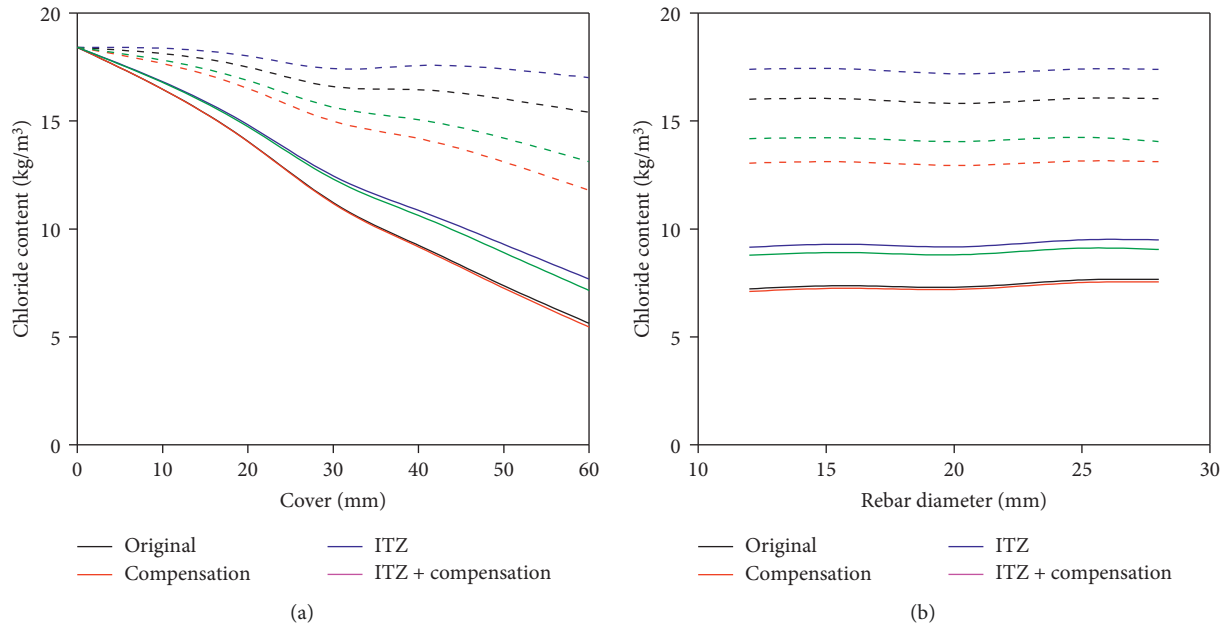


FIGURE 27: Mean chloride content of rebar on center of bottom side (solid: 20 y; dashed: 100 y). (a) Mean chloride content vs. cover thickness, 16 mm rebar. (b) Mean chloride content vs. diameter, 50 mm cover.

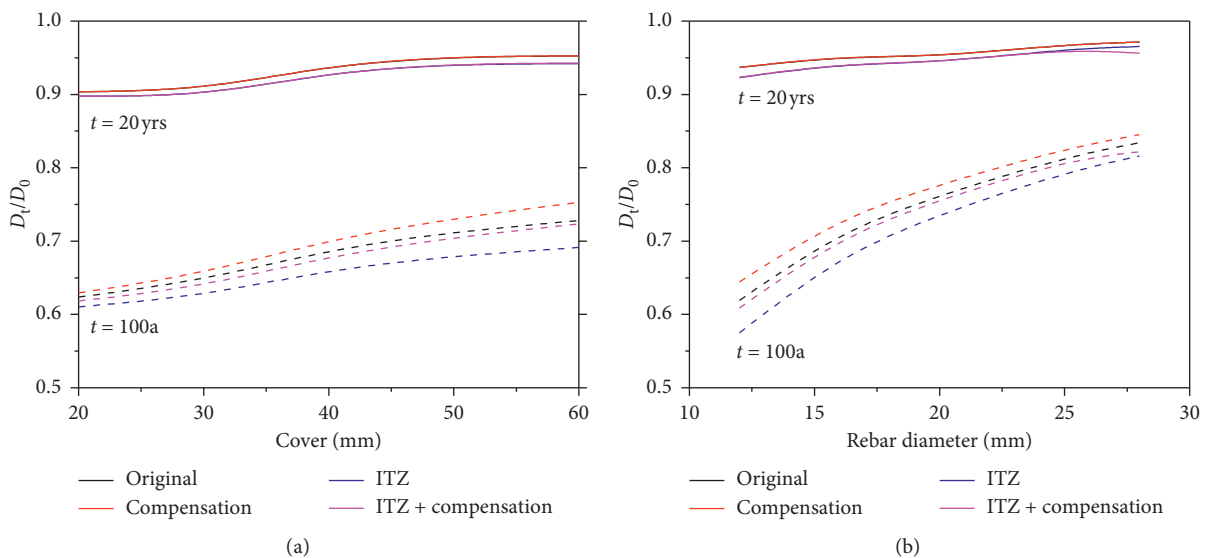


FIGURE 28: Mean chloride content of rebar on center of bottom side (solid: 20 y; dashed: 100 y). (a) Mean remaining diameter vs. cover thickness, 16 mm rebar. (b) Mean remaining diameter vs. diameter, 50 mm cover.

## 6. Conclusion

This paper presented a study on the approach of multiscale modeling for diffusion of chloride ion within concrete including ITZ. A two-phase integrated model including core part and compensation part was introduced, where both phases were connected by an overlapped zone called interfacial transition layer. Nodes and elements of ITZ in FE model were built by expanding outline of aggregates which were randomly generated. Cases considering multiscale and ITZ were studied for obtaining chloride content profile. Moreover, corrosion of rebar on straight edge was discussed

by means of the multiscale approach. The conclusions of this study are summarized as follows:

- (1) The multiscale approach based on the theory of compensation for mesoscopic numerical simulation of chloride diffusion within concrete introduced in this paper was applied by means of numerical simulation. The presented work showed the influence of compensated model on distribution of chloride content, which provided the basis for future large-scale structural durability analysis in optimized size, number of DOFs, and time consumption.



- (2) Regarding diffusivity and width of ITZ, volume fraction, and grade of aggregate, effects of ITZ on distribution of chloride were compared in the presented work. The result showed significant difference on distribution of chloride content between different configuration of ITZ and compensation.
- (3) In the light of corrosion model of steel rebar in terms of surrounding chloride content, presence of ITZ and multiscale compensation was discussed by numerical simulation. The result obtained is related to the configuration of rebar diameter, concrete cover, and exposure period. It was clearly concluded that consideration of both ITZ and compensation changed significantly the distribution of chloride content as well as corrosion process of steel rebar.

### Data Availability

The data used to support the findings of this study are available from the corresponding author upon request.

### Conflicts of Interest

The authors declare that they have no conflicts of interest.

### Acknowledgments

This study was sponsored by the National Key Research and Development Program of China (2016YFC0701202). This study was also supported by the National Natural Science Foundation of China (51508053), the National Natural Science Foundation of China (51808069), and the Fundamental Research Funds for the Central Universities (106112014CDJZR200016), which were greatly appreciated by the authors.

### References

- [1] W. Zhu, R. François, Q. Fang, and D. Zhang, "Influence of long-term chloride diffusion in concrete and the resulting corrosion of reinforcement on the serviceability of RC beams," *Cement and Concrete Composites*, vol. 71, pp. 144–152, 2016.
- [2] Q.-F. Liu, G.-L. Feng, J. Xia, J. Yang, and L.-Y. Li, "Ionic transport features in concrete composites containing various shaped aggregates: a numerical study," *Composite Structures*, vol. 183, pp. 371–380, 2018.
- [3] U. Angst, B. Elsener, C. K. Larsen, and Ø. Vennesland, "Critical chloride content in reinforced concrete—a review," *Cement and Concrete Research*, vol. 39, no. 12, pp. 1122–1138, 2009.
- [4] J.-J. Zheng, H. S. Wong, and N. R. Buenfeld, "Assessing the influence of ITZ on the steady-state chloride diffusivity of concrete using a numerical model," *Cement and Concrete Research*, vol. 39, no. 9, pp. 805–813, 2009.
- [5] L.-X. Mao, Z. Hu, J. Xia et al., "Multi-phase modelling of electrochemical rehabilitation for ASR and chloride affected concrete composites," *Composite Structures*, vol. 207, pp. 176–189, 2019.
- [6] J. Xu and F. Li, "A meso-scale model for analyzing the chloride diffusion of concrete subjected to external stress," *Construction and Building Materials*, vol. 130, pp. 11–21, 2017.
- [7] X. Du, L. Jin, and G. Ma, "A meso-scale numerical method for the simulation of chloride diffusivity in concrete," *Finite Elements in Analysis and Design*, vol. 85, pp. 87–100, 2014c.
- [8] F. Bernard and S. Kamali-Bernard, "Numerical study of ITZ contribution on mechanical behavior and diffusivity of mortars," *Computational Materials Science*, vol. 102, pp. 250–257, 2015.
- [9] J.-J. Zheng and X.-Z. Zhou, "Effective medium method for predicting the chloride diffusivity in concrete with ITZ percolation effect," *Construction and Building Materials*, vol. 47, pp. 1093–1098, 2013.
- [10] K. Wu, L. Xu, G. D. Schutter, H. Shi, and G. Ye, "Influence of the interfacial transition zone and interconnection on chloride migration of portland cement mortar," *Journal of Advanced Concrete Technology*, vol. 13, no. 3, pp. 169–177, 2015.
- [11] Z. Zhang and Q. Zhang, "Self-healing ability of engineered cementitious composites (ECC) under different exposure environments," *Construction and Building Materials*, vol. 156, pp. 142–151, 2017.
- [12] Z. Zhang and Q. Zhang, "Matrix tailoring of engineered cementitious composites (ECC) with non-oil-coated, low tensile strength PVA fiber," *Construction and Building Materials*, vol. 161, pp. 420–431, 2018.
- [13] H. Chen, Z. Zhu, J. Lin, W. Xu, and L. Liu, "Numerical modeling on the influence of particle shape on ITZ's microstructure and macro-properties of cementitious composites: a critical review," *Journal of Sustainable Cement-Based Materials*, vol. 7, no. 4, pp. 248–269, 2018.
- [14] J. F. Unger and S. Eckardt, "Multiscale modeling of concrete," *Archives of Computational Methods in Engineering*, vol. 18, no. 3, pp. 341–393, 2011.
- [15] G.-L. Feng, L.-Y. Li, B. Kim, and Q.-F. Liu, "Multiphase modelling of ionic transport in cementitious materials with surface charges," *Computational Materials Science*, vol. 111, pp. 339–349, 2016.
- [16] K. Maekawa, T. Ishida, and T. Kishi, "Multi-scale modeling of concrete performance," *Journal of Advanced Concrete Technology*, vol. 1, no. 2, pp. 91–126, 2003.
- [17] L. Chen, Z. Qian, and J. Wang, "Multiscale numerical modeling of steel bridge deck pavements considering vehicle-pavement interaction," *International Journal of Geomechanics*, vol. 16, no. 1, article B4015002, 2016.
- [18] Y. Hiratsuka and K. Maekawa, "Multi-scale and multi-chemo-physics analysis applied to fatigue life assessment of strengthened bridge decks," in *Proceedings of XIII International Conference on Computational Plasticity: fundamentals and applications*, pp. 596–607, Barcelona, Spain, September 2015.
- [19] X. Tu et al., "A multiscale numerical simulation approach for chloride diffusion and rebar corrosion with compensation model," *Computers and Concrete*, vol. 21, no. 4, pp. 471–484, 2018.
- [20] X. Wang, M. Zhang, and A. P. Jivkov, "Computational technology for analysis of 3D meso-structure effects on damage and failure of concrete," *International Journal of Solids and Structures*, vol. 80, pp. 310–333, 2016.
- [21] Z. M. Wang, A. K. H. Kwan, and H. C. Chan, "Mesoscopic study of concrete I: generation of random aggregate structure and finite element mesh," *Computers and Structures*, vol. 70, no. 5, pp. 533–544, 1999.
- [22] M. Bailakanavar, Y. Liu, J. Fish, and Y. Zheng, "Automated modeling of random inclusion composites," *Engineering with Computers*, vol. 30, no. 4, pp. 609–625, 2012.

- [23] Z. Y. Ren and J. Y. W., "Generation of spatial convex polyhedron random aggregate model," in *Proceedings of ICOMÉ 2006*, Hefei, China, October 2006.
- [24] A. Caballero, C. M. López, and I. Carol, "3D meso-structural analysis of concrete specimens under uniaxial tension," *Computer Methods in Applied Mechanics and Engineering*, vol. 195, no. 52, pp. 7182–7195, 2006.
- [25] F. Biondini, F. Bontempi, D. M. Frangopol, and P. G. Malerba, "Cellular automata approach to durability analysis of concrete structures in aggressive environments," *Journal of Structural Engineering*, vol. 130, no. 11, pp. 1724–1737, 2004.
- [26] B. Šavija, J. Pacheco, and E. Schlangen, "Lattice modeling of chloride diffusion in sound and cracked concrete," *Cement and Concrete Composites*, vol. 42, pp. 30–40, 2013.
- [27] H. Ma, W. Xu, and Y. Li, "Random aggregate model for mesoscopic structures and mechanical analysis of fully-graded concrete," *Computers and Structures*, vol. 177, pp. 103–113, 2016.
- [28] R. François and G. Arliguie, "Effect of microcracking and cracking on the development of corrosion in reinforced concrete members," *Magazine of Concrete Research*, vol. 51, no. 2, pp. 143–150, 1999.
- [29] T. Vidal, A. Castel, and R. François, "Corrosion process and structural performance of a 17 year old reinforced concrete beam stored in chloride environment," *Cement and Concrete Research*, vol. 37, no. 11, pp. 1551–1561, 2007.
- [30] T. Vidal, A. Castel, and R. François, "Analyzing crack width to predict corrosion in reinforced concrete," *Cement and Concrete Research*, vol. 34, no. 1, pp. 165–174, 2004.
- [31] R. Zhang, A. Castel, and R. François, "Concrete cover cracking with reinforcement corrosion of RC beam during chloride-induced corrosion process," *Cement and Concrete Research*, vol. 40, no. 3, pp. 415–425, 2010.
- [32] R. Zhang, A. Castel, and R. François, "The corrosion pattern of reinforcement and its influence on serviceability of reinforced concrete members in chloride environment," *Cement and Concrete Research*, vol. 39, no. 11, pp. 1077–1086, 2009.
- [33] C. Andrade, C. Alonso, and F. J. Molina, "Cover cracking as a function of bar corrosion: Part I-Experimental test," *Materials and Structures*, vol. 26, no. 8, pp. 453–464, 1993.
- [34] T. Liu and R. W. Weyers, "Modeling the dynamic corrosion process in chloride contaminated concrete structures," *Cement and Concrete Research*, vol. 28, no. 3, pp. 365–379, 1998.
- [35] L. C. Qing, "Corrosion initiation of reinforcing steel in concrete under natural salt spray and service loading—results and analysis," *Materials Journal*, vol. 97, no. 6, 2000.
- [36] S. M. Pritpal and S. E. Mahmoud, "Flexural strength of concrete beams with corroding reinforcement," *ACI Structural Journal*, vol. 96, no. 1, 1999.
- [37] A. A. Torres-Acosta, S. Navarro-Gutierrez, and J. Terán-Guillén, "Residual flexure capacity of corroded reinforced concrete beams," *Engineering Structures*, vol. 29, no. 6, pp. 1145–1152, 2007.
- [38] A. A. Torres-Acosta and M. Martínez-Madrid, "Residual life of corroding reinforced concrete structures in marine environment," *Journal of Materials in Civil Engineering*, vol. 15, no. 4, pp. 344–353, 2003.
- [39] F. Biondini, F. Bontempi, D. M. Frangopol, and P. G. Malerba, "Probabilistic service life assessment and maintenance planning of concrete structures," *Journal of Structural Engineering*, vol. 132, no. 5, pp. 810–825, 2006.
- [40] P. Zhang, D. Li, Y. Qiao, S. Zhang, C. Sun, and T. Zhao, "Effect of air entrainment on the mechanical properties, chloride migration, and microstructure of ordinary concrete and fly ash concrete," *Journal of Materials in Civil Engineering*, vol. 30, no. 10, article 04018265, 2018.
- [41] P. Zhang, F. H. Wittmann, M. Vogel, H. S. Müller, and T. Zhao, "Influence of freeze-thaw cycles on capillary absorption and chloride penetration into concrete," *Cement and Concrete Research*, vol. 100, pp. 60–67, 2017.
- [42] P. Zhang, D. Hou, Q. Liu, Z. Liu, and J. Yu, "Water and chloride ions migration in porous cementitious materials: an experimental and molecular dynamics investigation," *Cement and Concrete Research*, vol. 102, pp. 161–174, 2017.
- [43] X. Li, F. Wu, and Z. Huang, "Analytical solution to chloride diffusion equation on concrete," *Concrete(Chinese)*, vol. 30, no. 10, pp. 30–33, 2009.
- [44] W. Dridi, "Analysis of effective diffusivity of cement based materials by multi-scale modelling," *Materials and Structures*, vol. 46, no. 1-2, pp. 313–326, 2012.
- [45] G. Sun, Y. Zhang, W. Sun, Z. Liu, and C. Wang, "Multi-scale prediction of the effective chloride diffusion coefficient of concrete," *Construction and Building Materials*, vol. 25, no. 10, pp. 3820–3831, 2011.
- [46] Z. Zhu, H. Chen, L. Liu, and X. Li, "Multi-scale modelling for diffusivity based on practical estimation of interfacial properties in cementitious materials," *Powder Technology*, vol. 307, pp. 109–118, 2017.
- [47] K. Maekawa, T. Ishida, and T. Kishi, *Multi Scale Modeling of Structural Concrete*, Taylor & Francis, Vol. 670, Taylor & Francis, Abingdon, UK, 2009.
- [48] Q. Yuan, C. Shi, G. De Schutter, K. Audenaert, and D. Deng, "Chloride binding of cement-based materials subjected to external chloride environment: a review," *Construction and Building Materials*, vol. 23, no. 1, pp. 1–13, 2009.
- [49] P. S. Mangat and B. T. Molloy, "Prediction of long term chloride concentration in concrete," *Materials and Structures*, vol. 27, no. 6, pp. 338–346, 1994.
- [50] B. Šavija, M. Luković, J. Pacheco, and E. Schlangen, "Cracking of the concrete cover due to reinforcement corrosion: a two-dimensional lattice model study," *Construction and Building Materials*, vol. 44, pp. 626–638, 2013.
- [51] Y. Zhao et al., "Concrete surface chloride ion concentration varying with seasons in marine environment (Chinese)," *Journal of Zhejiang University (Engineering Science)*, vol. 43, no. 11, pp. 2120–2124, 2009.
- [52] Z. Pan, A. Chen, and X. Ruan, "Spatial variability of chloride and its influence on thickness of concrete cover: a two-dimensional mesoscopic numerical research," *Engineering Structures*, vol. 95, pp. 154–169, 2015.